Εθνικό Μετσόβιο Πολυτεχνείο
Σχολή Πολιτικών Μηχανικών
Τομέας Γεωτεχνικής

National Technical University of Athens
School of Civil Engineering
Geotechnical Division

Διπλωματική Εργασία

Θωμάς Ανδρουτσέλης

Επιβλέποντες

Καθηγητής Γ. Γκαζέτας
Καθηγητής Ι. Αναστασόπουλος

Μάιος 2014

Σεισμική απόκριση γεφυρών: ο ρόλος των σωμάτων ανάσχεσης και μη γραμμικη αλληλεπιδραση εδάφους – κατασκευής

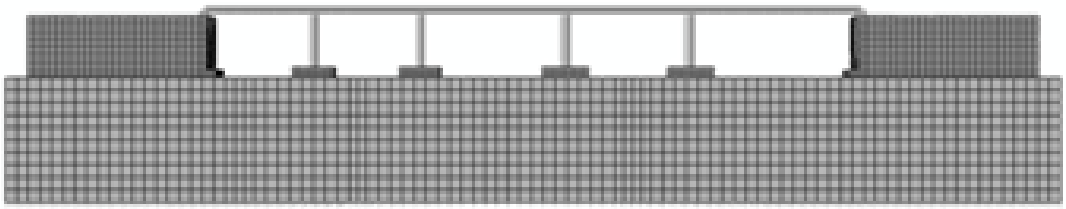

Seismic response of motorway bridges: the role of abutment stoppers and non linear soil – structure interaction

Diploma Thesis

Thomas Androutselis

Supervisors

Professor G. Gazetas
Professor. I. Anastasopoulos

May 2014

Ευχαριστίες

Ολοκληρώνοντας τη διπλωματική μου εργασία, νιώθουμε βαθιά την ανάγκη να ευχαριστήσω τους ανθρώπους που συνέβαλαν στην επίτευξη αυτού του στόχου.

Αρχικά, θα ήθελα να ευχαριστήσω θερμά τον καθηγητή μας Γ. Γκαζέτα που ες τίμησε με την εμπιστοσύνη του και μου έδωσε την ευκαιρία να εργαστώ υπό την επίβλεψη και την καθοδήγησή του. Η συναναστροφή μαζί του κατά τα χρόνια των σπουδών μου υπήρξε πολύτιμη και ιδιαίτερα διδακτική.

Ιδιαίτερες ευχαριστίες οφείλω καθηγητή Ι. Αναστασόπουλο, για την εξαιρετική συνεργασία που ανέπτυξα μαζί του όλους αυτούς τους μήνες. Η πολύτιμη καθοδήγηση, οι υποδείξεις και η αμέριστη συμπαράστασή του ήταν καθοριστικές για την επιτυχή ολοκλήρωση αυτής της εργασίας.

Θα ήθελα επίσης να ευχαριστήσω τον καθηγητή Π. Αναστασόπουλο, για την σημαντική βοήθειά του. Η συμβολή του υπήρξε καθοριστική στη κατεύθυνση και τους στόχους της παρούσας εργασίας.

Ολοκληρώνοντας, θα ήθελα να ευχαριστήσουμε θερμά τον υποψήφιο διδάκτορα Α. Τσάτση για τις συμβουλές και τη διαρκή βοήθειά του. Βεβαίως, ευχαριστώ πολύ και όλα τα υπόλοιπα μέλη του Εργαστηρίου Εδαφομηχανικής που με στήριξαν ενεργά κατά τη διάρκεια της εργασίας αυτής.

Τέλος, νιώθω την ανάγκη να ευχαριστήσω την οικογένειά μου και τους φίλους μου που βρίσκονται πάντα δίπλα μας στηρίζοντας τις προσπάθειές μας.

Table of Contents

INTRODUCTION

SCOPE OF THE THESIS

1. Earthquake Rapid Response System for Metropolitan Motorways

The consequences of a strong seismic event in a metropolitan motorway network can be distinguished in: (a) structural damage of motorway infrastructures, and (b) deterioration of serviceability. The latter can either be due to a decrease of motorway capacity due to damage of critical infrastructures, or to the increase of demand due to damage within the neighbouring urban environment.

Although the direct consequences of a strong earthquake cannot easily be avoided, the *indirect consequences* can be effectively mitigated through timely development and implementation of a rapid response system. Such a system aims to: (a) ensure the safety of motorway users and avoid panic, (b) minimize closure of the motorway, and (c) optimize system serviceability after the earthquake.

Evidently, emergency inspection of motorway infrastructures will be essential after a strong seismic event. However, prior knowledge of the seismic vulnerability of critical structures is necessary: (i) to rationally decide whether there is a need for emergency inspection, and (ii) to rationally allocate inspection teams, allowing for minimum disruption of traffic operations. Such prior knowledge of the seismic vulnerability of the motorway will enable prediction of potential damage distribution, facilitating the detection of sensitive areas within the network. This way, realistic seismic damage scenarios can be devised before-hand, to estimate the potential capacity deterioration of the motorway network, as well as the increased demand due to damage in neighbouring urban areas. Such scenarios can then be utilized to test before-hand (through traffic analysis simulation) the effectiveness of possible emergency response actions.

The development of such a system requires knowledge of: (a) of the accurate evaluation of the seismic hazard (b) the seismic vulnerability of critical motorway infrastructures, such as bridges, cut-and-cover and bored tunnels, retaining walls, cut slopes, and embankments; and (c) knowledge of the typology and all necessary information regarding the geometric and material `properties of the network system and its subsystems.

1.1 Seismic Hazard Assessment

Various methods have been proposed to characterize the seismic hazard broadly categorized in *deterministic* and *probabilistic*. A significant amount of empirical correlations (broadly known as attenuation relationships or recently Ground Motion Prediction Equations–*GMPE*) can be found in the literature for estimation of ground motion characteristics, commonly expressed through spectral acceleration or displacement with regard to earthquake magnitude, distance from the source, soil and geologic site conditions (Figures I.1, I.2).

To model the consequences of failure to a motorway it is important to define seismic scenarios in a coherent and realistic manner. Traditional seismic hazard analysis, whilst effective in translating the hazard into a probabilistic formulation, is limited in the extent to which it can incorporate spatial coherency of the form needed for estimation of loss to spatially distributed portfolios. This approach becomes computationally and theoretically more complex when considering more than a few correlated sites or ground motions. So an alternative approach is the use of seismic scenarios, from which it is possible to create fields of expected ground motions, which are then input into seismic risk models.The performance of a motorway network may be conditional upon failure of different elements, each responding differently to the ground motion. Certain components may respond adversely to strong accelerations, whilst other elements or larger structures may be sensitive to low period motions and ground displacements. Other may be mainly affected by permanent displacements (fault crossing, landslides). Hence, the characterization of ground motion and the associated permanent ground displacements constitute a crucial element for the assessment of the risk of isolated structures. Many intensity measures (IM) have been developed and are readily available in the literature.

1.2 Seismic Vulnerability of critical Motorway Infrastructures

A widely used way to express vulnerability of a motorway infrastructure , especially referring to bridges, are fragility curves, which describe the probability of an element at risk, to be in or to exceed different damage states for a given seismic intensity. They can be classified as : (a) generic–based on expert judgment [e.g., ATC-13, ATC-25], (b) empirical–based mainly on surveys after earthquakes [Basoz et al., 1999; Shinozuka et al., 2000a], and (c) analytical–based on numerical simulation [Shinozuka et al., 2000b; Elnashai et al., 2004; Nielson & DesRoches, 2007]. Although such a plethora of fragility curves for bridges is readily available in the literature, they typically refer to a single bridge component as representative of the overall fragility. Another more recent approach to express vulnerability is Incremental Dynamic Analysis (IDA) curves, which express the correlation between an IM and a Damage Measure (DM) for a specific accelerogram while the intensity increases.

Bridges represent a particular challenge in the analysis of seismic risk of motorways. Failure of a bridge may occur due to either strong seismic shaking or ground deformation, or a combination of both. The response of a bridge due to strong shaking may vary according to many different factors including span and skewness, in addition to the common situation whereby the fundamental period of a column differs in the longitudinal and transverse direction.

For a portfolio of bridges within a region, the vast disparity in bridge geometry, construction type and method (including design code level) limit the extent to which the structural models can be adequately described. Consequently the gain in efficiency for using complex spectral IMs may be offset by the uncertainty in the structural model. Modeling infrastructure and complex systems presents a challenge in this approach (Figure I.3, I4).

One of the main purposes of the analysis is to highlight the most crucial parameters affecting the vulnerability, including (but not limited to): the typology of the structural system, P-Δ effects, the characteristics of the ground motion, and the magnitude of ground-induced deformation.

2. Proposal of the thesis:

Seismic performance of typical motorway bridges: the role of abutment stopper and nonlinear SSI

The number and the variety of bridges of a metropolitan motorway make the computational effort to estimate precisely the seismic vulnerability of each one of them, unprofitable. In addition to this, the necessity to take into account the contribution of each component of a bridge as well as the interaction between them to the seismic response of the whole bridge, leads to very complicated models. Hence, the need for classification of bridges and subsequently the creation of a simplified model which has the similar seismic performance with the original bridge led to a simplified method that estimate the seismic vulnerability of bridges considering soil-structure interaction (Agalianos-Sakelariadis,2013).

In order to simulate more accurately a whole bridge in a simplified model, it is necessary to take into account the effect of each one of the components of the bridge and examine its behavior. The simplified model (Agalianos-Sakelariadis,2013) includes the contribution of the bearings and the rotational stiffness of the deck.

One of the key objectives of the present thesis is to expand this simplified method by simulating the contribution of the abutment stopper and nonlinear soil-structure interaction.

2.1 Main Structure of the Thesis

The main scope of this thesis is to examine the seismic performance of typical motorway bridges when a seismic event occurs including the impact of stoppers and non-linear SSI and add their impact on the simplified model (Agalianos-Sakelariadis,2013).

Firstly, the role of the abutment stopper as a bridge component is examined and how it effects the seismic performance of a motorway bridge by limiting the bridge seismic movements. It is necessary to realize its behavior during a seismic event, so that it is easier to simulate it. In addition, the role of non-linear SSI is studied and see how it improves the seismic performance of the bridge.

For this reason, a simple symmetric bridge with fixed base of the Greek metropolitan motorway ''Attiki Odos'' was modeled and non-linear time history analyses were performed, in order to obtain the damage indices.

The next step was to develop a complete 3D model of a bridge which was examined in ABAQUS finite element code. Comparing this model with the fixed base bridge the impact of SSI is quantified.

The following challenge is to examine the behavior of the retaining walls which are connected with the simulation of the abutment stoppers. In order to fully understand the procedure of the simulation, all the attempts made till the optimum simulation of the stoppers are shown.

Moreover, another more complicated bridge of the Greek metropolitan motorway ''Attiki Odos'' was modeled to validate the precision of the simulation. Based on the previous pattern, a simple fixed base model and a 3D model were developed.

The last parameter to be taken into account was non-linear Soil-Structure interaction. For this purpose, both bridges were tested with under-dimensioned foundations (rocking isolation) to investigate the performance of the rocking-isolated system and compare it with the conventional bridge.

CHAPTER 1

LITERATURE REVIEW

FRAGILITY CURVES – IDA CURVES

1.1 Fragility Curves

A widely used way to express vulnerability of a motorway infrastructure , especially referring to bridges, are fragility curves, which describe the probability of an element at risk, to be in or to exceed different damage states for a given seismic intensity. They can be classified as: (a) generic–based on expert judgment [e.g., ATC-13, ATC-25], (b) empirical–based mainly on surveys after earthquakes [Basoz & Kiremidjian, 1997; Yamazaki et al., 1999; Shinozuka et al., 2000b; Kiureghian, 2002], and (c) analytical–based on numerical simulation [Shinozuka et al., 2000b; Karim & Yamazaki, 2002; Elnashai et al., 2004; Nielson & DesRoches, 2007;]. Although such a plethora of fragility curves for bridges is readily available in the literature, they typically refer to a single bridge component as representative of the overall fragility.

1.1.1 Fragility functions

One of the key links in the risk assessment methodology is to estimate the damage to the lifeline components. This is done by estimating the performance of the various highway bridges in the network as a function of a ground motion intensity parameter. This bridge performance is commonly represented in either a damage probability matrix or a fragility function.

A fragility function is a conditional probability that gives the likelihood that a structure will meet or exceed a specified level of damage for a given ground motion parameter. This conditional probability is given in the following equation:

$$Fragility = P[S > LS \mid IM = y] \quad (1)$$

where S is the response measure of the bridge or bridge component, LS is the limit state or damage level of the bridge or bridge component, IM is the ground motion intensity measure and y is the realization of the chosen ground motion intensity measure. One can see from this formulation that given a scenario earthquake, a prediction of the damage level may be made for each bridge for which a fragility function is defined.

This probabilistic way of estimating structural damage was used in the evaluation of nuclear facility vulnerabilities in the late 1970's and early 1980's and since then has expanded into other areas of structural engineering. The 1985 ATC-13 report presented this probability of damage in the discrete form of damage probability matrices which were later followed by the introduction of continuous cumulative distribution functions or fragility curves in the 1991 ATC-25 report as well as the first release of the FEMA funded HAZUS software in 1997. There are many different methodologies that have been employed in the determination of these structural fragilities, a synopsis of which will be given in the following sections.

1.1.2 Generic fragility curves

Generic fragility curves are based on expert judgment. A typical example of developing generic fragility curves is the ATC-13 report (ATC, 1985) developed by the Applied Technology Council (ATC) of California, USA. In October 1982 the Federal Emergency Management Agency (FEMA) awarded Applied Technology Council (ATC) a contract to develop earthquake damage evaluation data for facilities in California. FEMA was planning to use these data and companion loss estimation and inventory methodology to estimate the economic impacts of a major California earthquake. Because the required earthquake damage, loss and inventory data were not available in the literature, ATC and FEMA agreed that the best way to develop the required data was to draw on the experience and judgment of seasoned earthquake engineers. The ATC put together a panel of 42 experts, four of which were for bridges, whom they could query concerning the various components of a typical Californian infrastructure.

The questionnaires that were created queried the experts on the probability of a bridge being in one of seven damage states for a given Modified-Mercalli Intensity (MMI) value. They also asked the experts to rate themselves on their experience in the field on a scale from zero to ten. After the questionnaires were completed and analyzed, the results were given back to the experts for a second look. They were permitted to consider the overall results and compare them with their initial responses and make any modifications they felt were necessary. These results were then compiled and reported as the probability damage matrices (DPM) for bridges in the ATC-13 report (ATC, 1985) and were subsequently used in the ATC-25 report (ATC, 1991). (Table 1.1, Figures 1.1)

1.1.3 Empirical fragility curves

Empirical fragility curves are based mainly on surveys after earthquakes. Following the 1989 Loma Prieta and 1994 Northridge earthquakes empirical bridge fragility curves became more common as a direct result of more complete ground motion and bridge damage data. Empirical fragility curves are generated from actual earthquake data. This methodology has been presented and demonstrated by several groups of people for the Loma Prieta and Northridge earthquakes such as Basoz and Kiremidjian (1997), Kiureghian (2002), Shinozuka et al. (2000b) and by Yamazaki et al. (1999) for the 1995 Kobe earthquake.

Although there are some slight variations in the methods used by the aforementioned groups they are conceptually the same. The procedure requires that a post-earthquake assessment be performed where a damage state would be assigned to all the bridges that belong to the bridge class being considered. A shake map, that geographically defines the ground motion in terms of some intensity measure, such as peak ground acceleration (PGA) is used to assign each bridge to a damage state and a given ground motion intensity in a damage frequency matrix.

Table 1.2 is an example of a damage frequency matrix that was assembled by Basoz and Kiremidjian (1997) for all multi-span bridge types as they performed in the Northridge earthquake. Thus a percentage of the overall bridge class inventory may be displayed for each damage state at each ground motion intensity level as shown in Table 1.3.

This information can be used in any number of ways. Basoz and Kiremidjian (1997) used a logistic regression analysis to generate the fragility curves shown in Figure 1.2 from the damage matrices shown in Tables 1.2, 1.3. Shinozuka et. al (2000b) recommends using the Maximum Likelihood method in conjunction with hypothesis and goodness of fit tests to estimate the parameters of the two parameter lognormal probability distribution while Kiureghian (2002) used a Bayesian approach and the Likelihood function to accomplish this task.

Although this method is relatively straight forward it has limitations. The first limitation is that it is difficult to get an adequate number bridges belonging to one bridge class that lie in a particular damage state to get statistically significant results (Shinozuka, 2000b). Thus it is often required to group classes together to get enough bridges in a given damage state and hence reduces the usefulness of the fragility curves.

However, these empirical fragility curves can still be used to calibrate/validate analytical fragility curves which will be discussed hereafter (Basoz and Kiremidjian, 1999).

Another limitation that Basoz and Kiremidjian (1997) noted in their generation of fragility curves for several classes of bridges in both the Loma Prieta and Northridge earthquakes was that the ground motion intensity (Shake maps) were different depending upon who generated them. They received two different maps with different values for the Northridge earthquake (USGS and WCFS) and three different maps for the Loma Prieta earthquake (observed, Boore and Joyner, Campbell).

Yet another limitation of empirical fragility curves is that when post-earthquake assessments of bridges are made and damage levels assigned, there is often a discrepancy between the damage levels that any two different inspectors would assign (Basoz and Kiremidjian, 1997). Thus another source of uncertainty is entered into the curves.

1.1.4 Analytical fragility curves

Analytical fragility curves are based on numerical simulation. When actual bridge damage and ground motion data are not available, analytical fragility curves must be used to assess the performance of highway bridges. There have been many researchers that have developed analytical fragility curves for bridges. As previously mentioned, a fragility curve is a conditional probability that specifies the likelihood of a structure or structural component reaching or exceeding a damage state for a specified ground motion intensity. Since damage states are related to structural capacity and the ground motion intensity parameter is related to structural demand, the fragility can then be described as the probability that the seismic demand will exceed the structural capacity. This probability of failure is represented in the following equation (Melchers, 1999):

$$p_f = P\left[\frac{S_d}{S_c} \geq 1\right] \tag{2}$$

where *pf* is the probability of exceeding a specific damage state, *Sd* is the structural demand and *Sc* is the structural capacity or damage state.

This probability is generally modeled as a lognormal probability distribution. This model is chosen because it has shown to be a good fit in the past and is convenient for manipulation using conventional probability theory (Wen et al., 2003). In addition, when the structural capacity and demand roughly fit a normal or lognormal distribution, using the central limit theorem, it can be said that the composite performance will be lognormally distributed (Kottegoda and Rosso, 1997). Thus the fragility curve can be represented by a lognormal cumulative distribution function which is given in the following equation (Melchers, 1999):

$$p_f = \Phi\left[\frac{ln\left(S_d/S_c\right)}{\sqrt{\beta_d^2+\beta_c^2}}\right] \tag{3}$$

where *Sc* is the median value of the structural capacity defined for the damage state, β*c* is the dispersion or lognormal standard deviation of the structural capacity, *Sd* is the seismic demand in terms of a chosen ground motion intensity parameter, βd is the logarithmic standard deviation for the demand and Φ[•] is the standard normal distribution function.

Using the above equation it can be seen that the structural demand and capacity must be modeled to generate analytical fragility curves. Figure 1.3 presents the basic flow of analytical fragility curve generation using non-linear time history analysis. Although there are some variations to this methodology that are used, this represents the basic overall procedure. The first step is to obtain a suite of ground motions that is appropriate and representative of the target geographic area and captures the uncertainty inherent in ground motions such as the

magnitude and the epicentral distances. Next, the structural properties (material strengths and geometric values) are probabilistically sampled for a base bridge model. This will be done N times thus generating N nominally identical but statistically different bridge samples. Then the ground motions are paired with the bridge simulations and a non-linear time history analysis is performed. For each simulation, the peak structural responses for key elements (i.e. column's ductility, bearing deformation, abutment displacement, etc.) are collected. Using the peak bridge component responses, a probabilistic seismic demand model is generated by using a regression analysis of the ground motion parameters and the peak structural response.

The capacity or limit state of each component is combined with the seismic demand in the above equation to generate the fragility curves. The next few sections will discuss each of these steps in more depth.

Typical analytical Fragility curves from the work of Karim & Yamazaki (2001) are shown on Figure 1.4 while analytical fragility curves from the work of Choi & Nielson are presented on Figure 1.5.

1.1.4.1 Selection of ground motion time-histories

As part of the probabilistic seismic demand analysis (PSDA), a suite of ground motion time histories must be obtained for use therein. The composition of this suite is a function of the requirements of the PSDA methodology chosen. For instance, if the PSDA is being performed for bridges in Southern California then a suite of time histories may be assembled from strong ground motion records from the area. In work done by Mackie and Stojanovic (2003), they assemble four suites of 20 ground motions each having different magnitudes and epicentral distances.

When the PSDA is being used for regions where little or no strong ground motion records are available, such as the Mid-America region of the U.S., it becomes necessary to use outside records or create synthetic time histories by sampling on ground motion parameter random variables. There have been a number of groups that have generated synthetic ground motions for use in this region (Wen and Wu, 2001; Herrmann and Akinci, 1999; Hwang et al., 2000c).

The number of ground motions required for the analysis also varies depending on the methodology used. In work done by Hwang et al. (2000c) and Choi (2002) a suite of ground motions containing 100 records was used. Shome et al. (1998) state that the lognormal assumption for the model allows suites containing 20 ground motions are sufficient to achieve the required confidence levels, while Wen et al. (2003) assert that suites with as few as ten ground motions are adequate to capture the structural response.

Another issue that arises is the question of what ground motion intensity parameter best captures the response and minimizes the dispersion of that response. The traditional intensity parameters that have been used are MMI (ATC, 1985) and PGA (FEMA, 1997), but Mackie and Stojanovic (2003) point out that there are up to 22 different ground motion intensity parameters that could be used. These parameters range from geometric properties (epicentral distance) to peak motion quantities (PGA, PGV, PGD) to spectral quantities (Sa, Sv, Sd) to energy based quantities (Mw). However, they state along with others, that the spectral quantities at the fundamental period of the structure, such as spectral acceleration, velocity and displacements, produce better results than do peak ground motion quantities such as peak ground acceleration, velocity and displacement (Wen et al., 2003; Mackie and Stojanovic, 2003; Hwang et al., 2000b).

It is interesting to note that although most fragility work done now with respect to buildings is done using spectral quantities, the bridge community is still predominantly using PGA as the intensity measure. This reluctance of the highway bridge community to switch to spectral values is in part due to the challenges associated with their use. One of these challenges is the difficulty in comparing the fragility of various bridges types. When the bridge types have different fundamental periods, the fragility comparisons must be done at a specific ground motion. Also to use the fragility curves in a risk assessment program it is imperative that the fundamental period of the structure be known. This is not always possible when the bridge information is pulled out of the NBI database. In addition to the challenges of implementation, some in the transportation arena assert that there is very little difference in the transportation network loss calculations as well as the dispersion of the results when the use of PGA and Sa is compared (Tri-Center Workshop, 2003).

1.1.4.2 Bridge model simulation

A base bridge analytical model needs to be created that is representative of the target structure. It should be noted that this not a trivial task. In fact, Song and Ellingwood (2001) recommended that less time should be spent developing more efficient Monte Carlo sampling techniques and more time should be focused on generating better models, indicating that the modeling procedure plays a very important role in the outcome of the model.

Different structural properties that define the bridge model, such as concrete compressive strength, yield strength of the reinforcing steel, deck mass, deck gap width, column height and span length will need to be defined probabilistically. These structural properties should each be assigned a probability distribution to account for their uncertainty. Then using a sampling technique such as Importance Sampling (Melchers, 1989) or Latin Hypercube sampling (Ayyub and Lai, 1989), these structural parameters can be sampled based on their distributions to create a required number of nominally identical but statistically different bridge samples. Not all structural properties need to be treated probabilistically.

A sensitivity analysis of the various structural properties is generally performed to indicate which ones should be treated probabilistically and which ones may be treated deterministically.

As previously mentioned, the model generation is not a trivial task. Whenever an analytical model is created the assumptions and modeling format are a major concern. The general consensus in the field of structural engineering is that the simpler the model the better off you are. However, caution must also be used so as not to oversimplify.

1.1.4.3 Transverse vs. Longitudinal

When generating the analytical models for bridges, assumptions and simplifications are often made to make the analyses more feasible. A full three dimensional model of a bridge may be generated but the analysis becomes extremely computationally expensive when it is used in a Monte Carlo simulation. Therefore much of the work done to date has simplified the models by modeling the bridges in two dimensions. This requires the bridges to be modeled in both the transverse and longitudinal directions. In an attempt to cut down further on the amount of work required to adequately quantify a bridge response, it is advantageous to explore whether or not one loading direction controls the response of the bridge.

There have been a number of studies that indicate that the longitudinal direction controls the response of the bridge (Choi, 2002; Rashidi and Saadeghvaziri, 1997) while others maintain that the loading in the transverse direction controls the damage of the bridge (Cheng et al, 1998; Saadeghvaziri and Rashidi, 1998).

There are yet others that believe that a bridge must be modeled in three dimensions and have the longitudinal and transverse responses combined in some fashion to adequately represent the system (Jernigan and Hwang, 2002; ATC, 1991; Yashinski, 1999; Hwang et al, 2000b). It is clear from the many different views on this issue that there is no definite methodology that should be used for the analytical modeling of bridges.

1.1.4.4 Vulnerable bridge components

There are a number of different vulnerable components in a bridge system which include the columns/piers, fixed and expansion bearings, abutments and foundations. Almost all of the previous work for fragility analysis of bridges has assumed that the columns/piers are the only vulnerable component (ie. the fragility of the column is equivalent to the fragility of the entire bridge system) (Dutta and Mander, 1998; Hwang et al, 2000b; Hwang et al, 2000c; Mander and Basoz, 1999; Shinozuka et al, 2000a; Shinozuka et al, 2000b). However, previous work has shown that the steel fixed bearing is the most fragile component for the multi-span simply supported steel girder bridge at all of the damage states.

This trend varies for different bridge types. For example, the columns for the multi-span continuous pre-stressed concrete girder bridge typical to Mid-America are the most fragile bridge component in the moderate, extensive and complete damage states (Choi, 2002).

This indicates that it is important to include all major vulnerable components when doing a fragility analysis of a bridge. If the assumption was made that the column damage states were representative of the damage states of the entire bridge, it is likely that this would result in an underestimation of the overall bridge system fragility.

1.1.4.5 Seismic demand

There are several different methodologies that have been proposed for the analysis of the seismic demand of a structure ranging from simplistic in nature to labor intensive. Some of these methods are using probabilistic response spectra in conjunction with the NBI data (Dutta and Mander, 1998; FEMA, 1999), using an elastic spectral analysis couched in a capacity/demand ratio formulation (Jernigan and Hwang, 2002; Hwang et al., 2000b), using a reduced response spectrum (Shinozuka et al., 2000b), using non-linear time history analysis in incremental dynamic analysis (IDA) (Mackie and

Stojanovic, 2003) and using non-linear time history analysis to perform a probabilistic seismic demand analysis (Hwang and Huo, 1998; Hwang et al., 2000c; Choi, 2002; Mackie and Stojanovic, 2001; Song and Ellingwood, 2001; Wen et. al, 2003). It appears that the majority of the seismic demand modeling work to date has been using non-linear time history analyses using Monte Carlo simulation techniques. It is also the most reliable method available (Shinozuka et al., 2000a).

As shown in Figure 1.3, a probabilistic seismic demand model (PSDM) must be generated if the non-linear time history approach is to be used. This is done through a probabilistic seismic demand analysis (PSDA) which relies heavily upon the first three steps in Figure 1.3. As previously mentioned these steps would be to combine a suite of ground motions with a suite of bridge samples to create ground motion-bridge pairs. These pairs are then analyzed using a finite element analysis package. For each analysis, the maximum response quantities of interest, such as column curvature ductility (μθ) and the bearing and abutment deformations (δb, δa), are recorded and plotted versus the ground motion intensity parameter value, as seen in Figure 1.6. A linear regression of the form shown in Equation 4 is then performed to determine the seismic demand, Sd, as a function of the ground motion intensity measure (IM) for each of the bridge components. This is shown in Equation 5, where a and b are the unknown regression coefficients.

$$\ln(S_d) = b\ln(IM) + \alpha \tag{4}$$

$$S_d = IM^b e^a \tag{5}$$

This seismic demand, Sd, is the first half of the input to the fragility function, Equation 3. The structural capacity or limit states must also be acquired as will be addressed in the next section.

1.1.4.6 Structural capacity and damage states

As previously mentioned, the other part of fragility modeling requires something to be known about the capacity or limit states of the structure. To facilitate further discussion about the structural capacity a brief discussion on damage or limit states is required. A limit state is defined as the capacity that a structure or structural component has before reaching a specified level of damage or deformation. These limit states, which have traditionally been given in qualitative terms, are defined and discretized differently by various researchers.

For example, the ATC-13 and ATC-25 reports list seven damage states (ATC, 1985; ATC, 1991). HAZUS reports five damage states (FEMA, 1997) and Hwang and Huo (1998) used two. It should be noted that it appears as if the majority of users appear to use the qualitative damage states as given by HAZUS.

The qualitative limit state descriptions work well for fragility curves that are based on expert judgment and empirical methods, but quantitative descriptions are needed for use in analytical models. The question of what response quantities (deformations, ductilities, material response etc.) will result in the qualitative description for the various damage states needs to be answered. There have been a number of tests and analytical procedures implemented to address this issue. Dutta and Mander (1998) in addition to Akkari and Duan (2000) used static pushover with plastic analysis to get deterministic capacity values with assumed dispersion values with many others following similar paths (Choi, 2002; Shinozuka et al., 2000b; Hwang and Huo, 1998; Hwang and Jaw, 1990; Hwang et al., 2000c). Shinozuka et al. (2000a) used a capacity spectrum analysis while others recommended the use of an incremental dynamic analysis (IDA) to calculate the capacity against collapse (Wen et al., 2003). An example of a quantitative equivalent to the qualitative descriptions of the bridge component limit states is presented in Table 1.4. These are the limit states that Choi (2002) used in his work for developing fragility curves for bridges in Mid-America. This table shows the median values of the limit states that were used in conjunction with the dispersions that were recommended by HAZUS 97.

There have been numerous studies done on the behavior of reinforced concrete bridge piers and columns to assist in the quantification of pier/column limit states (Kowalsky, 2000; Park et al., 1982; Ghosn and Chen, 1991). However, there have not been many studies on the response of other vulnerable bridge components, such as bearings (Mander et al., 1996) and abutments (Goel and Chopra, 1997). Therefore expert or professional judgment is still required in defining the capacity limit states of bridge components.

1.1.4.7 Component vs. System fragility

The process that is explained in Figure 1.3 is the process to generate fragility curves for the individual bridge components. It is necessary, however, to obtain an overall bridge or system fragility for use in the risk assessment process. This can be performed through a crude Monte Carlo simulation but is considerably more computationally expensive. An alternative would be to combine the component fragility curves to get the system (bridge) fragility curve. This, however, requires information about the stochastic dependence between the damage states of the various bridge components. Using first-order reliability theory, an upper and lower bound on the system fragility can be easily determined. The lower bound is the maximum component fragility while the upper bound is a combination of all of the component fragilities. These bounds are given in Equation 5 where P(Fi) is the probability of failure for each component and P(Fsys) is the probability of failure for the entire system.

These first-order bounds are valid for a series type system where a failure of one the components constitutes a failure of the system (Melchers, 1999). When a bridge is modeled in the longitudinal direction, it in fact behaves like a series system. The lower bound represents the probability of failure for a system whose components are all fully stochastically dependent and provides an un-conservative estimate for the fragilities of the subject bridges. The upper bound assumes that the components are all statistically independent and provides a conservative estimate on the overall bridge fragility. The upper bound estimate to the system fragility gets better as the difference between the upper and lower bound decreases. When the bridge is modeled in the transverse direction, it is no longer solely a series system but rather a combination of parallel and serial components. Therefore if transverse analysis is required, the implementation of more complex second-order reliability techniques will be required.

1.2 Incremental Dynamic Analysis (IDA) Curves

In the wake of the damage brought by the 1994 Northridge earthquake, the SAC/FEMA project was launched to resolve the issue of poor performance of steel moment-resisting frames due to the fracturing beam-column connections. Within the creative environment of research cooperation, the idea of subjecting a structure to a wider range of scaling emerged. Initially, the method was called Dynamic Pushover and it was conceived as a way to estimate a proxy for the global collapse of the structure. It was later recognized that such a method would also

enable checking for multiple limit-states, e.g. for life-safety, as is the standard for most seismic design methods, but also for lower and higher levels of intensity that represent different threat levels, such as immediate-occupancy and collapse-prevention. Thus, the idea for Incremental Dynamic Analysis was born by researchers Vamvatsikos & Cornell (2002) at the John A. Blume Earthquake Research Center of Stanford University.

Incremental Dynamic Analysis (IDA) is a computational analysis method for performing a comprehensive assessment of the behavior of structures under seismic loads. It has been developed to build upon the results of probabilistic seismic hazard analysis in order to estimate the seismic risk faced by a given structure. It can be considered to be the dynamic equivalent of the static pushover analysis.

IDA involves performing multiple nonlinear dynamic time history analyses of a structural model under a suite of ground motion records, each scaled to several levels of seismic intensity. The scaling levels are appropriately selected to force the structure through the entire range of behavior, from elastic to inelastic and finally to global dynamic instability, where the structure essentially experiences collapse. Appropriate post processing can present the results in terms of IDA curves, one for each ground motion record, of the seismic intensity, typically represented by a scalar Intensity Measure (IM), versus the structural response, as measured by an Engineering Demand Parameter (EDP).

Possible choices for the IM are scalar (or rarely vector) quantities that relate to the severity of the recorded ground motion and scale linearly or nonlinearly with its amplitude. The IM is properly chosen well so that appropriate hazard maps (hazard curves) can be produced for them by probabilistic seismic hazard analysis. Possible choices are the peak ground acceleration, peak ground velocity or Arias intensity, but the most widely used is the 5%-damped spectral acceleration at the first-mode period of the structure.

The EDP can be any structural response quantity that relates to structural, non-structural or contents' damage. Typical choices are the maximum (over all stories and time) interstorey drift, the individual peak storey drifts and the peak floor accelerations.

IDA grew out of the typical practice of scaling accelerograms by multiplying with a constant factor to represent more or less severe ground motions than the ones that were recorded at a site. Since the natural recordings available are never enough to cover all possible needs, scaling is a simple, yet potentially problematic method (if misused) to "fill-in" gaps in the current catalog of events. Still, in most cases, researchers would scale only a small set of three to seven records and typically only once, just to get an estimate of response in the area of interest.

Typical IDA curves from the work of Vamvatsikos & Cornell (2002) are shown in Figure 1.7.

Chapter 1

Figures

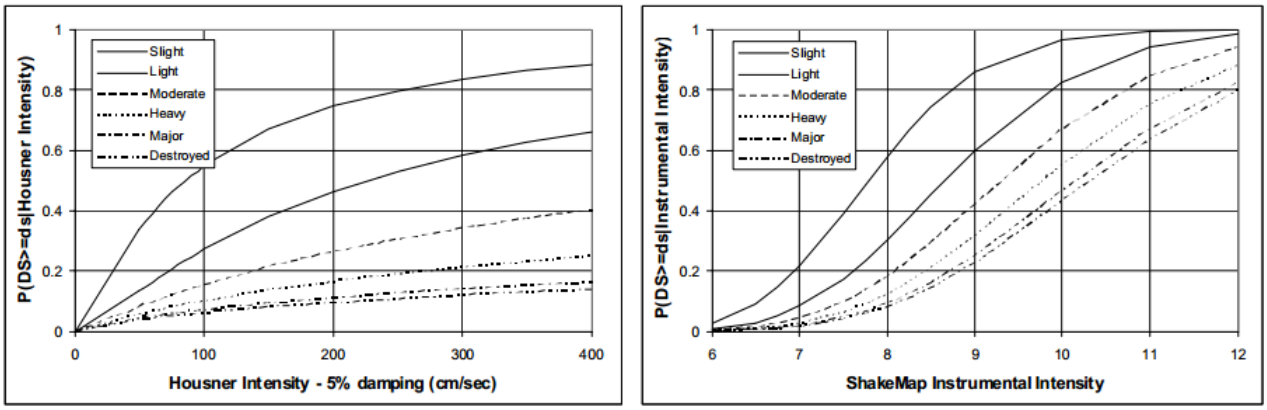

Figure 1.1 Fragility curves for C1 buildings, ATC-13 damage states and parameters *IH* and *IMM*

	USGS Peak Ground Acceleration (g)						
Observed Damage	0.15 –0.2	0.2 - 0.3	0.3 - 0.4	0.4 - 0.5	0.5 - 0.6	0.6 - 0.7	0.7 - 0.8
None	194	262	150	31	10	15	17
Minor	2	8	16	2	6	4	2
Moderate	1	8	8	9	6	5	1
Major	0	6	0	5	5	3	1
Collapse	0	0	0	0	0	0	0
Total	197	284	174	47	27	27	21
	USGS Peak Ground Acceleration (g)						
Observed Damage	0.8 - 0.9	0.9 - 1.0	1.0 - 1.1	1.1 - 1.2	1.2 - 1.3	1.3 - 1.4	Total
None	18	7	9	1	0	1	717
Minor	0	5	1	1	0	0	47
Moderate	4	7	3	0	0	0	52
Major	1	9	0	0	0	0	30
Collapse	2	1	1	0	0	0	4
Total	25	29	14	2	0	1	848

Table 1.2 Damage Frequency Matrix for Multi-Span Bridges (Basoz and Kiremidjian, 1997)

	USGS Peak Ground Acceleration (g)						
Observed Damage	0.15 –0.2	0.2 - 0.3	0.3 - 0.4	0.4 - 0.5	0.5 - 0.6	0.6 - 0.7	0.7 - 0.8
None	98.48	92.25	86.21	65.96	37.04	55.56	80.95
Minor	1.02	2.82	9.20	4.26	22.22	14.81	9.52
Moderate	0.51	2.82	4.60	19.15	22.22	18.52	4.76
Major	0	2.11	0	10.64	18.52	11.11	4.76
Collapse	0	0	0	0	0	0	0
	USGS Peak Ground Acceleration (g)						
Observed Damage	0.8 - 0.9	0.9 - 1.0	1.0 - 1.1	1.1 - 1.2	1.2 - 1.3	1.3 - 1.4	
None	72.00	24.14	64.29	50	0	100	
Minor	0	17.24	7.14	50	0	0	
Moderate	16.00	24.14	21.43	0	0	0	
Major	4.00	31.03	0	0	0	0	
Collapse	8.00	3.45	7.14	0	0	0	

Table 1.3 Damage Probability Matrix for Multi-Span Bridges (%) (Basoz and Kiremidjian, 1997)

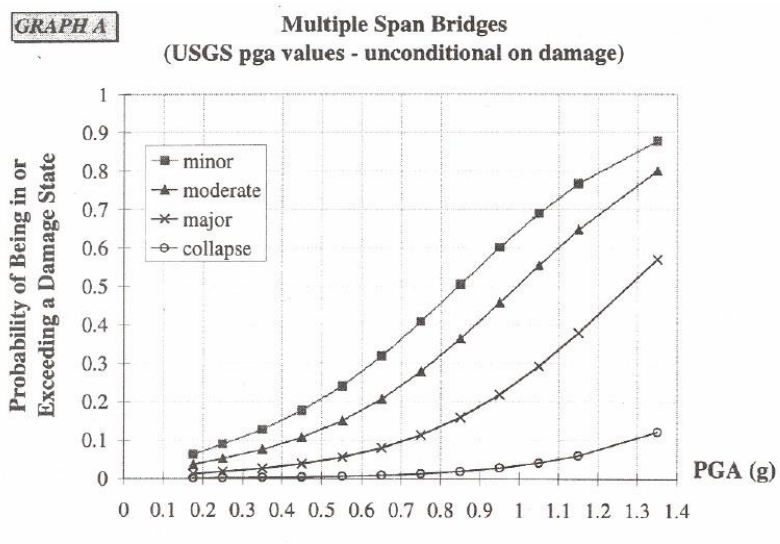

Figure 1.2 Fragility curves using logistic regression analyses (Basoz and Kiremidjian, 1997)

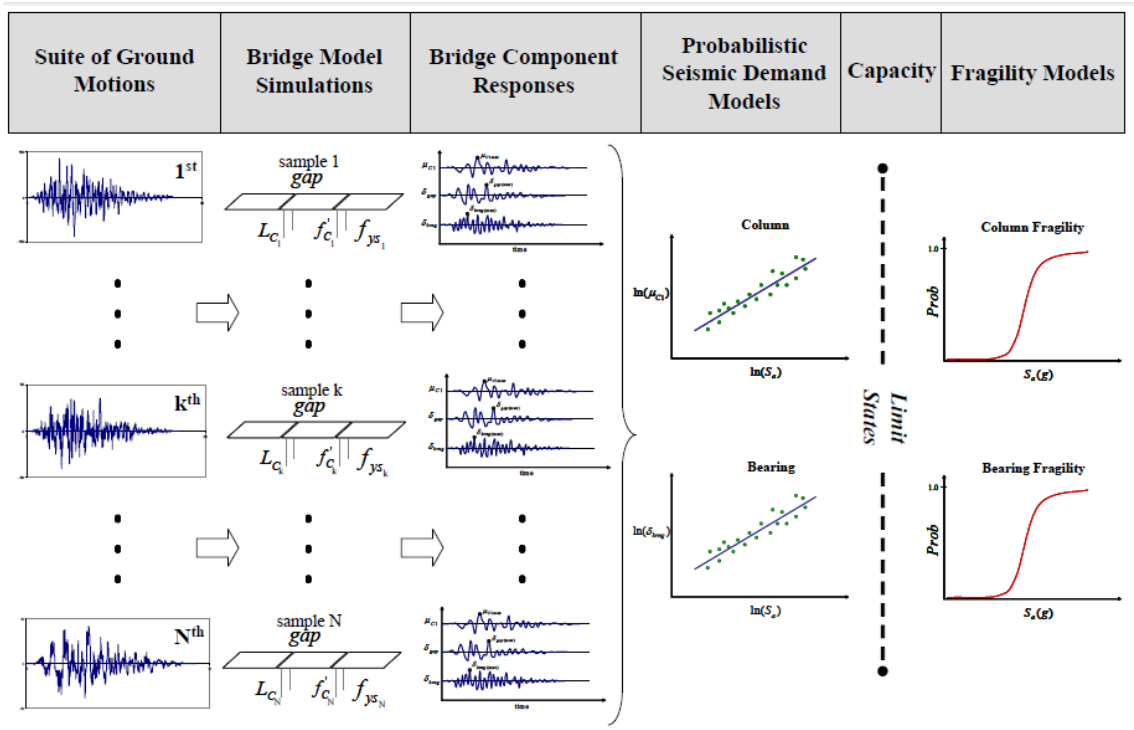

Figure 1.3 Analytical Fragility curve Generation using Non-linear Time History Analysis

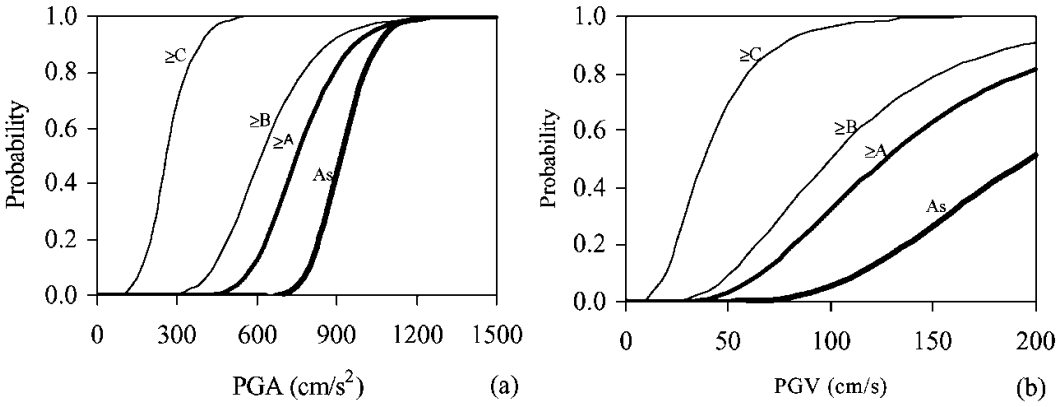

Figure 1.4 Typical analytical Fragility curves from the work of Karim & Yamazaki (2001) with respect to **(a)** PGA and **(b)** PGV obtained from the records of Kobe earthquake

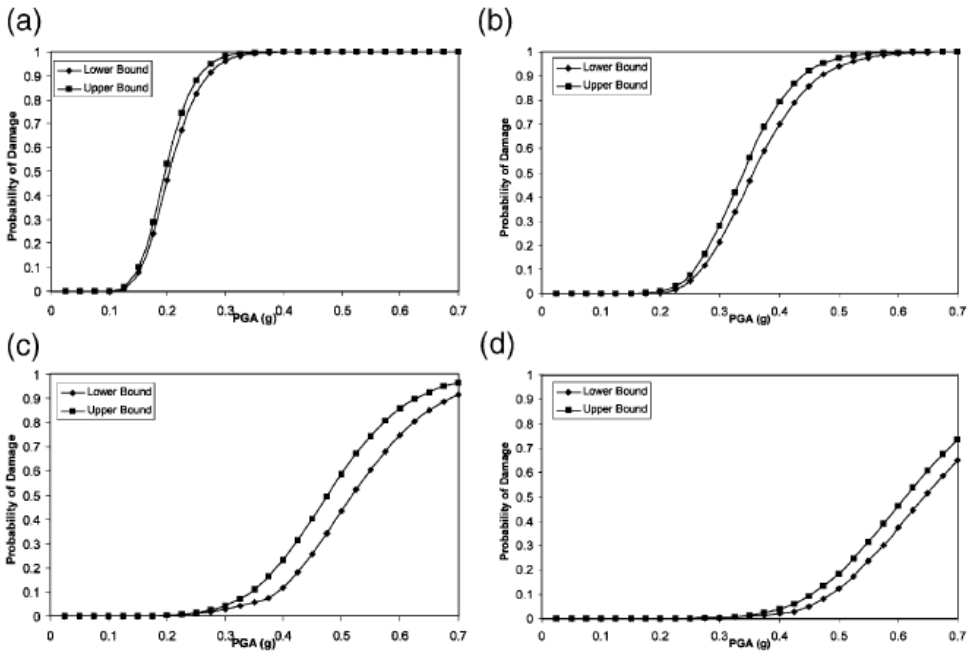

Figure 1.5 Typical analytical Fragility curves from the work of Choi & Nielson (2004) for **(a)** slight damage, **(b)**moderate damage, **(c)** extensive damage and **(d)** complete damage

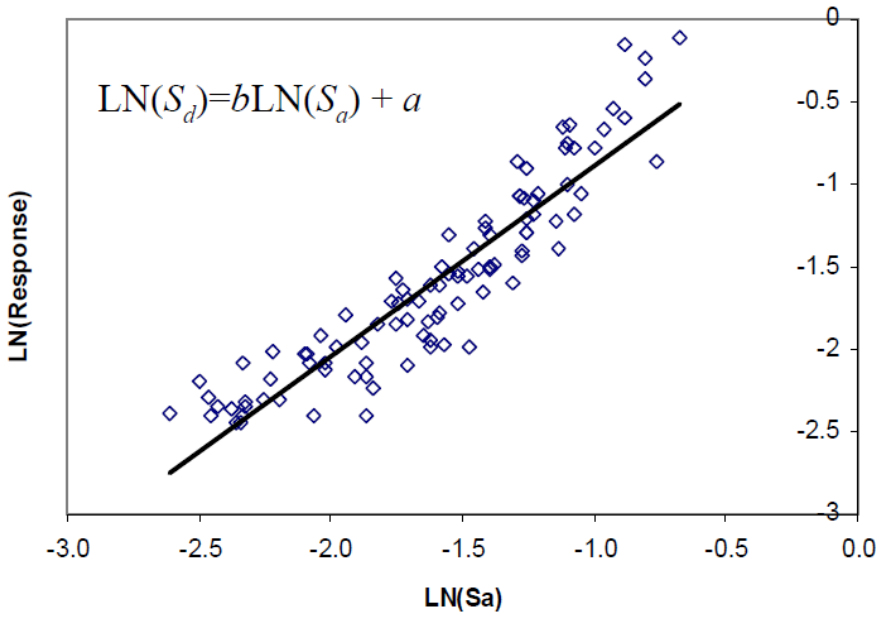

Figure 1.6 Probabilistic seismic demand model (PSDM) using Sa at the fundament period of the bridge

Damage State		Slight Damage	Moderate Damage	Extensive Damage	Complete Damage
Columns	(μ)	1.0<μ<2.0	2.0<μ<4.0	4.0<μ<7.0	7.0<μ
Steel Bearings	(δ, mm)	1<δ<6	6<δ<20	20<δ<40	40<δ
Expansion Bearings	(δ, mm)	δ<50	50<δ<100	100<δ<150	150<δ<255
Fixed Dowels	(δ, mm)	8<δ<100	100<δ<150	150<δ<255	255<δ
Expansion Dowels	(δ, mm)	δ<30	30<δ<100	100<δ<150	150<δ<255

Table 1.4 Definition of Limit States for Bridge Components (Choi, 2002)

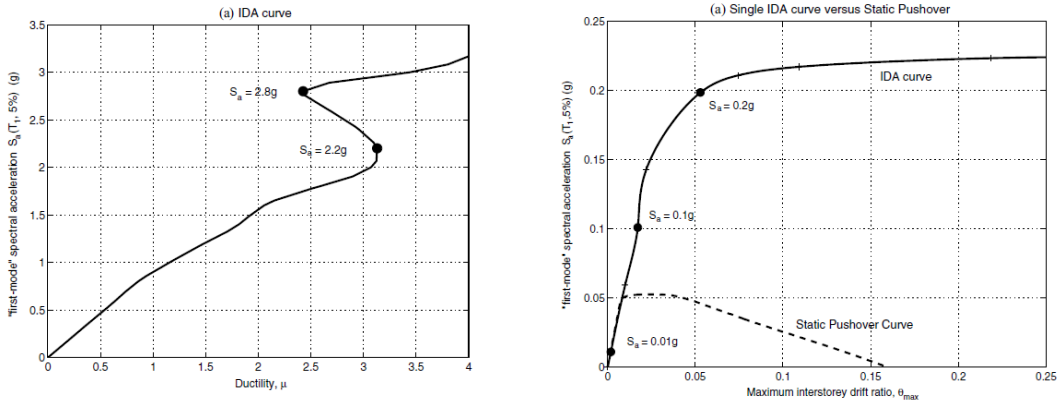

Figure 1.7 Typical Incremental Dynamic Analysis (IDA) curves from the work of Vamvatsikos and Cornell (2002)

CHAPTER 2

PROBLEM DEFINITION

2.1 Seismic Hazard

2.1.1 Selection of acceleration time histories

The fact that the structural damage due to different records from different earthquakes might be different even having the same IM indicates the importance of various characteristics of the input ground motion. Frequency contents, phase, duration etc. have such a significant effect on the performance of the structure that they cannot be ignored.

In order to take into account the effect of each one of these characteristics, 29 real records from earthquakes of varied intensity and characteristics are used as input excitation. These records were used to examine the seismic behavior of two bridges to different excitation levels.

2.1.2 Selection of Intensity Measures (IM) and Damage Potential Indexes (DPI)

The Peak Ground Acceleration (PGA) and Peak Ground Velocity (PGV) are commonly used indices to describe the severity of the earthquake ground motion. However, it is well known that a large PGA is not always followed by severe structural damage, especially for long period structures. Similarly, a large PGV is not always followed by severe structural damage, especially for input motions which include permanent fault displacements. Other indices of earthquake ground motion, e.g., Peak Ground Displacement (PGD), time duration of strong motion (Td), spectrum intensity (SI) , and spectral characteristics, can be considered in damage estimation.

In this direction, a total of nineteen IM's and DPI's were selected each of which describes a different characteristic of the earthquake.

Ten of them (PGA, PGV, PGD, IA, ARMS, VRMS, DRMS, IC, SMA, SMV) which are directly correlated to the acceleration, velocity and displacement time history were calculated first and then were compared and validated with the results of the software SEISMOSIGNAL.

Furthermore another nine DPI's (IH, SE, CAV, ASI, VSI, A95, TP, TMEAN, Dsig) were extruded from SEISMOSIGNAL in order to take into account more parameters of the ground motion. All these parameters are presented in detail and are listed in Table 2.1.

2.2 Seismic Performance of typical motorway bridges

- ### Description of the ''references'' bridges

The present thesis used two bridges from the Greek Metropolitan Motorway ''Attiki Odos''. The first one was the A01_TE20 bridge, which was chosen because it is a simple and the same time common case. Its simplicity lies on the symmetry of the bridge and the circular section of the piers. In addition, each pier consists of a single column which is monolithically connected to the deck while there are bearings at the abutments. The second one was the A01_TE23 bridge and was chosen because it is a more complicated type of bridge which is consisted of four different piers and has five unsymmetrical spans. Also, the two piers have sliding bearings which have an impact on the seismic performance of the bridge only in the longitudinal direction.

- ### Models used

Two-dimensional analytical model was generated using the finite element platform ANSYS. Typical details taken from examined bridge plans were used to generate these models. The superstructure of the bridges is modeled using linear elastic beam elements in a lumped centerline model as shown in Figures 2.1, 2.5

The piers are modeled using also nonlinear beam elements. The hysteretic behavior of the piers is described through the moment-curvature curve. Truss elements of one meter length are used to model the behavior of the bearings in both the transverse and longitudinal direction while linear springs and dampers are used in the vertical direction.

The abutments are ignored in this case and the bearings are considered to be fixed. In order to place the bearings in their exact position, rigid elements were used with selected nodes in the exact place of each bearing. Furthermore in this task the base of the pier is considered fixed and the impact of foundation and soil-structure interaction (SSI) is ignored.

As far as bearings are concerned both in longitudinal and transverse direction truss elements were chosen. The fact that truss elements have both stiffness and damping make them more appropriate solution in comparison to springs and extra dashpots. Moreover by using truss elements it is possible to simulate the nonlinear behavior of the bearings after a certain deformation. Also dashpots are designed with a damping coefficient appropriate for a specific deformation, so truss elements simulate better the behavior of the bearings. Truss elements work with an axial force that depends on their axial strain, so while the value of $\frac{Axial\ deformation}{Length\ of\ truss\ element}$ increases, after a while they do not perform in the expected way.

In order to be sure for the results of our analysis it had to be examined whether or not the expected deformations affects the performance of the truss elements used. For this purpose a pushover analysis was performed in order to extrude the Force-Displacement curve of the truss element. The curve is presented on Figure 2.3. It can be deduced that even for the maximum expected displacements (Takatori records) truss elements of one meter length work appropriately.

- **Piers Section Reinforcement**

a) AO1_TE20

The reinforcement of the piers base circular section (D = 2 m) was calculated according to the provisions of the Greek Code for Reinforced Concrete (ΕΚΩΣ, 2000) for columns with large capacity demands. For acceleration *A* = 0.16 g, considering a (ductility-based) behavior factor *q* = 3 with an elastic (fixed-base) vibration period *T* = 0.55s and soil conditions characterized as "B" the design spectral acceleration is estimated to be: $\Phi_d = 0.13g$.

The computed reinforcement of the pier section was taken from the examined bridge plans [DOMI OE-STATHOPOULOS-FARROS & all.] and for concrete C25 and Steel S500 is:

longitudinal 64Ø25
transverse Ø13/8.6
The section of the pier is presented on Figure 2.2.

b) AO1_TE23

The reinforcement of the piers base circular section (D = 2 m) was calculated according to the provisions of the Greek Code for Reinforced Concrete (ΕΚΩΣ, 2000) for columns with large capacity demands. For acceleration *A* = 0.16 g, considering a (ductility-based) behavior factor *q* = 3 with an elastic (fixed-base) vibration period *T* = 0.70s and soil conditions characterized as "B" the design spectral acceleration is estimated to be: $\Phi_d = 0.13g$.
The computed reinforcement of the piers section was taken from the examined bridge plans [DOMI OE-STATHOPOULOS-FARROS & all.] and for concrete C25 and Steel S500 is:

Pier 1,2 :	Pier 3,4
longitudinal 52Ø25	longitudinal 52Ø25 + 18 Ø20
transverse Ø12/10	transverse: Ø14/10

The section of the pier is presented on Figure 2.6.

- **Moment-Curvature Analysis**

The section is also analyzed using the USC_RC program (Moment-Curvature, Force-Deflection, and Axial Force-Bending Moment Interaction Analysis of Reinforced Concrete Members". University of South California, 2001). The geometric characteristics and the reinforcement of the section used in the analysis are depicted in Figure 2.2.

The Mander model (Mander et al., 1984) is used to simulate the stress–strain relationship of confined concrete. The analysis doesn't take into account the hardening behavior of steel and the material strength values refer to the design values (fcd, fsd).

The moment curvature relationship for the pier section as derived from the analysis with the USC_RC program, considering the softening behavior of concrete, is shown in Figure 2.3.

The point of "failure", when the ultimate moment capacity is reached, is highlighted in the diagram as well as the point when yielding initiates (εy = fy/Es ≈0.002).

2.3 Modeling bridge's components

2.3.1 Bearing's stiffness

The first component of the bridge that is taken into account is the bearings. As in the model of the whole bridge the abutments are fixed, the impact of bearings is specified on their stiffness while damping will be examined in the following section. The stiffness of the specific spring is equal to the stiffness of the four bearings of the one abutment.

$$K_{spring} = 4 * K_{Bearing} = 5200 \frac{KN}{m}$$

The stiffness of the bearing is calculated by the following equation:

$$K_{bearing} = n * \frac{G * A}{t}$$

assuming the following parameters:

- n : number of bearings
- G : 1 MPa
- A : section area of bearing
- t : thickness of elastic part of bearing

2.3.2 Bearing's damping

The damping coefficient of the dashpot that represents the damping of the four bearings of the abutment is calculated by the following equation:

$$c_{bearing} = \frac{2 * k * \xi}{\omega}$$

assuming the following parameters:

- K : stiffness of bearings
- ξ : 5%
- ω_{bridge} : $2\pi/T_{bridge\ long}$

2.3.3 Deck's rotational stiffness

The rotational stiffness of the deck can be calculated with one of the known methods of structural analysis if you consider the deck of the bridge as a continuous beam with simply supports at the top of the piers and the bearings of the abutments.

In this case that the deck is considered as a three equal span continuous beam (TE 20), the rotational (bending) stiffness of the deck is calculated by the following formula:

$$K_{rotational} = \frac{9EI}{L}$$

assuming the following parameters:

- E=30000000 KPa, the Young's elastic modulus
- I=2.72 m^4, the I_{11}moment of inertia of the deck
- L=31 m, the length of each span (TE 20)

2.3.4 Deck's damping

The last parameter that was taken into account was the damping of the material of the bridge's deck. The damping coefficient of the dashpot that represents the damping of the material of the deck is calculated by the following equation:

$$c_{deck\ rotational} = \frac{2 * k * \xi}{\omega}$$

assuming the following parameters:

- K :rotational stiffness of deck
- ξ : 5%
- ω_{bridge} : $2\pi/T_{bridge\_long}$

Chapter 2

Figures

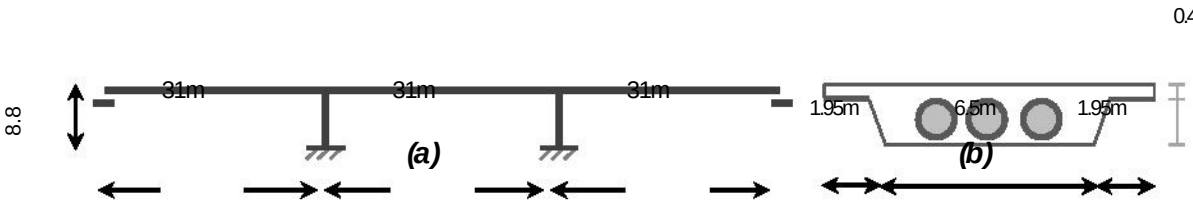

Figure 2.1 (a) geometry of the bridge and **(b)** section of the deck

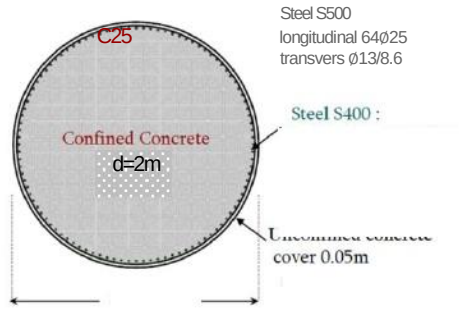

Figure 2.2
The geometric characteristics
and the reinforcement of pier's section

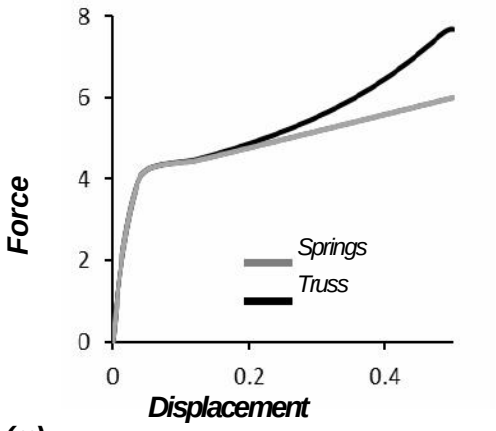

Figure 2.3
Pushover analysis comparison between
bearing as linear springs and
truss elements

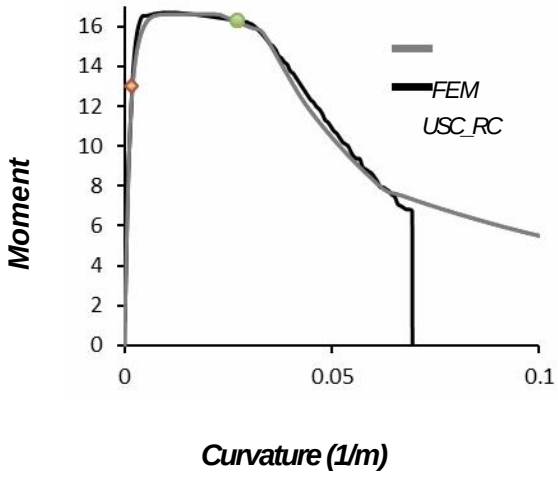

Figure 2.4 Comparison of moment-curvature curves using
USC_RC program and calibrated finite element
model

	SEISMIC PERFORMANCE					
	max Drift (m)	***maxDrift ratio (%)***	***Drift res (m)***	***Drift res ratio(%)***	***μdemand***	***μd/μc***
TAKATORI_000	8.20	93.23	5.16	58.59	2199.26	184.81
JMA_090	2.72	30.95	2.72	30.95	438.17	36.82
MNSA	0.02	0.28	0.00	0.01	0.44	0.04
KALAMATA	0.07	0.81	0.05	0.62	1.92	0.16
TCU68NS	8.19	93.07	3.86	43.88	2077.64	174.59
RINALDI_228	0.36	4.05	0.20	2.29	15.98	1.34
SYLMAR_360	0.31	3.53	0.06	0.73	13.55	1.14
TAKATORI_090	8.20	93.23	5.66	64.36	2245.35	188.69
JMA_000	0.20	2.26	0.05	0.55	8.98	0.75
TAKARAZUKA_090	0.18	2.09	0.05	0.60	9.27	0.78
PYRGOS	0.03	0.29	0.00	0.04	0.46	0.04
AEGIO	0.05	0.62	0.00	0.03	1.24	0.10
LEFKADA_2003	0.10	1.15	0.06	0.74	3.06	0.26
LEFKADA_1973	0.15	1.73	0.13	1.52	6.46	0.54
TCU52EW	8.18	93.01	2.96	33.62	1854.96	155.88
TCU52NS	0.36	4.13	0.01	0.11	19.02	1.60
TCU68EW	8.18	92.95	0.30	3.36	2955.09	248.33
RINALDI_318	0.28	3.16	0.13	1.51	17.75	1.49
JENSEN_292	8.16	92.73	3.05	34.66	2009.33	168.85
JENSEN_022	0.38	4.33	0.38	4.26	42.86	3.60
SYLMAR_090	0.27	3.03	0.23	2.58	16.19	1.36
DUZE_000	0.15	1.67	0.11	1.23	7.04	0.59
YARIMCA_060	0.16	1.77	0.14	1.60	7.92	0.67
YARIMCA_330	0.22	2.44	0.20	2.27	12.47	1.05
SAKARYA	0.07	0.74	0.01	0.12	2.57	0.22
LUCERNE_000	0.05	0.55	0.01	0.06	1.01	0.08
IV#04_140	0.17	1.89	0.16	1.82	8.61	0.72
IV#04_230	0.27	3.05	0.24	2.74	15.43	1.30
DUCE_090	0.17	1.95	0.16	1.82	7.68	0.6

Table 2.2 Seismic performance of pier of bridge A01_TE20

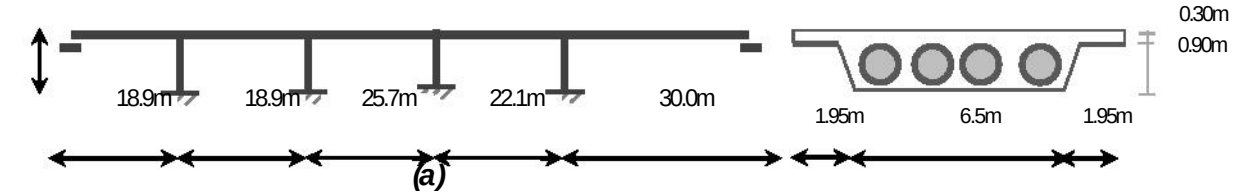

8.8

Figure 2.5 (a) geometry of the bridge and **(b)** section of the deck

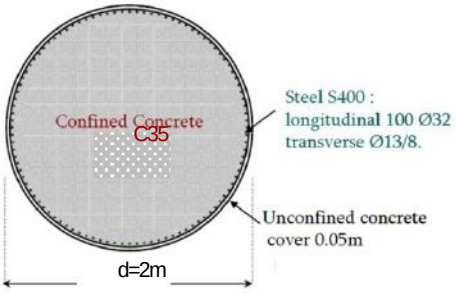

Figure 2.6 Geometric characteristics and reinforcement of pier's section

(b)

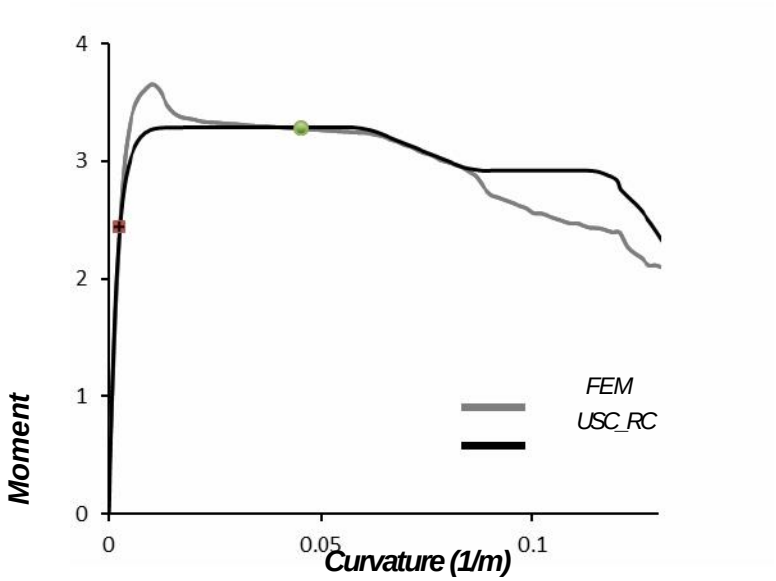

Figure 2.7 Comparison of moment-curvature curves using USC_RC program and calibrated finite element model

	SEISMIC PERFORMANCE					
	max Drift (m)	maxDrift ratio (%)	Drift res (m)	Drift res ratio(%)	μdemand	μd/μc
TAKATORI_000	0.54	4.94	0.51	4.65	20.92	1.57
JMA_090	0.31	2.79	0.28	2.57	13.16	0.99
MNSA	0.02	0.21	0.00	0.00	0.35	0.03
KALAMATA	0.06	0.58	0.04	0.35	1.24	0.09
TCU68NS	0.35	3.19	0.23	2.14	21.54	1.62
RINALDI_228	0.32	2.94	0.09	0.78	13.16	0.99
SYLMAR_360	0.29	2.67	0.12	1.07	11.70	0.88
TAKATORI_090	0.50	4.50	0.48	4.39	18.44	1.39
JMA_000	0.19	1.76	0.00	0.01	7.71	0.58
TAKARAZUKA_090	0.18	1.65	0.04	0.35	8.21	0.62
PYRGOS	0.03	0.24	0.00	0.04	0.40	0.03
AEGIO	0.05	0.50	0.00	0.03	0.99	0.07
LEFKADA_2003	0.09	0.82	0.05	0.48	2.16	0.16
LEFKADA_1973	0.16	1.44	0.13	1.15	6.03	0.45
TCU52EW	0.40	3.63	0.02	0.18	19.24	1.45
TCU52NS	0.32	2.90	0.18	1.61	15.46	1.16
TCU68EW	0.84	7.67	0.84	7.65	57.01	4.29
RINALDI_318	0.24	2.14	0.02	0.17	11.53	0.87
JENSEN_292	0.47	4.24	0.41	3.75	25.27	1.90
JENSEN_022	0.32	2.91	0.27	2.47	16.01	1.20
SYLMAR_090	0.22	1.96	0.17	1.57	11.51	0.87
DUZE_000	0.14	1.32	0.08	0.69	6.21	0.47
YARIMCA_060	0.14	1.30	0.11	1.04	5.87	0.44
YARIMCA_330	0.15	1.35	0.08	0.70	7.12	0.54
SAKARYA	0.07	0.60	0.02	0.15	1.32	0.10
LUCERNE_000	0.05	0.44	0.00	0.02	0.83	0.06
IV#04_140	0.13	1.21	0.10	0.87	5.39	0.41
IV#04_230	0.21	1.94	0.14	1.26	10.53	0.79
DUCE_090	0.17	1.57	0.14	1.26	6.59	0.50

Table 2.3 Seismic performance of pier of bridge A01_TE23

CHAPTER 3

DEVELOPMENT OF 3D MODEL

EFFECT OF SOIL-STRUCTURE INTERACTION

3.1 Development of 3D model

In the previous chapter the impact of the various components of a bridge on its seismic performance was examined and simple models were developed to describe the seismic performance of a whole bridge both in longitudinal and transverse direction. However in all the previous analyses the base of the piers was considered fixed so as the connection of the bearings to the abutments. In this way the effect of soil-structure interaction (SSI) was ignored so as the impact of the retaining walls and the embankments at the abutments to the performance of the whole bridge system. In this chapter a three-dimensional analytical model of the whole bridge system (soil, footings, piers, deck, bearings, retaining walls, access embankments) is generated (Figure 3.1) in order to examine the effect of the previous factors and to develop if necessary new simple models that take into account all the above.

3.1.1 Modeling bridge's deck and piers

The bridges selected were the A01_TE20 and A01_TE23 bridge of the Greek Metropolitan Motorway ''ATTIKI ODOS'' the same that was used at the previous analyses in order to compare the results. The reason that led to this choice at the first place was that it is a simple and at the same time common case. Its simplicity lies in the symmetry of the bridge and the circular section of the piers. Also each pier consists of a single column which is monolithically connected to the deck while there are bearings at the abutments. The model of the bridge used is the same and is described in detail at chapter 2.

3.1.2 Modeling bridge's footings

Unlike the approach of chapter 5 that the base of the bridge's piers is considered fixed, in this chapter the soil-foundation system is taken into account. The piers of the bridge are connected at their base to a shallow foundation.

More specific a square footing of 8 m width and 2 m height is considered for the base of each pier which was taken from the examined bridge plans. The footings of the piers are modeled in the finite element code ABAQUS using elastic (8-node) continuum elements (C3D8) and are shown in Figure 6.2 (c).

3.1.3 Modeling retaining walls at the abutments

The abutments of the bridge system consist of retaining walls that retain the access embankments, the exact dimensions of which were taken from the examined bridge plans. More specific each wall is of 9 m height and 1.5 m thickness. It is also connected to two side walls of 0.6 m thickness that retain the sides of the embankment. In addition each wall is founded on a rectangular footing of 7 m x 10.4 m and 1.5 m height. Both the retaining walls of the abutments and their footings are modeled in the finite element code ABAQUS using elastic (8-node) continuum elements (C3D8) and are shown in Figure 3.2 (b). The only component of the constructed bridge of Attiki Odos that has not been modeled is the stoppers at the abutments. The reason for this choice is that their impact on the seismic performance of the bridge is dominant and as a result the effect of the rest structural components cannot be examined properly.

3.1.4 Modeling subject soil and embankments

The main objective of this chapter is to examine the effect of soil-structure interaction on the seismic performance of a certain bridge. As a result it is necessary to model the soil subject to the bridge as well as the soil of the embankments at its abutments. For this purpose an idealized homogeneous 20 m stiff clay layer, of undrained shear strength Su=150 kPa is used which is representative soil conditions for which a surface foundation would be a realistic solution. The properties of the soil used are shown on Figure 3.3. The same stiff clay is also used for the embankments, which is not a very realistic approach but it is not of great importance for our purpose. The subject soil and the soil of the embankments are modeled in the finite element code ABAQUS using nonlinear (8-node) continuum elements (C3D8) and are shown in Figure 3.2 (a).

- **Soil behavior**

Soil behavior is modeled through a nonlinear kinematic hardening constitutive model, with a Von Mises failure criterion and associated plastic flow rule (Anastasopoulos et al., 2011). According to the Von Mises failure criterion, the evolution of stresses is described by the relation:

$$\sigma = \sigma_0 + \alpha \quad (1)$$

where σ_0 is the value of stress at zero plastic strain, assumed to remain constant. The parameter α is the "backstress", which defines the kinematic evolution of the yield surface in the stress space. An associated plastic flow rule is assumed:

$$\dot{\varepsilon}^{pl} = \dot{\bar{\varepsilon}}^{pl} \frac{\partial F}{\partial \sigma} \quad (2)$$

where $\dot{\varepsilon}^{pl}$ is the plastic flow rate (obtained through the equivalent plastic work), $\dot{\bar{\varepsilon}}^{pl}$ the equivalent plastic strain rate, and *F* a function defining the pressure-independent yield surface:

$$F = f(\sigma - \alpha) - \sigma_0 \quad (3)$$

The evolution law of the model consists of two components: a nonlinear kinematic hardening component, which describes the translation of the yield surface in the stress space (defined through the backstress α), and an isotropic hardening component, which describes the change of the equivalent stress defining the size of the yield surface σ_0 as a function of plastic deformation. The kinematic hardening component is defined as an additive combination of a purely kinematic term (linear *Ziegler* hardening law) and a relaxation term (the *recall* term), which introduces the nonlinearity.

The evolution of the kinematic component of the yield stress is described as follows:

$$\dot{\alpha} = C \frac{1}{\sigma_0} (\sigma - \alpha) \ - \gamma \alpha \quad (4)$$

where C the initial kinematic hardening modulus ($C = \sigma_y / \varepsilon_y = E$) and γ a parameter that determines the rate at which the kinematic hardening decreases with increasing plastic deformation.

The evolution of the kinematic and the isotropic hardening components is illustrated in Figures 3.4 (a), (b) and c for unidirectional and multiaxial loading, respectively. The evolution law for the kinematic hardening component implies that the backstress is contained within a cylinder of radius:

$$\sqrt{\frac{2}{3}a^s} = \sqrt{\frac{2}{3}\frac{C}{\gamma}} \quad (5)$$

where α^s is the magnitude of α at saturation. Since the yield surface remains bounded, this implies that any stress point must lie within a cylinder of radius $\sqrt{2/3}\,\sigma_y$. At large plastic strains, any stress point is contained within a cylinder of radius $\sqrt{2/3}\,(\alpha^s + \sigma^s)$ where σ^s is the equivalent stress defining the size of the yield surface at large plastic strain. The maximum yield stress (at saturation) is:

$$\sigma_y = \frac{C}{\gamma} + \sigma_0 \quad (6)$$

According to the Von Mises yield criterion this ultimate stress is:

$$\sigma_y = \sqrt{3}S_u \quad (7)$$

From Eqs. 6 and 7 we have:

$$\gamma = \frac{C}{\sqrt{3}S_u - \sigma_0} \quad (8)$$

Model parameters are calibrated (Anastasopoulos et al., 2011) to fit published G–γ curves of the literature, following the procedure described in Gerolymos & Gazetas (2005). Figure 3.4 (c) illustrates the validation of the kinematic hardening model (through simple shear finite element analysis) against published G–γ curves by Ishibashi and Zhang (1993).

- **Mesh of the soil model**

The final 3D model of the subject soil is of 155 m length, 40 m width and 20 m depth. The soil model is divided into three volumes: The first volume is a very fine mesh under both footings of 16 m (2B) length and width and 20 m (2.5B) depth, where B is the width of the footing. The elements of this volume are of 0.8 m length and width and 1 m height for the upper 10 m depth of the soil model and of 2 m height for the rest 10 m depth of the first volume. The second volume is an also very fine mesh under the two embankments of the abutments of 37 m length, 16 m width and 20 m depth. The elements of this volume are of 1 m length, 0.92 m width and 1 m height for the upper 10 m depth of the soil model and of 2 m height for the rest 10 m depth of the second volume. The third volume contains the rest of the subject soil model and consists of cubic elements of 2 m length, width and height. As far as the soil of the embankments is concerned, a 3D soil model is also generated in the finite element code ABAQUS of 30 m length, 9.2 m width and 10.5 m depth for each embankment. The elements of this model are of 1 m length, 0.92 m width and 1 m height. The whole 3D soil model as generated in ABAQUS consists of about 50000 elements and is shown in figure 6.1.

- **Boundaries of the soil model**

The boundaries of the soil model are placed far enough from the bridge model in order not to affect the results of the analysis. In particular ‘’free-field’’ boundaries responding as shear beams are placed at each lateral boundary of the subject soil model and of the embankments, to reproduce free-field conditions. In addition reflections at the base of the formation are avoided by utilizing absorbing boundaries. More specific dashpots are placed under the base of the soil model which damping coefficient is calculated by the following equation:

$$c_{base} = \rho * A * Vs$$

assuming the following parameters:

- ρ=1.6 Mgr/m³, the density of the clay layer
- A, the area of each element of the base
- Vs=255m/s, the shear wave velocity

Due to the fact that for the calculation of the damping coefficient of the dashpot you need to know the area of each element of the base, two different kind of dashpots are used, one for the very fine mesh where the area of each element of the base is A=0.64 m² and one for the rest of the soil base where the area of each element is A=4 m². The kind of dashpots used are node to node ones and are connected to the nodes of the soil base and to some extra nodes defined which are placed 1 m lower from the soil base. All degree of freedoms of the latter are fixed, while at the nodes of the soil base only the vertical displacement degree of freedom is fixed. The seismic excitation is imposed at the fixed nodes of the dashpots of the soil base.

- **Soil-footing and retaining wall-embankment interfaces**

At the soil-footing and retaining wall-embankment interfaces contact elements are placed. The coefficient of friction at these interfaces is μ=0.7 that allows only small sliding of the foundation and the wall.

3.2 Effect of soil-structure interaction

3.2.1 Seismic performance of 3D model

The seismic performance of the 3D model of the entire bridge-soil system as developed in the finite element code ABAQUS was tested under nonlinear dynamic time history analysis using 3 real earthquake records: One of low intensity (Aegio record), one of moderate intensity (Lefkada_2003 record) and one severe earthquake excitation (Rinaldi_228 record).

The 3D model was tested in both longitudinal and transverse direction. The results of the seismic performance of the different components of the 3D model are presented below for the Rinaldi_228 record in both directions.

- **Soil amplification**

There are two alternative ways to impose the seismic excitation. The first is to consider a fixed soil base (bedrock) and impose the seismic excitation there. The second is to consider dashpots at the soil base and to impose the seismic excitation at the fixed nodes of the dashpots below the soil base. The acceleration time histories for the Aegio record for both considerations at the fixed base and at the surface of the soil layer are presented in Figures 3.5 (a), (b) , (c), (d) for both longitudinal and transverse direction. From the comparison of the two alternatives it is concluded that the most realistic approach is the one with the dashpots at the soil base so this is the one that is finally used. In addition from the comparison of the acceleration time histories for the Rinaldi_228 record at the surface of the subject soil and the surface of the embankment that is shown in Figures 3.6 (a), (b), the additional soil amplification is obvious.

- **Effect of SSI in the natural period of the bridge**

In the previous chapter the base of bridge's piers so as the connections of the bearings at the abutments were considered fixed. The natural period of the bridge system with the fixed base consideration is T=0.55 sec in the longitudinal direction and T=0.66 sec in the transverse.

However taking into account the soil-structure interaction it increases to T=0.69 sec in the longitudinal direction and to T=0.78 sec in the transverse. The natural period of the bridge considering soil-structure interaction can be calculated using the equation:

$$T_{ssi} = T_{fixed}\sqrt{1 + \frac{K_{str}}{K_H} + \frac{K_{str}}{K_R}H^2}$$

assuming the following parameters:

- T_{fixed}: the natural period of the superstructure with the fixed base consideration
- K_{str}: the stiffness of the superstructure
- K_H: the stiffness of the horizontal spring that replaces the soil-foundation system
- K_R: the stiffness of the rotational spring that replaces the soil-foundation system
- H: the height of the superstructure

- **Seismic performance of soil-foundation system**

The seismic performance of the whole bridge system depends greatly on the seismic performance of the soil-foundation system. In this case each pier of the bridge is connected at its base to a square footing of 8 m width which is designed according to the provisions of the Greek Code for Reinforced Concrete (ΕΚΩΣ, 2000). The factor of safety (Fs) of the particular soil-footing system against vertical loading is Fs=6.7. Its seismic performance for the Rinaldi_228 record in both directions is described by the Moment-Rotation and Settlement-Rotation curves that are shown in Figures 3.7 (a), (b) , 3.8 (a), (b). These curves refer to the center point of the soil-footing interface. In addition from the relative horizontal displacement time histories between the footing and the soil that are shown in Figures 3.7 (c), 3.8 (c) for both directions, it is obvious that there is practically no sliding of the footing.

- **Seismic performance of retaining walls**

Each abutment of the 3D bridge-soil model consists of a retaining wall that retains the access embankment. One of the key objectives of this chapter is to examine the effect of the seismic performance of the retaining wall to the performance of the whole bridge system. The seismic performance of each retaining wall for the Rinaldi_228 record in both directions is described by the Settlement-Rotation curves that are shown in Figures 3.9(a), 3.10(a). These curves refer to the center point of the subject soil - retaining wall interface. In addition the relative horizontal displacement time histories between the wall and the deck of the bridge in both directions are shown in Figures 3.9(b), 3.10(c).

From these curves it is concluded that both retaining walls don't have significant displacements in comparison to the deck, so the consideration of fixed abutments is a logical and realistic approach.

- **Seismic performance of superstructure**

The present thesis focuses mainly on the structural damage of the superstructure. For this reason great emphasis is given to the seismic performance of the bridge and its components (deck, piers and bearings). The performance of bridge's piers is described for the Rinaldi_228 record in both directions by the Moment-Curvature curve at the base of each pier and the Relative Displacement time histories at the top of each pier, which are shown in Figures 3.11, 3.12. In these figures it is also shown the drift limit at which the stoppers of the bridge at the abutments begin to affect its seismic performance. The structural damage of the piers is expressed in terms of Maximum Drift, Residual Drift and in terms of ductility $\frac{\mu_{demand}}{\mu_{capacity}}$ which can be extruded from the above curves. These values for the Rinaldi_228 record and for both piers and directions are presented in Table 3.1. The deck's seismic performance for the same record in both directions is described by the Moment curves at the time of maximum drift, which are presented in Figures 3.13 (a) and (b), while the performance of the bearings is described by the Relative Displacement time histories of the truss elements that represent the bearings and are shown in Figures 3.13 (c) and (d).

- **Contact pressures at the retaining wall-embankment interface**

The contact pressure time histories at each retaining wall-embankment interface and at different heights for the Rinaldi_228 record in the longitudinal direction are presented in Figure 3.14. These curves refer to the center point of the wall-embankment interface. From the above curves it is obvious that the soil of the abutment is cohesive (clay) as at certain moments and heights the contact pressures drop to zero, which means that the contact between the soil of the embankment and the wall is lost. This is a classic cohesive soil behavior. If the soil of the embankment was sand (noncohesive soil) then these zero values would be less and would appear mainly at the highest points of the interface (top of the wall) as the sand ''follows'' the movement of the wall and ''fills'' the gaps. From the above curves it is also obvious that the two retaining wall-embankment systems at the abutments of the bridge perform different during the earthquake.

The observed differences are expected due to the fact that the seismic excitation is imposed in the horizontal direction and as a result the soil layer behind the wall develops passive earth pressure in one abutment and at the same time active earth pressure at the other.

3.2.2 Comparison between fixed base simple model and complete 3D model Effect of soil-structure interaction

In the 2nd chapter simple models were developed that have similar seismic performance to the entire 3D bridge system with the consideration of fixed base conditions. So in this chapter in order to examine the effect of soil-structure interaction the seismic performance of the entire 3D bridge-soil model is compared to the whole 3D bridge system. Both the simple model and the complete 3D model were tested under nonlinear time history analysis using three real earthquake records: One of low intensity (Aegio record), one of moderate intensity (Lefkada_2003 record) and one severe earthquake excitation (Rinaldi_228 record). The seismic excitation imposed at the fixed base of the simple models is the acceleration time history at the surface of the soil as resulted from the analysis of the complete model. Finally the same input acceleration time history is imposed to both the base of the piers and the fixed nodes of the horizontal spring and dashpot. In this way the abutments of the bridge are considered fixed.

This is a logical assumption, as explained before, due to the fact that the retaining walls don't have significant displacements in comparison to the deck of the bridge.

As shown in Figures 3.11, 3.12 in the complete model both piers have the same seismic performance in terms of Relative Displacement time history at the top of the pier and Moment-Curvature curve at the base of the pier. So one of them is selected and compared to the simple model. The results of the analysis and the comparison between the simple fixed base model and the complete one in each direction are presented below.

- **Longitudinal direction**

The seismic performance of both the complete model and the simple one is described by the Relative Displacement time histories at the top of the pier and the Moment-Curvature curves at the base of the pier. The above curves for each earthquake record and for both models are presented in Figures 3.15, 3.16. Structural damage of the piers is expressed in terms of Maximum Drift, Residual Drift and in terms of ductility $\frac{\mu_{demand}}{\mu_{capacity}}$ which are extruded from the above curves. These values for each earthquake record and for both models are shown in Table 3.2. In this case for the 2 of the 3 records that demanded less ductility than the capacity of the system, the maximum deviation observed in terms of $\frac{\mu_{demand}}{\mu_{capacity}}$ is 27%, while the average deviation is 19%.

- **Transverse direction**

The seismic performance of both the complete model and the simple one in the transverse direction is also described by the Relative Displacement time histories at the top of the pier and the Moment-Curvature curves at the base of the pier. The above curves for each earthquake record and for both models are presented in Figures 3.17, 3.18. Structural damage of the piers is expressed in terms of Maximum Drift, Residual Drift and in terms of ductility $\frac{\mu_{demand}}{\mu_{capacity}}$ which are extruded from the above curves. These values for each earthquake record and for both models are shown in Table 3.3. In this case for the 2 of the 3 records that demanded less ductility than the capacity of the system, the maximum deviation observed in terms of $\frac{\mu_{demand}}{\mu_{capacity}}$ is 15%, while the average deviation is 9%.

- **Effect of soil-structure interaction**

From the comparison of the fixed base simple model with the complete 3D bridge-soil model in both directions it can be concluded that the effect of soil-structure interaction in the structural damage of the piers and in general in the seismic performance of the superstructure is important and cannot be ignored. More specific it is observed that its effect is beneficial for the superstructure in comparison to the fixed base approach, as it reduces the structural damage of the piers and the ductility demanded by the earthquake. Therefore the following step is to extend the previous simple models in each direction in order to take into account the soil-structure interaction by using springs and dashpots to replace the soil-foundation system.

3.2.3 Use of linear elastic springs and dashpots to consider SSI

The simplest way to take into account the soil-structure interaction is to replace the soil-foundation system by using linear elastic springs and dashpots (Gazetas, 1983). More specific at the base of the simple model horizontal, vertical and rotational springs and dashpots are added to represent the horizontal, vertical and rotational stiffness and damping of the soil-foundation system.

The stiffness of the vertical linear elastic spring is calculated by the following equation (Gazetas, 1983):

$$K_V = \frac{4.54Gb}{1-\nu}$$

assuming the following parameters:

- G=103846 KPa, the shear modulus of elasticity of the soil
- b=B/2=4m, where B is the width of the footing
- v=0.3, the Poisson's ratio

The damping coefficient of the vertical dashpot is calculated by the following equation (Gazetas, 1983):

$$C_V = \frac{2K_V\xi}{\omega}$$

assuming the following parameters:

- K_V=2694066 KN/m, as calculated using the previous equation
- ξ=5%
- $\omega = 2\pi/T_{SSI}$, where T_{SSI} is the natural period of the bridge system in the examined direction considering SSI

The stiffness of the horizontal linear elastic spring is calculated by the following equation (Gazetas, 1983):

$$K_H = \frac{9Gb}{2-\nu}$$

assuming the following parameters:

- G=103846 KPa, the shear modulus of elasticity of the soil
- b=B/2=4m, where B is the width of the footing
- v=0.3, the Poisson's ratio

The damping coefficient of the horizontal dashpot is calculated by the following equation (Gazetas, 1983):

$$C_H = \frac{2K_H\xi}{\omega}$$

assuming the following parameters:

- K_H=2199095 KN/m, as calculated using the previous equation
- ξ=5%
- $\omega = 2\pi/T_{SSI}$, where T_{SSI} is the natural period of the bridge system in the examined direction considering SSI

The stiffness of the rotational linear elastic spring is calculated by the following equation (Gazetas, 1983):

$$K_R = \frac{3.65Gb^3}{1-\nu}$$

assuming the following parameters:

- G=103846 KPa, the shear modulus of elasticity of the soil
- b=B/2=4m, where B is the width of the footing
- v=0.3, the Poisson's ratio

The damping coefficient of the rotational dashpot is calculated by the following equation (Gazetas, 1983):

$$C_R = \frac{2K_R\xi}{\omega}$$

assuming the following parameters:

- K_R=34654945 KNm/rad, as calculated using the previous equation
- ξ=5%
- $\omega = 2\pi/T_{SSI}$, where T_{SSI} is the natural period of the bridge system in the examined direction considering SSI

Due to the change in the natural period of the bridge system considering soil-structure interaction, the damping coefficients of the dashpots that are used in the simple model to represent the different components of the superstructure are also changed.

Both the new simple models and the complete 3D model are tested in both directions under nonlinear time history analysis using the same three real earthquake records. The seismic excitation is imposed at the fixed nodes of the springs and the dashpots that replace the soil-foundation system and the fixed node of the horizontal spring and dashpot that represents the stiffness and damping of the bearings.

The input seismic excitation is again the acceleration time history at the surface of the soil as resulted from the analysis of the complete model. The results of the analysis and the comparison between the simple model and the complete one in each direction are presented below.

- **Longitudinal direction**

The seismic performance of both the complete model and the simple one is described by the Rotation time histories of the footing, the Relative Displacement time histories at the top of the pier and the Moment-Curvature curves at the base of the pier. The above curves for each earthquake record and for both models are presented in Figures 3.19, 3.20.

Structural damage of the piers is expressed in terms of Maximum Drift, Residual Drift and in terms of ductility $\frac{\mu_{demand}}{\mu_{capacity}}$ which are extruded from the above curves. These values for each earthquake record and for both models are shown in Table 3.4. In this case for the 2 of the 3 records that demanded less ductility than the capacity of the system, the maximum deviation observed in terms of $\frac{\mu_{demand}}{\mu_{capacity}}$ is 18%, while the average deviation is 12%. The maximum deviation is 9% less than the fixed base approach, while the average is 7% less.

- **Transverse direction**

The seismic performance of both the complete model and the simple one in the transverse direction is also described by the Rotation time histories of the footing, the Relative Displacement time histories at the top of the pier and the Moment-Curvature curves at the base of the pier. The above curves for each earthquake record and for both models are presented in Figures 3.21, 3.22. Structural damage of the piers is expressed in terms of Maximum Drift, Residual Drift and in terms of ductility $\frac{\mu_{demand}}{\mu_{capacity}}$ which are extruded from the above curves. These values for each earthquake record and for both models are shown in Table 3.5. In this case for the 2 of the 3 records that demanded less ductility than the capacity of the system, the maximum deviation observed in terms of $\frac{\mu_{demand}}{\mu_{capacity}}$ is 9%, while the average deviation is 8%. The maximum deviation is 6% less than the fixed base approach, while the average is 1% less.

- **Evaluation of the use of linear elastic springs and dashpots to consider SSI**

From the previous analysis it can be concluded that the use of linear elastic springs and dashpots to replace the soil-foundation system is considered a satisfactory approach for the particular soil-foundation system and for the purposes of the present thesis. The deviations in the structural damage of the superstructure between this approach and the analysis of the entire 3D bridge-soil model are insignificant in comparison to the uncertainties in the properties of the subject soil. However for the sake of completeness a more accurate approach of replacing the soil-foundation system with springs and dashpots is considered in the following section.

3.2.4 Combination of linear elastic and nonlinear springs and dashpots to consider SSI

One more accurate way to take into account the soil-structure interaction is to replace the soil-foundation system by using a combination of linear elastic and nonlinear springs and dashpots (Anastasopoulos & Kontoroupi, 2013). More specific at the base of the simple model horizontal, vertical and rotational springs and dashpots are added to represent the horizontal, vertical and rotational stiffness and damping of the soil-foundation system as before. The horizontal and vertical springs and dashpots are considered linear elastic and have the same stiffness and damping coefficient as in the previous approach, while a nonlinear rotational spring accompanied by a linear rotational dashpot is added to the simple model calculated according to the methodology described in Anastasopoulos & Kontoroupi (2013). The basic steps of this methodology are presented below.

3.2.4.1 Moment-Rotation Relations

To define the necessary relations to implement this methodology, the *M*–ϑ response of the soil-foundation system is divided in three characteristic phases, which are described in detail in the next sections: (a) quasi–elastic response (for very small rotation $\vartheta \rightarrow 0$), (b) plastic response (referring to the ultimate capacity, for large rotation ϑ) and (c) nonlinear response (which is the intermediate stage between the quasi-elastic and the plastic phases).

- **Quasi–elastic response**

The first phase of response refers to very small rotation ϑ. The effective (secant) rotational stiffness is a function of ϑ and F_S: $K_R = f(\theta, F_S)$. For a given factor of safety F_S, the initial (i.e., for $\vartheta \rightarrow 0$) rotational stiffness can be defined as:

$$K_{R,0} = K_R(0, F_S) \quad (1)$$

As shown in Figure 3.23, for the lightly-loaded (F_S= 10) footing, $K_{R.0}$ is very close to the purely elastic rotational stiffness (Gazetas, 1983):

$$K_{R,elastic} = \frac{3.65Gb^3}{1-\nu} \quad (2)$$

where *b* = *B*/2, *G* is the small strain shear modulus of soil, and *v* the Poisson's ratio. In stark contrast, a substantial difference is observed for the heavily-loaded (F_S = 2) footing. This reduction of $K_{R,0}$ is directly related to the initial soil yielding due to the imposed vertical load *N* (before application of moment loading). Based on the 3D FE analysis results, $K_{R,0}$ can be (approximately) expressed as:

$$K_{R,0} = K_{R,elastic}(1 - 0.8\frac{1}{F_S}) \quad (3)$$

- **Plastic response**

This phase refers to the ultimate capacity of the footing, and is quite straight-forward to define. As thoroughly discussed in Gazetas et al. (2012), the failure envelope can be defined as follows (Figure 6.24):

$$\frac{M_u}{N_{uo}B} = 0.55\left(\frac{N_u}{N_{uo}}\right)\left(1-\frac{N_u}{N_{uo}}\right) \quad (4)$$

where N_{uo} is the bearing capacity for purely vertical loading (Meyerhof, 1953; Gourvenec, 2007):

$$N_{uo} \approx (\pi+3)S_u B^3 \quad (5)$$

- **Nonlinear response**

This corresponds to the intermediate phase, bridging the gap between the quasi-elastic and plastic response. If the soil behaved as an ideally elastic–plastic material, there would be no need to consider this intermediate phase of response, and the previously described solutions would be enough to completely define the necessary *M*–*ϑ* relations. However, as revealed by Figure 3.23, the soil–foundation system exhibits strongly nonlinear response long before reaching its ultimate capacity. Hence, there is a need for a "connection" between the quasi-elastic and the plastic part of the *M*–*ϑ* relations. This is performed on the basis of 3D FE analysis results, following the dimensional formulation presented in Kourkoulis et al. (2012a) and Gazetas et al. (2012).

As shown in Figure 3.23, the initiation of the nonlinear phase is a function of *Fs*. While the lightly-loaded (*Fs* = 10) footing starts exhibiting nonlinear response for *ϑ* ≈ 0.02 x 10-2 rad, in the case of the heavily-loaded (*Fs* = 2) nonlinearity becomes observable much later, for *ϑ* ≈ 0.08 x 10-2 rad. This difference is due to the vertical load *N* acting on the foundation, the increase of which tends to hinder separation and uplifting. In the absence of soil nonlinearity, considering a footing (of any shape) rocking on elastic half-space, the overturning moment to initiate uplifting would be (Apostolou & Gazetas, 2007):

$$M_{uplift} \approx \frac{NB}{4} \quad (6)$$

where *B* is the width of the footing in the direction of rocking. Therefore, the uplifting rotation *ϑuplift* can be defined as:

$$\theta_{uplift} \approx \frac{NB}{4K_{R,elastic}} \quad (7)$$

As previously discussed, the initial quasi-elastic rotational stiffness $K_{R,0}$ decreases with the decrease of F_S due to the increasingly important initial soil yielding (due to the vertical load *N*, before application of moment loading). Therefore, when considering soil inelasticity it is reasonable to assume that the equivalent "uplifting" rotation will be a function of $K_{R,0}$ rather than $K_{R,elastic}$. Hence, combining Eq. 3 and Eq. 7, a characteristic rotation θ_S is defined:

$$\theta_S \approx \frac{NB}{4K_{R,0}} = \frac{NB}{4K_{R,elastic}(1-0.8\frac{1}{F_S})} \quad (8)$$

As shown in Figure 3.25 (a), θ_S can be used to normalize the rotation ϑ, allowing the expression of the *M–ϑ* relations in non-dimensional form: $M_u/S_u\,B^3 = f\,(\vartheta/\theta_S)$. Thanks to the normalization of ϑ with θ_S, the shape of the moment–rotation curves is almost identical for all cases examined, irrespective of *Fs*. Hence, if we normalize $M_u/S_u\,B^3$ with the moment capacity $M_u/S_u\,B^3$ of each curve, the moment–rotation curves of Figure 6.25 (a) "collapse" in the single non-dimensional curve of Figure 3.25 (b). The latter is simplified further, being approximated by piecewise linear segments. The resulting non-dimensional *M–ϑ* relation encompasses: (a) a quasi-elastic branch, for $\vartheta/\theta_S \leq 1/3$; (b) a plastic branch, for $\vartheta/\theta_S > 10$; and (c) an intermediate nonlinear branch, for $1/3 < \vartheta/\theta_S \leq 10$, consisting of four segments, as illustrated in Figure 3.25 (b).

3.2.4.2 Damping-Rotation Relations

For the rocking-dominated systems considered herein, the damping comprises three different components: (a) radiation damping, (b) hysteretic damping, and (c) damping due to impacts. In the idealized case of elastic soil response (without uplifting or soil inelasticity), radiation is the main

source of damping: waves emanating from the dynamically oscillating foundation disperse to infinity, “absorbing” energy from the rocking system (Gazetas, 1983).

However, when considering strongly inelastic response due to material (soil) and geometric nonlinearities (uplifting), radiation damping is practically negligible compared to hysteretic damping. Under strong seismic shaking, which is the main target of the proposed simplified method, the fundamental period *Tsoil* of the soil layer will be significantly lower than both the predominant period *Tp* of the earthquake and the natural period *Tn* of the rocking system—especially in view of the fact that the latter increases substantially due to uplifting. As a result, the system will respond below its “cutoff” frequency (Gazetas, 1983), and radiation damping will be of the order of 1% to 2%. Damping due to impacts is also considered negligible compared to hysteretic damping, being important only when soil inelasticity is limited.

Based on the above, emphasis is placed on the hysteretic component of rotational damping. The latter is computed on the basis of displacement–controlled cyclic pushover analyses, utilizing the rigorous 3D FE model. The FE analyses are conducted for the previously discussed factors of safety against vertical loading *Fs* = 2, 2.5, 3.3, 5, and 10. The rotational damping coefficient is a function of the effective (secant) rotational stiffness K_R, the hysteretic damping ratio ξ, and a characteristic frequency ω:

$$C_R \approx \frac{2K_R\xi}{\omega} \quad (9)$$

While the effective (secant) stiffness K_R is computed utilizing the previously discussed M–ϑ relations, the hysteretic damping ratio ξ is computed through the M–ϑ loops of the cyclic pushover analyses. For this purpose, the SDOF is subjected to cyclic rotation of increasing amplitude. The hysteretic damping ratio ξ is calculated according to its standard definition:

$$\xi \approx \frac{\Delta E/E}{4\pi} \quad (10)$$

where ΔE is the area of the M–ϑ loops, representing the energy consumed during one cycle of loading, and E is the corresponding elastic energy. As discussed in the sequel, the selection of the characteristic frequency ω is not that straightforward.

The results of the analyses are summarized in Figure 3.26 (a), where the hysteretic damping ratio ξ is plotted as a function of the dimensionless cyclic rotation amplitude ϑ/θ_S and the factor of safety against vertical loading *Fs*. As expected, ξ increases with the decrease of *Fs*, since energy dissipation increases with soil nonlinearity (the area enclosed by the *M*–ϑ loops becomes larger). Exactly for the same reason, ξ is an increasing function of ϑ/θ_S. Exactly the opposite is observed for the normalized effective (secant) rotational stiffness $K_R/K_{R,elastic}$, which (as also expected) increases with *Fs*, while being a decreasing function of ϑ/θ_S (Figure 3.26 (b)): the increase of soil inelasticity leads to a decrease of the secant stiffness. As a result, being the product of K_R and ξ (Eq. 10) the damping coefficient C_R is not that sensitive to ϑ/θ_S (assuming a constant value of ω). As shown in Figure 3.26 (c), the normalized damping coefficient $C_R/K_{R,elastic}\omega^{-1}$ plotted with respect to ϑ/θ_S is a "bell shaped" curve, with its maximum at $\vartheta/\theta_S \approx 1$. Interestingly, if we plot $C_R/K_{R,elastic}\omega^{-1}$ as a function of the absolute value of ϑ (Figure 3.26 (d)), the maximum is observed for roughly 10^{-3} rad, for all cases examined. The value of the maximum $C_R/K_{R,elastic}\omega^{-1}$ increases with the decrease of *Fs*.

As revealed by the derived C_R–ϑ relations, a nonlinear dashpot would ideally be required. Nevertheless, since most commercial FE codes accept a single value of C_R, a simplifying approximation is proposed in order to maintain simplicity. As discussed in the sequel, the numerical prediction using the simplified model compares well with the results of the rigorous 3D FE model, when the maximum value of the normalized C_R–ϑ curve is adopted. Therefore, in terms of a reasonable simplifying assumption, it is recommended to directly use this value to compute the necessary C_R as a function of *Fs* only, as indicated in Figure 3.26 (d)**.**

Following the previous methodology, to the final simple model used in each direction a nonlinear rotational spring and a linear rotational dashpot are added. The stiffness of the rotational spring is described by the Moment-Angle curve shown in Figure 3.27 for both directions and for Fs=6.7.

As far as the rotational dashpot is concerned, its damping coefficient is calculated as described in the previous paragraph. The horizontal and vertical stiffness and damping of the soil-foundation system is considered with the use of the same linear elastic horizontal and vertical springs and dashpots as before.

3.2.4.3 Dynamic Analysis

Both the new simple models and the complete 3D model are tested in both directions under nonlinear time history analysis using the same three real earthquake records. The seismic excitation is imposed at the fixed nodes of the springs and the dashpots that replace the soil-foundation system and the fixed nodes of the horizontal springs and dashpots that represent the stiffness and damping of each bearing. The input seismic excitation is again the acceleration time history at the surface of the soil as resulted from the analysis of the complete model. The results of the analysis and the comparison between the simple model and the complete one in each direction are presented below.

- **Longitudinal direction**

The seismic performance of both the complete model and the simple one is described by the Rotation time histories of the footing, the Relative Displacement time histories at the top of the pier and the Moment-Curvature curves at the base of the pier. The above curves for each earthquake record and for both models are presented in Figures 3.28, 3.29. Structural damage of the piers is expressed in terms of Maximum Drift, Residual Drift and in terms of ductility $\frac{\mu_{demand}}{\mu_{capacity}}$ which are extruded from the above curves. These values for each earthquake record and for both models are shown in Table 3.6. In this case for the 2 of the 3 records that demanded less ductility than the capacity of the system, the maximum deviation observed in terms of $\frac{\mu_{demand}}{\mu_{capacity}}$ is 19%, while the average deviation is 13%. These deviations are practically the same with the previous approach of using the linear elastic springs and dashpots by Gazetas (1983).

- **Transverse direction**

The seismic performance of both the complete model and the simple one in the transverse direction is also described by the Rotation time histories of the footing, the Relative Displacement time histories at the top of the pier and the Moment-Curvature curves at the base of the pier. The above curves for each earthquake record and for both models are presented in Figures 3.30, 3.31. Structural damage of the piers is expressed in terms of Maximum Drift, Residual Drift and in terms of ductility $\frac{\mu_{demand}}{\mu_{capacity}}$ which are extruded from the above curves. These values for each earthquake record and for both models are shown in Table 3.7. In this case for the 2 of the 3 records that demanded less ductility than the capacity of the system, the maximum deviation observed in terms of $\frac{\mu_{demand}}{\mu_{capacity}}$ is 9%, while the average deviation is 9%. These deviations are practically the same with the previous approach of using the linear elastic springs and dashpots by Gazetas (1983).

Chapter 3

Figures

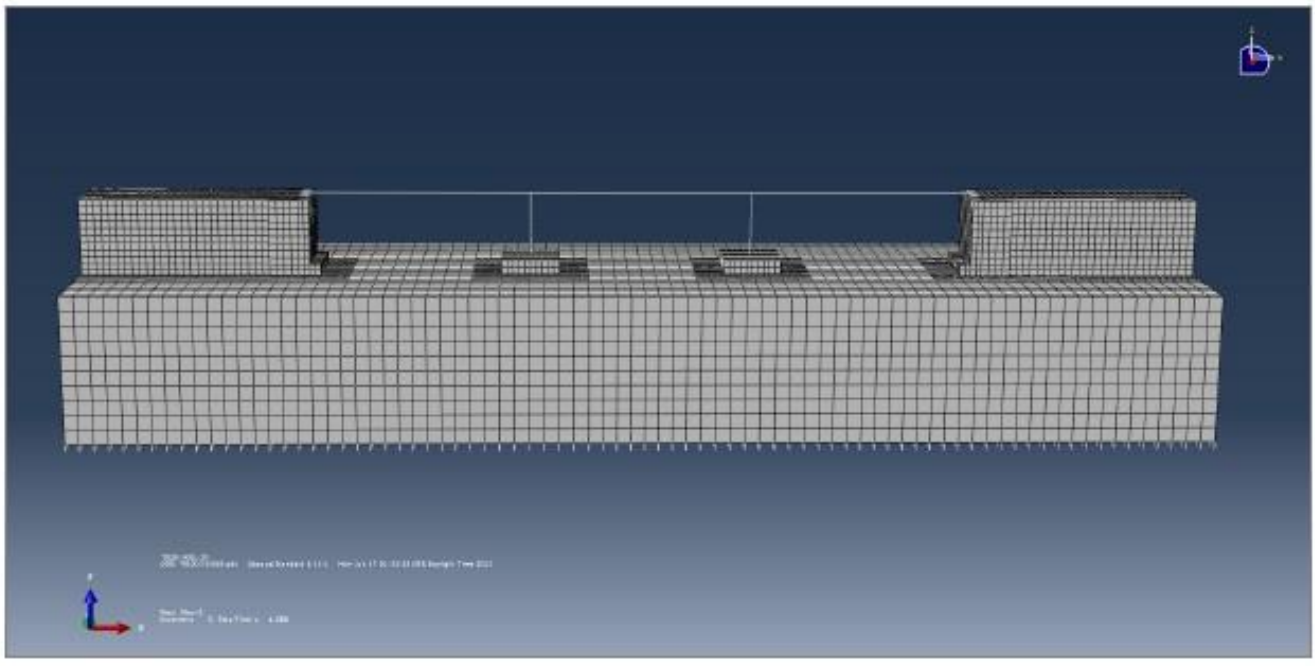

Figure 3.1 Complete 3D Bridge-Soil Model

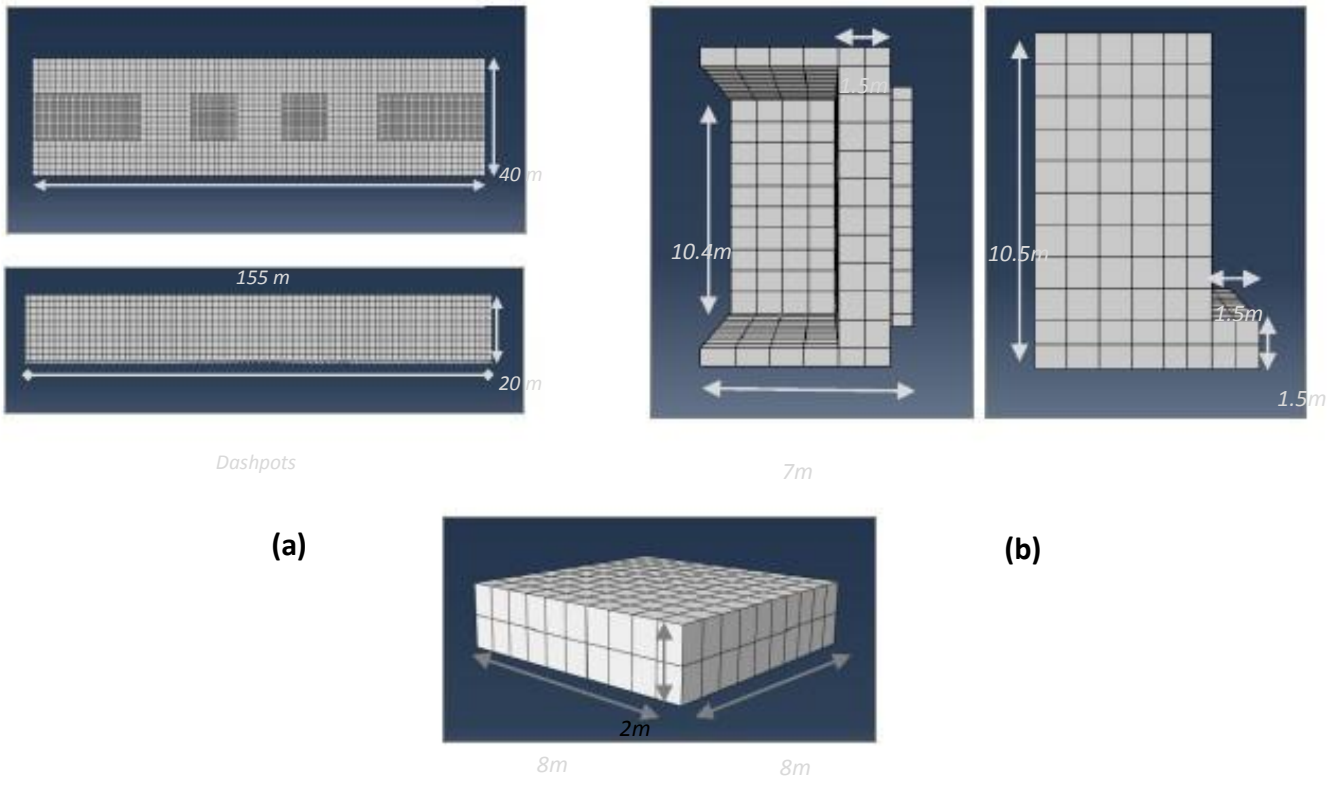

Figure 3.2 . **(a)** Soil Model , **(b)** Model of Retaining Walls, **(c)** Model of Footings

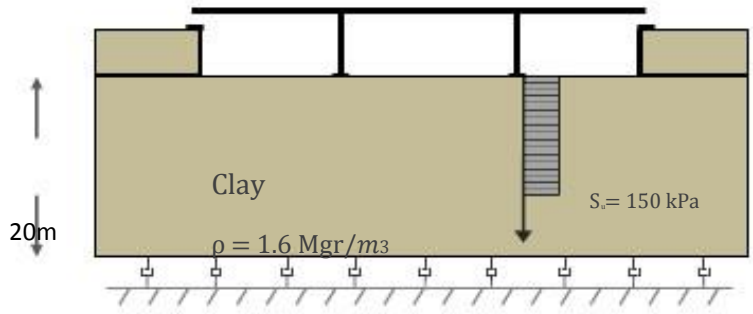

Figure 3.3 Soil Properties

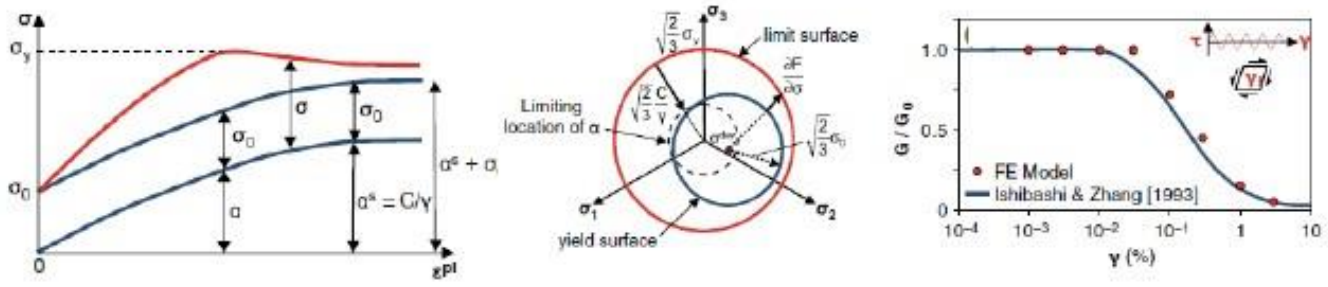

(a) (b) (c)

Figure 3.4 (a),(b) Simplified 1D and 3D representation of the hardening, **(c)** Calibration of kinematic hardening model for soil (stiff clay, Su =150kPa) against published G–γ (PI=30, σv =100kPa) curves (Ishibashi and Zhang 1993)

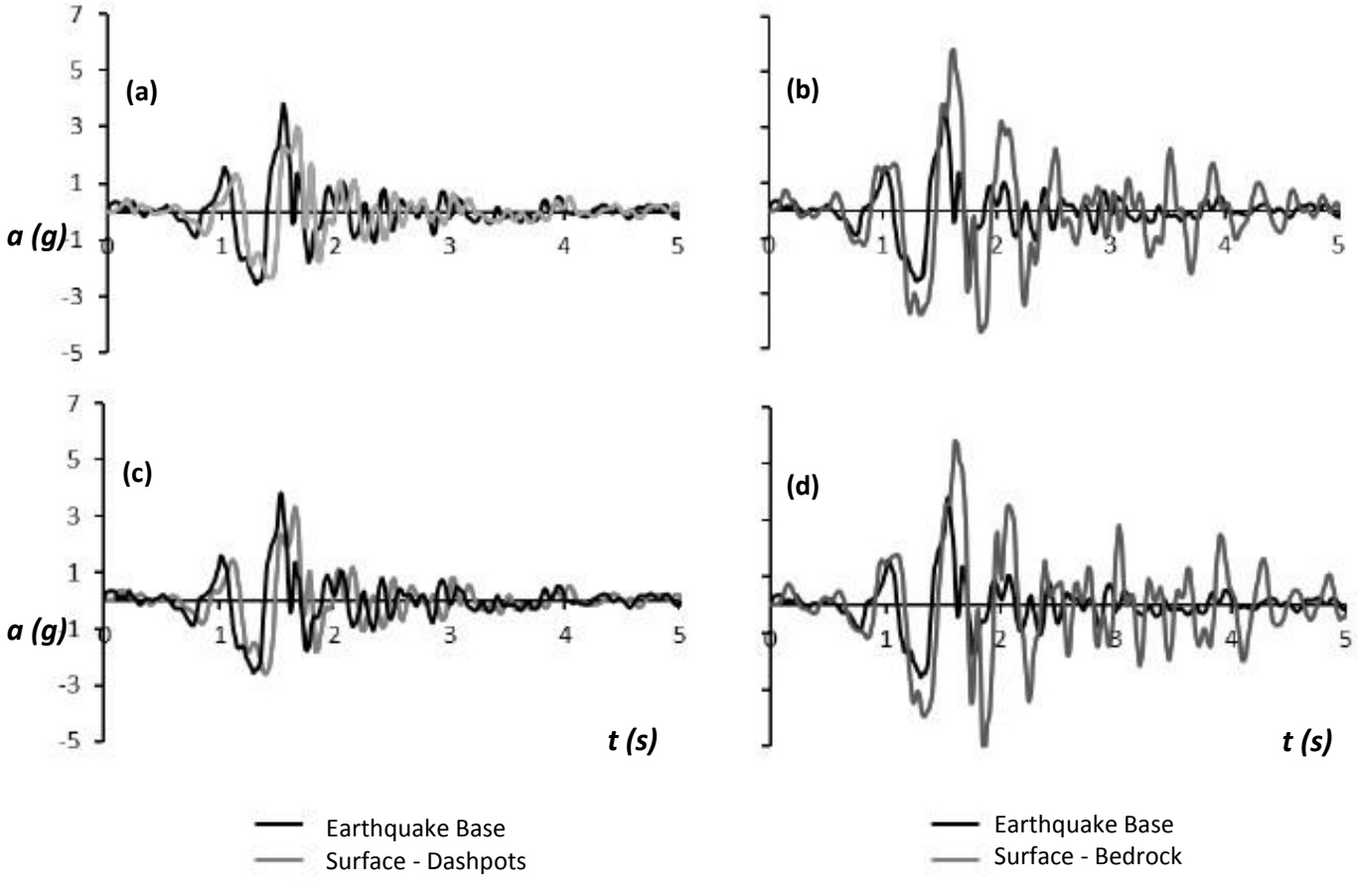

Figure 3.5 Soil amplification with **(a),(c)** and without **(b),(d)** Dashpots at the bottom of the model for Aegio record in longitudinal and transvers direction

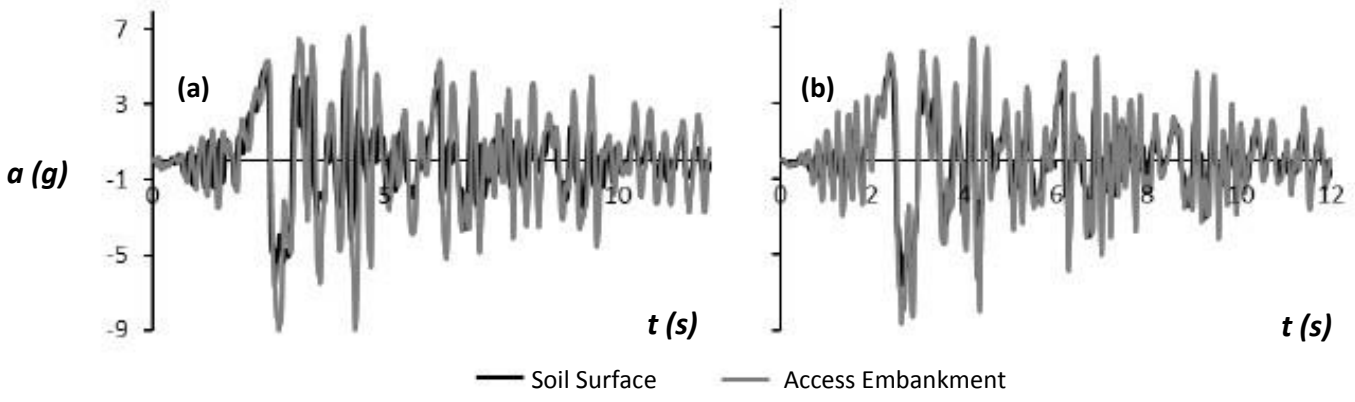

Figure 3.6 Soil amplification for Rinaldi_228 record in **(a)** Longitudinal and **(b)** Transverse direction on access embankment

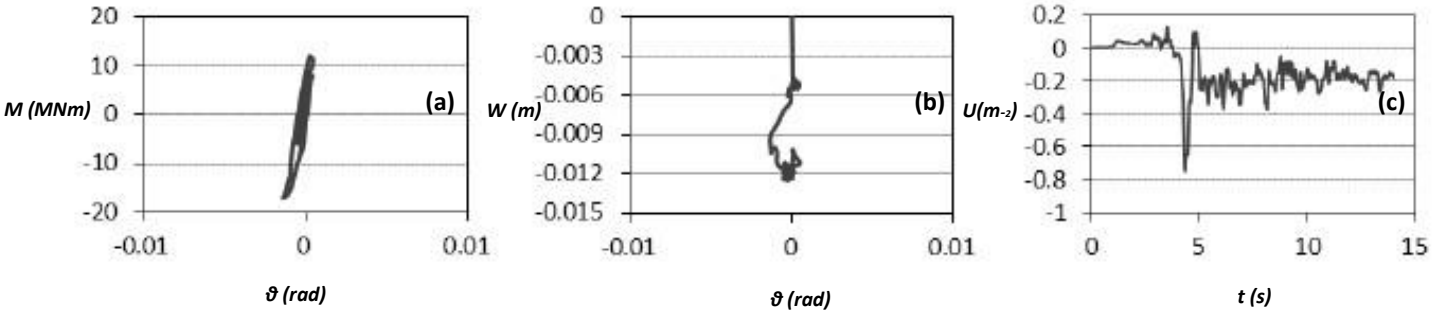

Figure 3.7 (a) Moment-Angle, **(b)** Settlement – Angle and **(c)** Horizontal drift curve of surface foundation for Rinaldi_228 record in Longitudinal direction

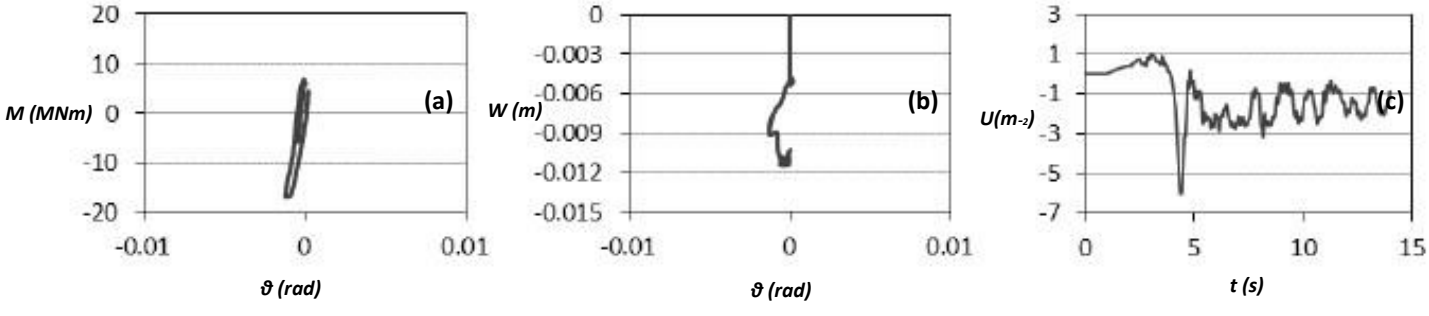

Figure 3.8 (a) Moment-Angle, **(b)** Settlement – Angle and **(c)** Horizontal drift curve of surface foundation for Rinaldi_228 record in Transverse direction

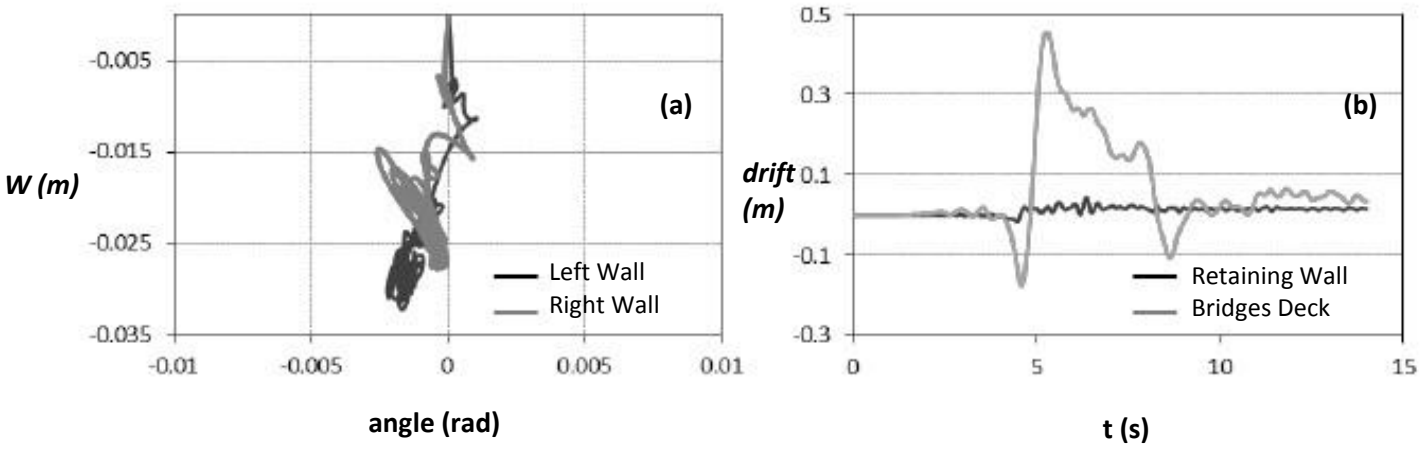

Figure 3.9 (a) Settlement-angle for both retaining walls and **(b)** drift of right retaining wall and displacement of deck for Rinaldi_228 record in Longitudinal direction

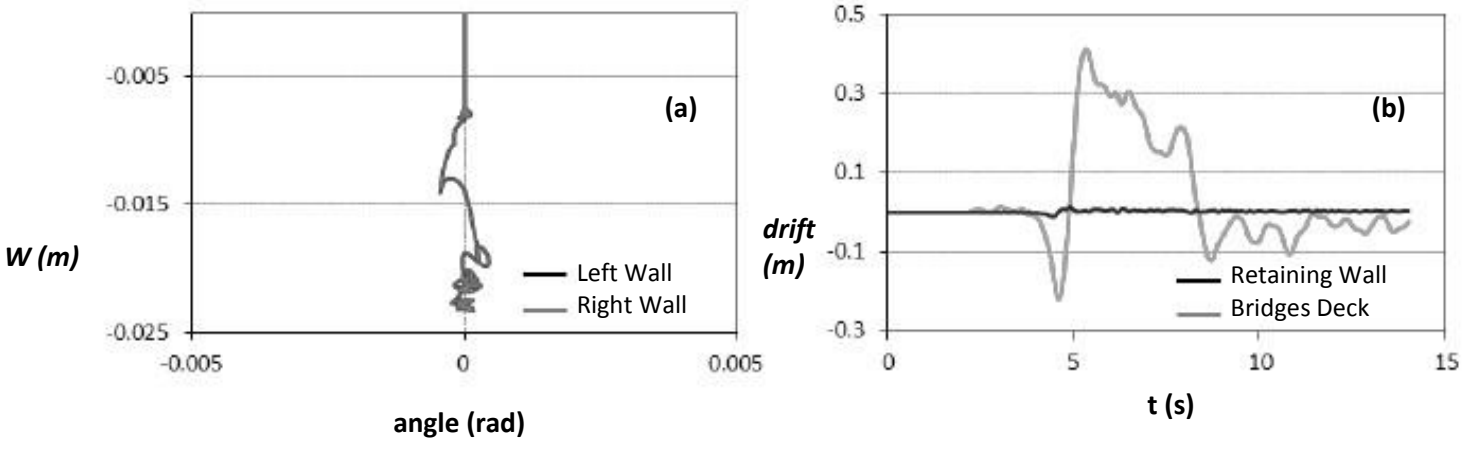

Figure 3.10 (a) Settlement-angle for both retaining walls and **(b)** drift of right retaining wall and displacement of deck for Rinaldi_228 record in Transverse direction

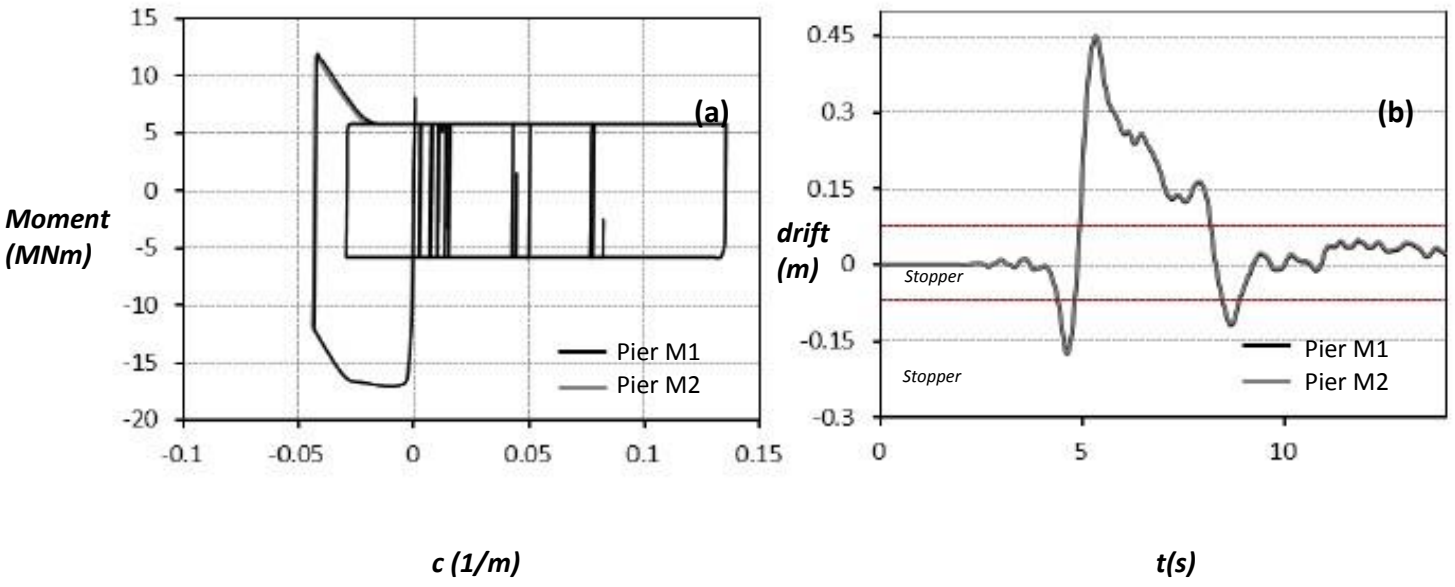

Figure 3.11 (a) Moment-Curvature and **(b)** drift time history for both piers for Rinaldi_228 record in Longitudinal direction

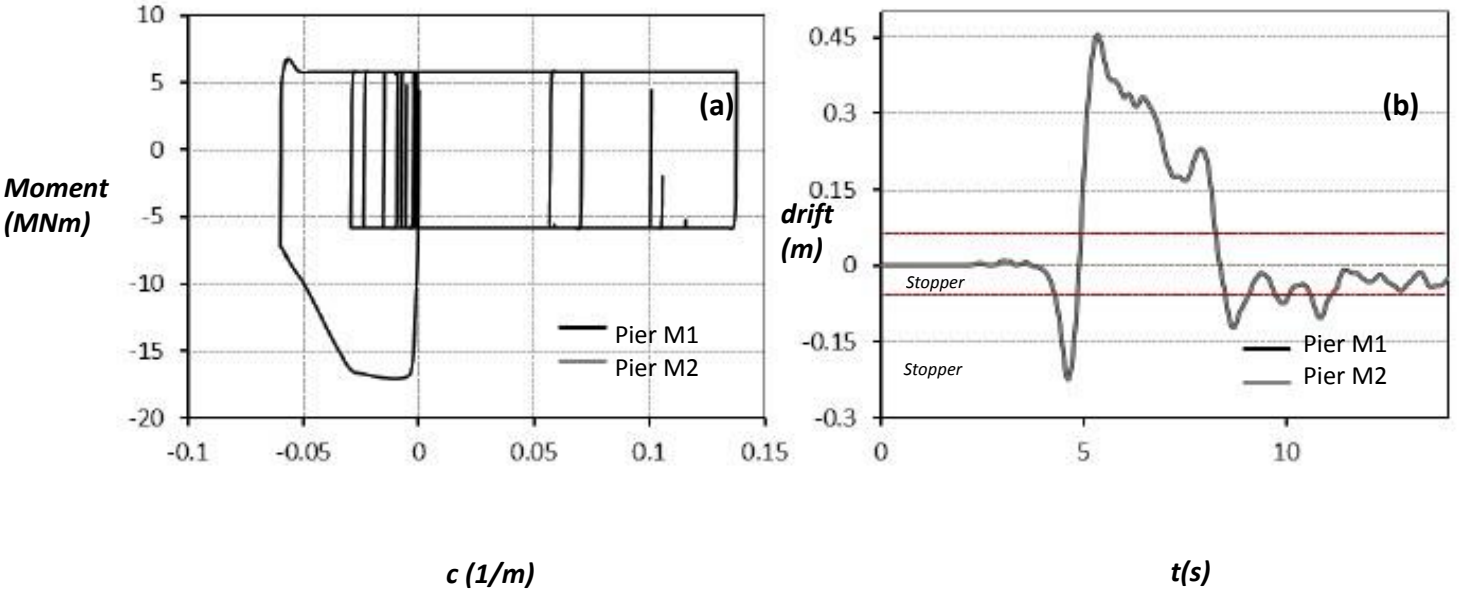

Figure 3.12 (a) Moment-Curvature and **(b)** drift time history for both piers for Rinaldi_228 record in Transverse direction

Rinaldi_228	Longitudinal			Transverse		
	Max Drift	Res Drift	μd/μc	Max Drift	Res Drift	μd/μc
Pier M1	0.45	0.02	5.1	0.46	0.03	5.2
Pier M2	0.45	0.02	5.1	0.46	0.03	5.2

Table 3.1 Seismic Performance of the two piers on Rinaldi_228 record

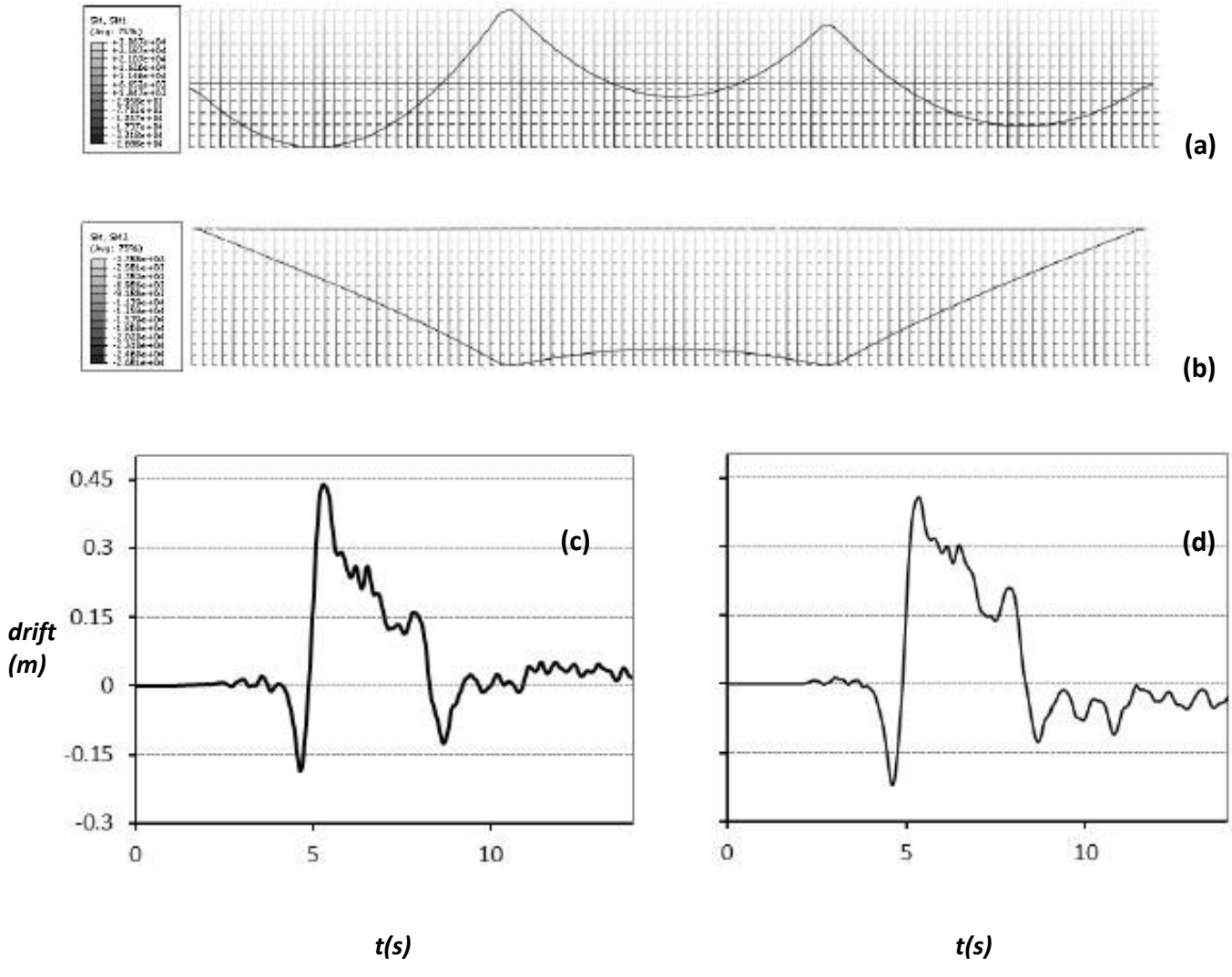

Figure 3.13 Moment curve of deck in **(a)** longitudinal and **(b)** transverse direction and drift time history of bearing in **(c)** longitudinal and **(d)** transverse direction

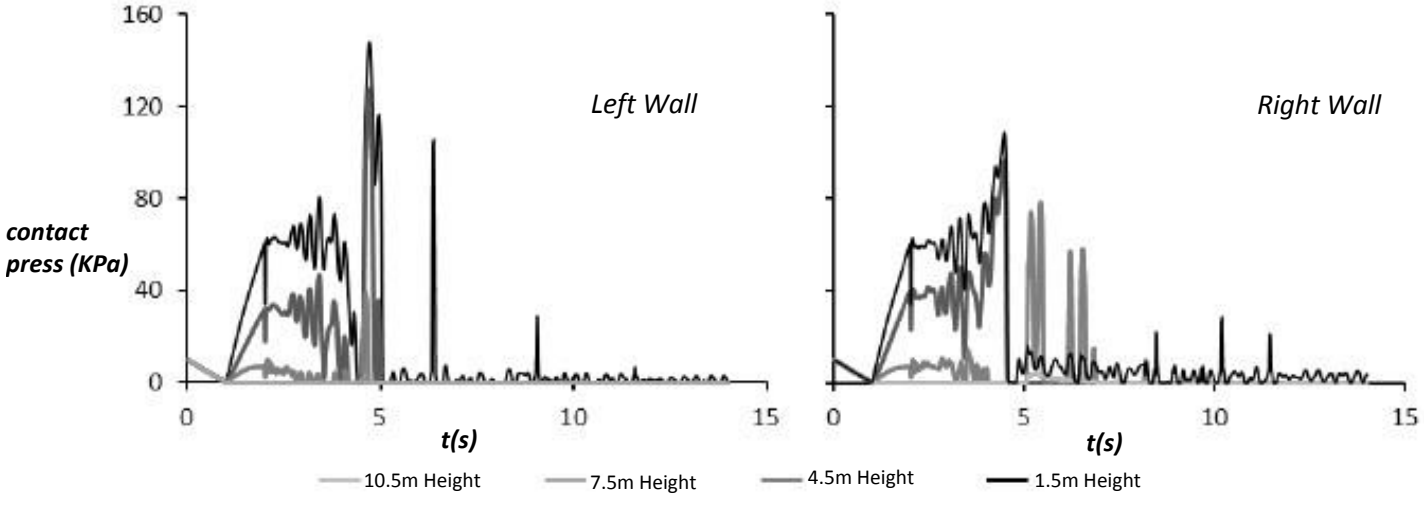

Figure 3.14 Contact Press in both retaining walls in Longitudinal direction for Rinaldi_228 record

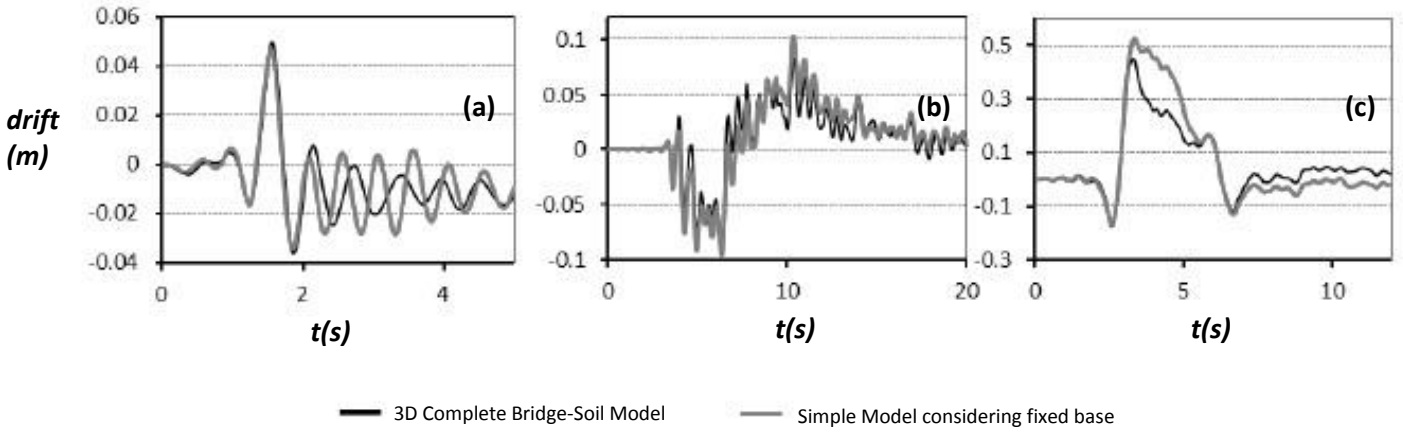

Figure 3.15 Drift time histories of the two models for **(a)** Aegio, **(b)** Lefkada_2003 and **(c)** Rinaldi_228 records in Longitudinal direction

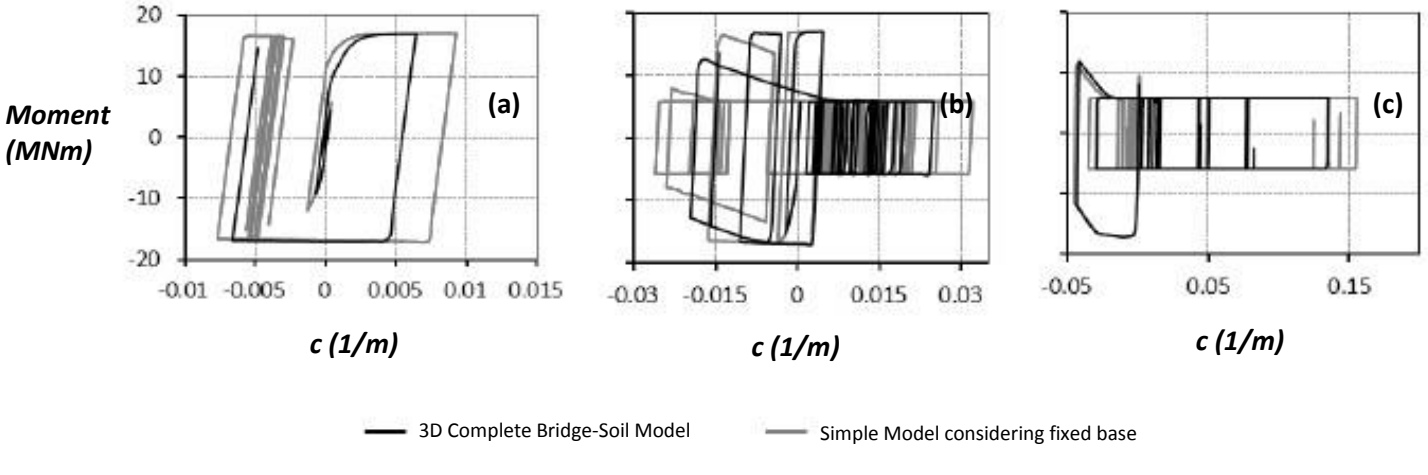

Figure 3.16 Moment-Curvature curves of the two models for **(a)** Aegio, **(b)** Lefkada_2003 and **(c)** Rinaldi_228 records in Longitudinal direction

	3D Complete Bridge-Soil Model				*Simple Model Fixed Base*			
	max Drift (m)	Drift res (m)	μ demand	μ d / μ c	max Drift (m)	Drift res (m)	μ demand	μ d / μ c
AEGIO	0.05	0.01	2.85	0.25	0.05	0.01	4.00	0.35
LEFKADA_2003	0.09	0.00	10.70	0.94	0.10	0.00	13.82	1.21
RINALDI_228	0.45	0.02	58.38	5.12	0.53	0.02	67.06	5.88

Deviations					
max Drift (m)	maxDrift ratio (%)	Drift res (m)	Drift res ratio (%)	μ demand	μ d / μ c
0.00	0.00	0.00	0.00	1.15	0.10
0.01	0.11	0.00	0.01	3.12	0.27
0.08	0.91	0.00	0.02	8.68	0.76

Table 3.2 Seismic Performance and deviations observed between the two Models in Longitudinal direction

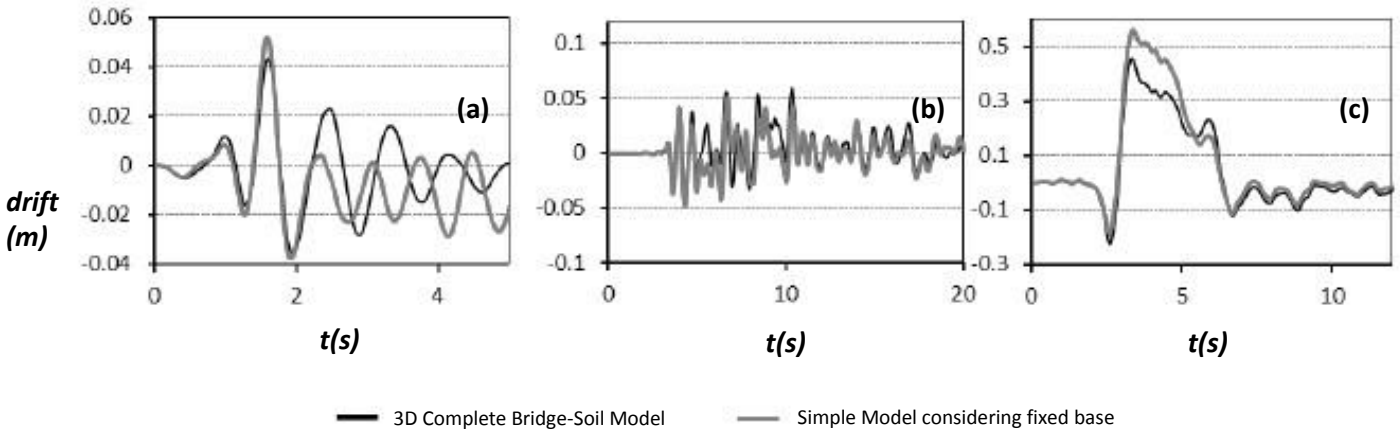

Figure 3.17 Drift time histories of the two models for **(a)** Aegio, **(b)** Lefkada_2003 and **(c)** Rinaldi_228 records in Transverse direction

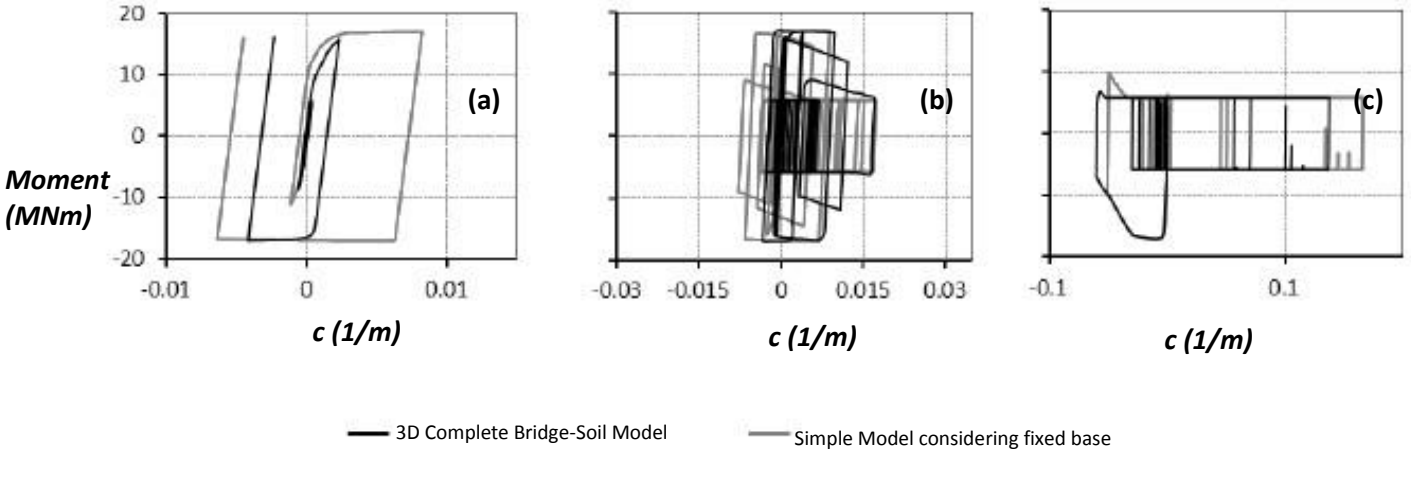

Figure 3.18 Moment-Curvature curves of the two models for **(a)** Aegio, **(b)** Lefkada_2003 and **(c)** Rinaldi_228 records in Transverse direction

	3D Complete Bridge-Soil Model				*Simple Model Fixed Base*			
	max Drift (m)	Drift res (m)	μ demand	μ d / μ c	max Drift (m)	Drift res (m)	μ demand	μ d / μ c
AEGIO	0.04	0.00	1.81	0.16	0.05	0.02	3.55	0.31
LEFKADA_2003	0.06	0.00	7.35	0.64	0.05	0.00	7.52	0.66
RINALDI_228	0.46	0.03	59.42	5.21	0.56	0.01	71.70	6.29

Deviations					
max Drift (m)	maxDrift ratio (%)	Drift res (m)	Drift res ratio (%)	μ demand	μ d / μ c
0.01	0.10	0.02	0.18	1.74	0.15
0.01	0.09	0.00	0.02	0.17	0.02
0.10	1.14	0.01	0.13	12.28	1.08

Table 3.3 Seismic Performance and deviations observed between the two Models in Transverse direction

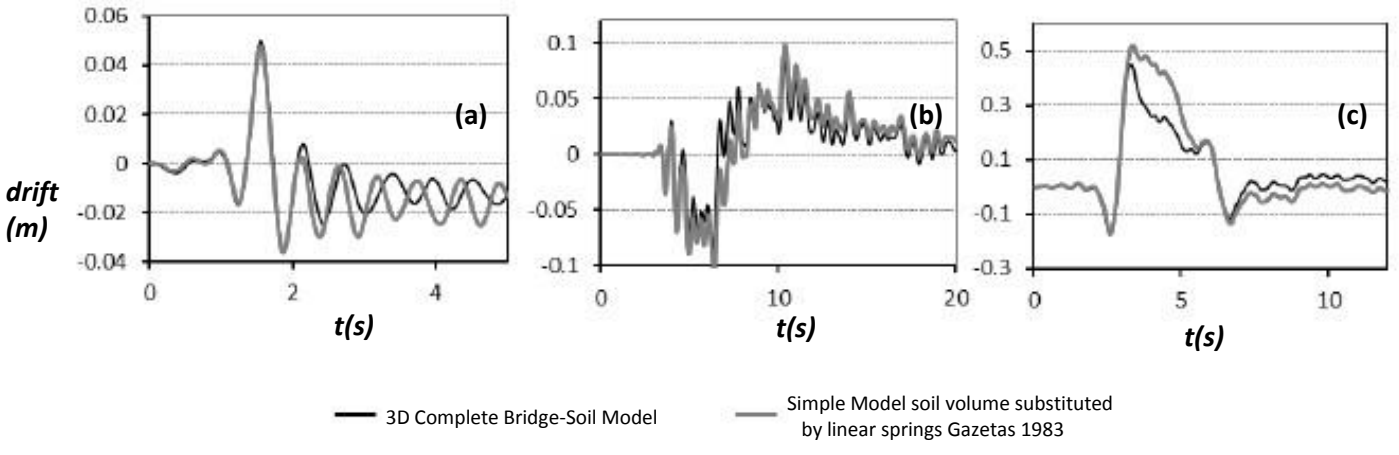

Figure 3.19 Drift time histories of the two models for **(a)** Aegio, **(b)** Lefkada_2003 and **(c)** Rinaldi_228 records in Longitudinal direction

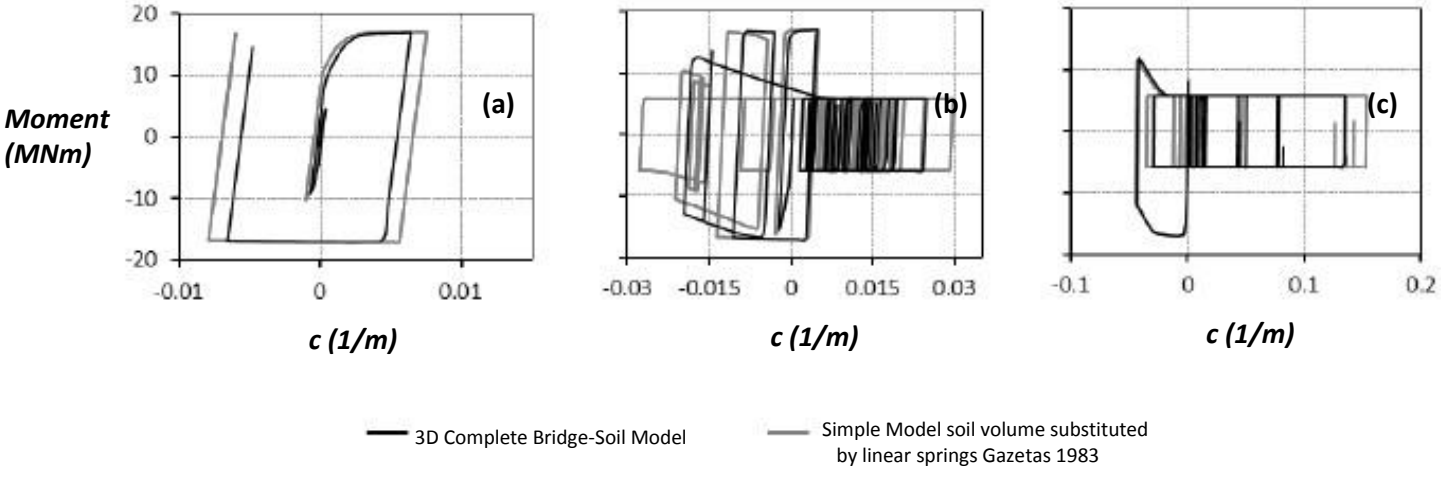

Figure 3.20 Moment-Curvature curves of the two models for **(a)** Aegio, **(b)** Lefkada_2003 and **(c)** Rinaldi_228 records in Longitudinal direction

	3D Complete Bridge-Soil Model				*Simple Model (linear springs Gazetas 1983)*			
	max Drift (m)	Drift res (m)	μ demand	μ d / μ c	max Drift (m)	Drift res (m)	μ demand	μ d / μ c
AEGIO	0.05	0.01	2.85	0.25	0.05	0.01	3.43	0.30
LEFKADA_2003	0.09	0.00	10.70	0.94	0.11	0.01	12.82	1.12
RINALDI_228	0.45	0.02	58.38	5.12	0.52	0.01	66.22	5.81

Deviations					
max Drift (m)	maxDrift ratio (%)	Drift res (m)	Drift res ratio (%)	μ demand	μ d / μ c
0.00	0.00	0.00	0.00	0.58	0.05
0.02	0.23	0.01	0.09	2.12	0.18
0.07	0.80	0.01	0.09	7.84	0.69

Table 3.4 Seismic Performance and deviations observed between the two Models in Longitudinal direction

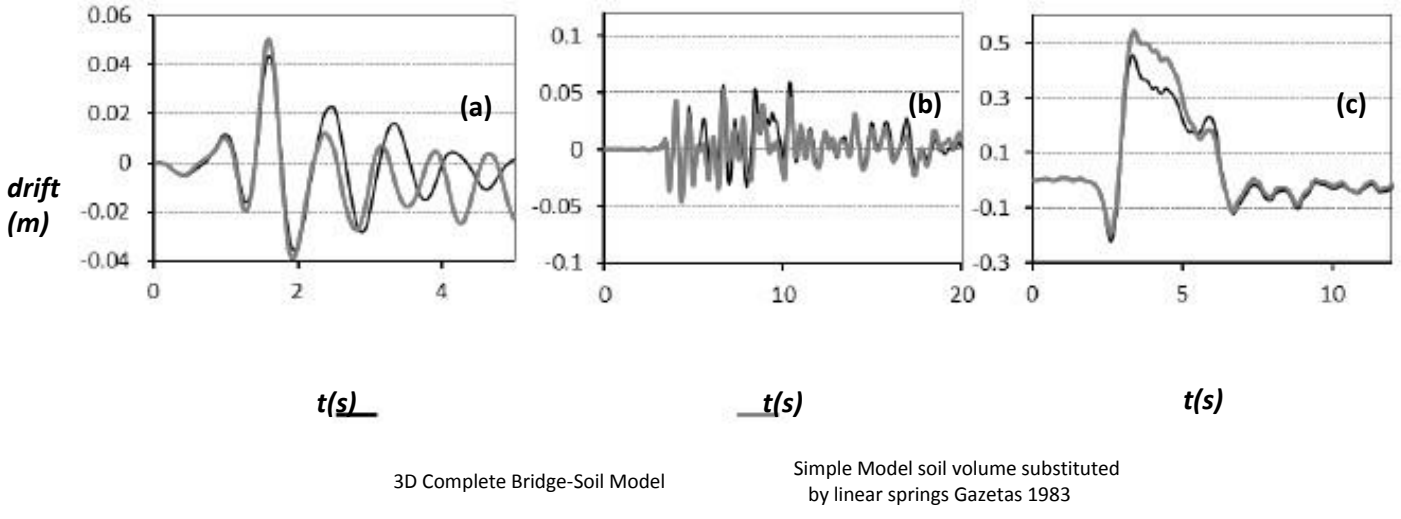

Figure 3.21 Drift time histories of the two models for **(a)** Aegio, **(b)** Lefkada_2003 and **(c)** Rinaldi_228 records in Transverse direction

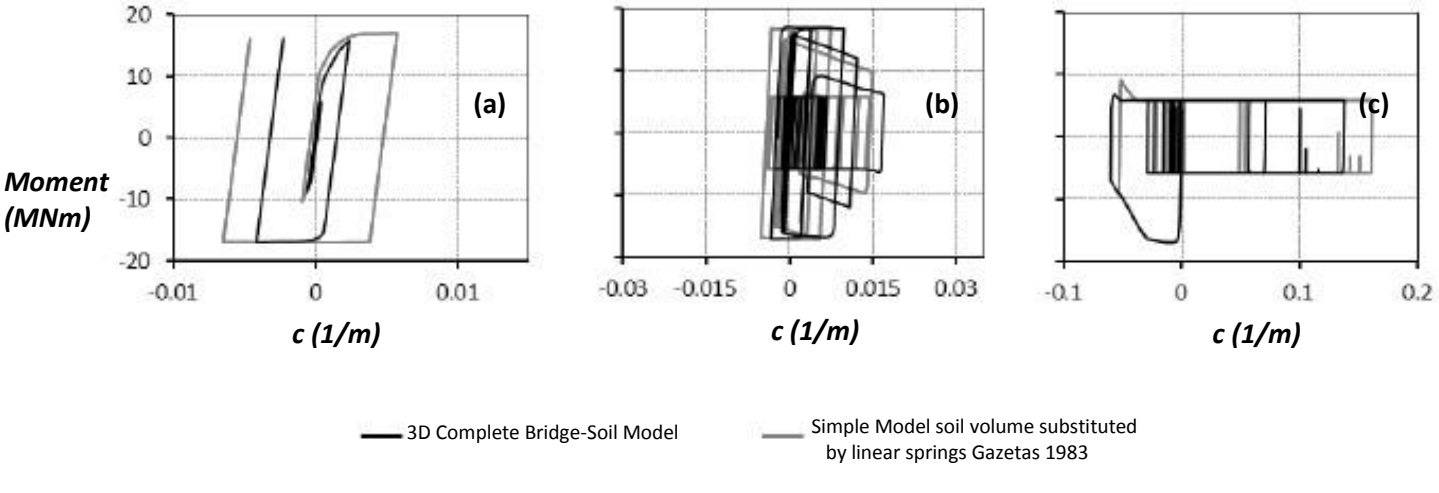

Figure 3.22 Moment-Curvature curves of the two models for **(a)** Aegio, **(b)** Lefkada_2003 and **(c)** Rinaldi_228 records in Transverse direction

	3D Complete Bridge-Soil Model				*Simple Model (linear springs Gazetas 1983)*			
	max Drift (m)	Drift res (m)	μ demand	μ d / μ c	max Drift (m)	Drift res (m)	μ demand	μ d / μ c
AEGIO	0.04	0.00	1.81	0.16	0.05	0.02	2.81	0.25
LEFKADA_2003	0.06	0.00	7.35	0.64	0.05	0.01	6.46	0.57
RINALDI_228	0.46	0.03	59.42	5.21	0.54	0.02	69.46	6.09

Deviations					
max Drift (m)	maxDrift ratio (%)	Drift res (m)	Drift res ratio (%)	μ demand	μ d / μ c
0.01	0.08	0.02	0.25	1.00	0.09
0.01	0.07	0.01	0.08	0.89	0.07
0.08	0.93	0.01	0.09	10.04	0.88

Table 3.5 Seismic Performance and deviations observed between the two Models in Transverse direction

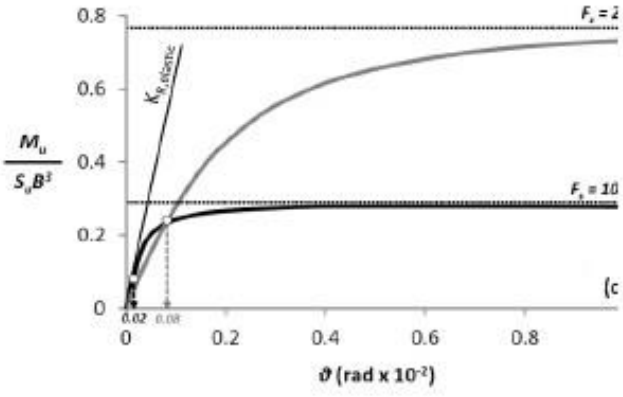

Figure 3.23 Square shallow footing subjected to monotonic pushover loading [Anastasopoulos, Kontoroupi 2013]

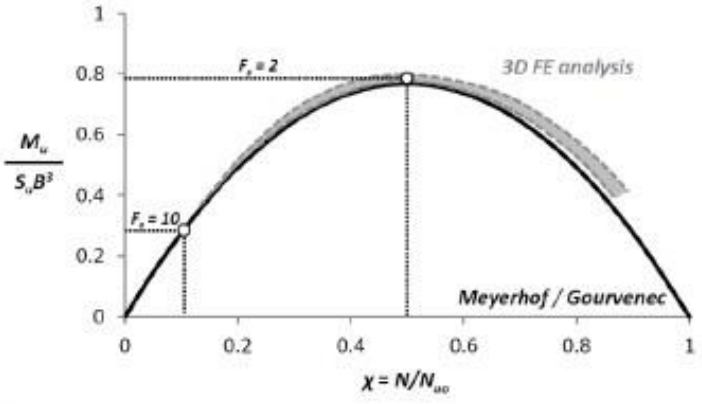

Figure 3.24 Comparison of FE analysis results [Anastasopoulos, Kontoroupi 2013] with published failure envelopes [Meyerhof 1952 ; Gouvernec 2007]

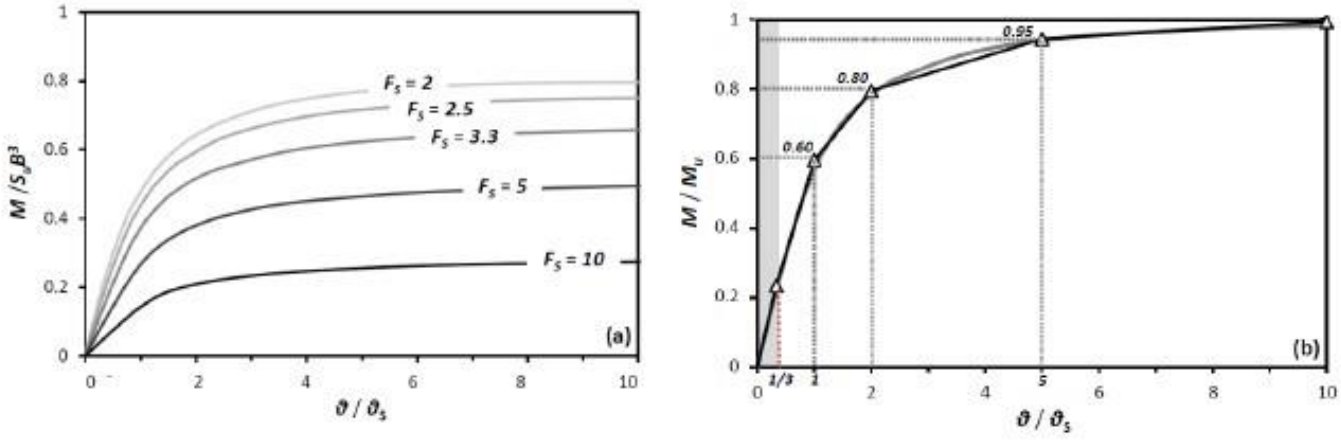

Figure 3.25 (a) Normalized moment-rotation response for different FS and **(b)** non-dimensional unique moment-rotation (M-θ) relation and simplified piecewise approximation [Anastasopoulos, Kontoroupi 2013]

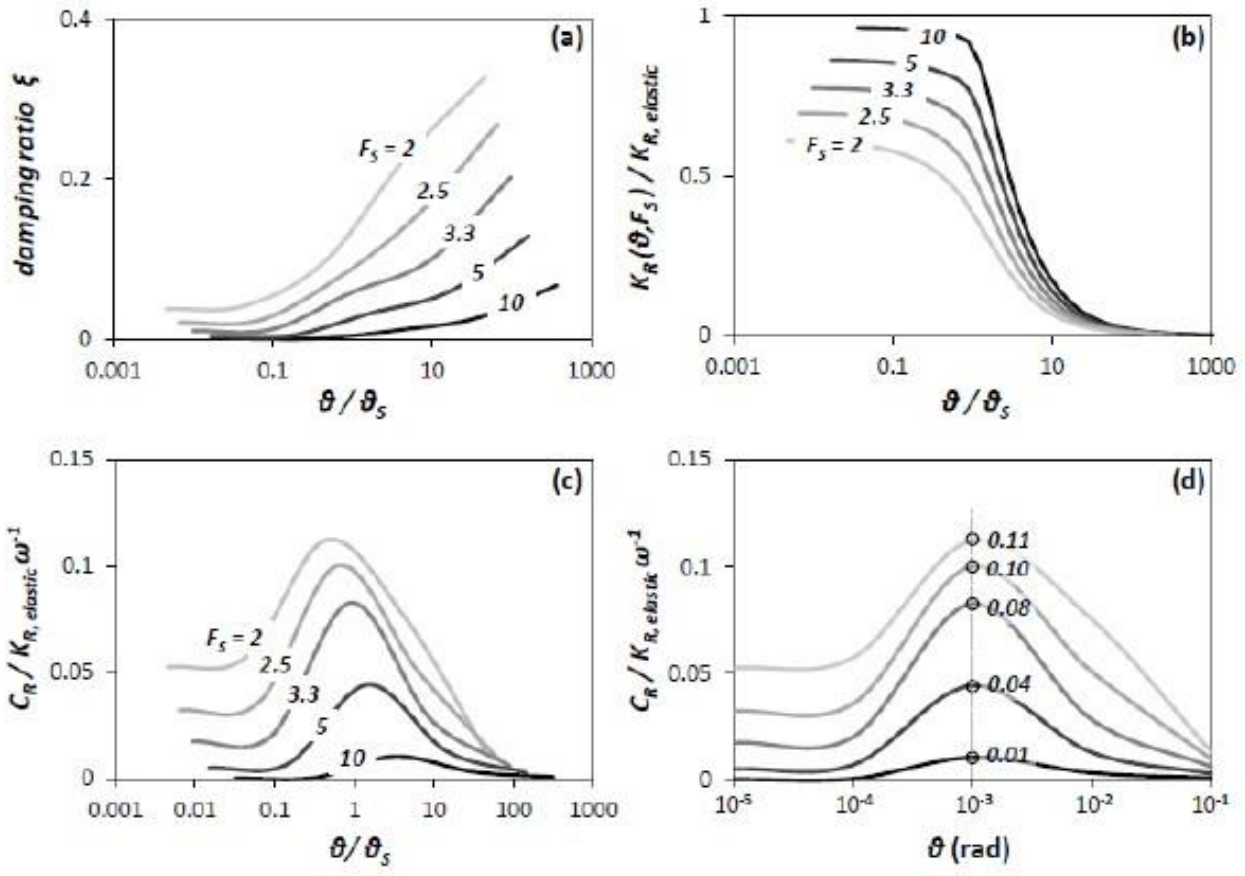

Figure 3.26 (a) Damping ration ξ **(b)** normalized rotational stiffness **(c), (d)** dimensionless damping coefficient with respect to the dimensionless rotation θ/θs and FS and θ and FS [Anastasopoulos, Kontoroupi 2013]

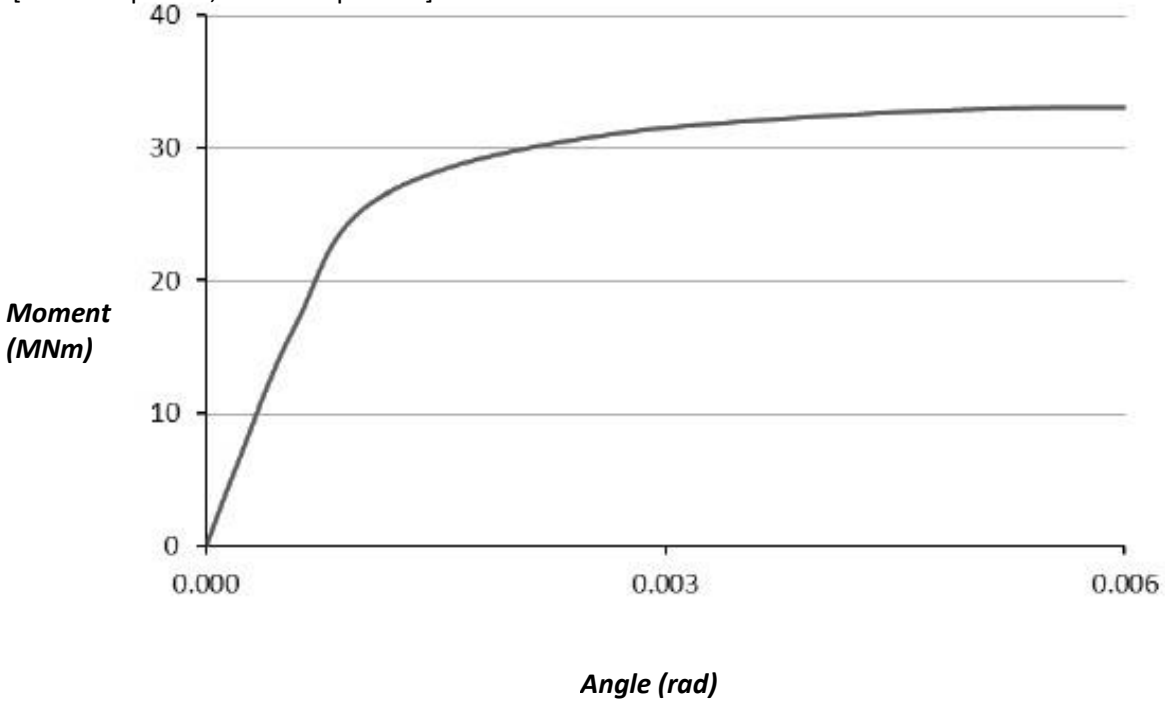

Figure 6.27 Moment-angle curve of the nonlinear rotational spring

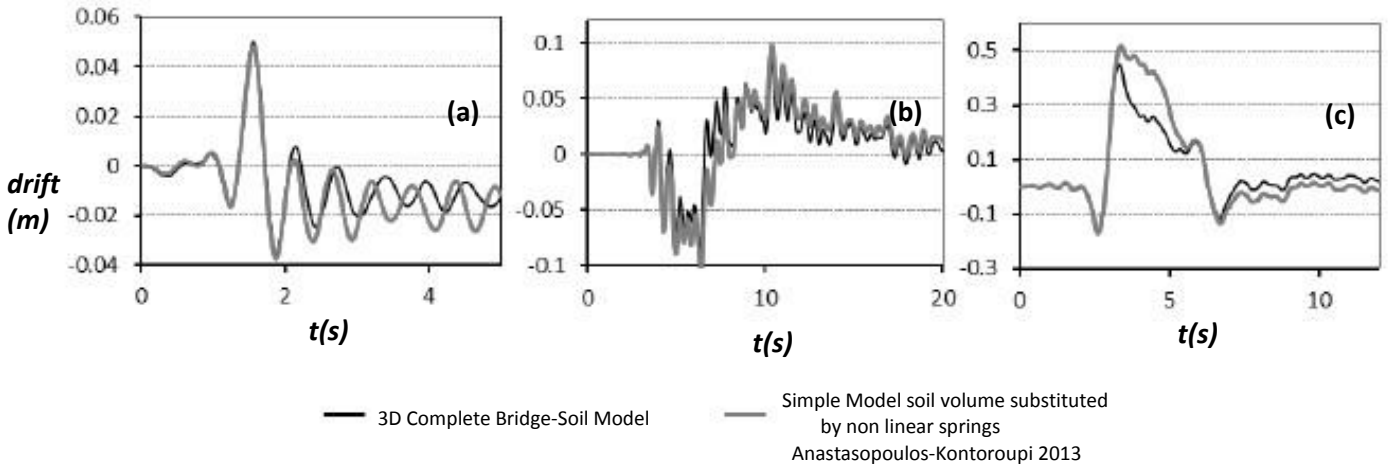

Figure 3.28 Drift time histories of the two models for **(a)** Aegio, **(b)** Lefkada_2003 and **(c)** Rinaldi_228 records in Longitudinal direction

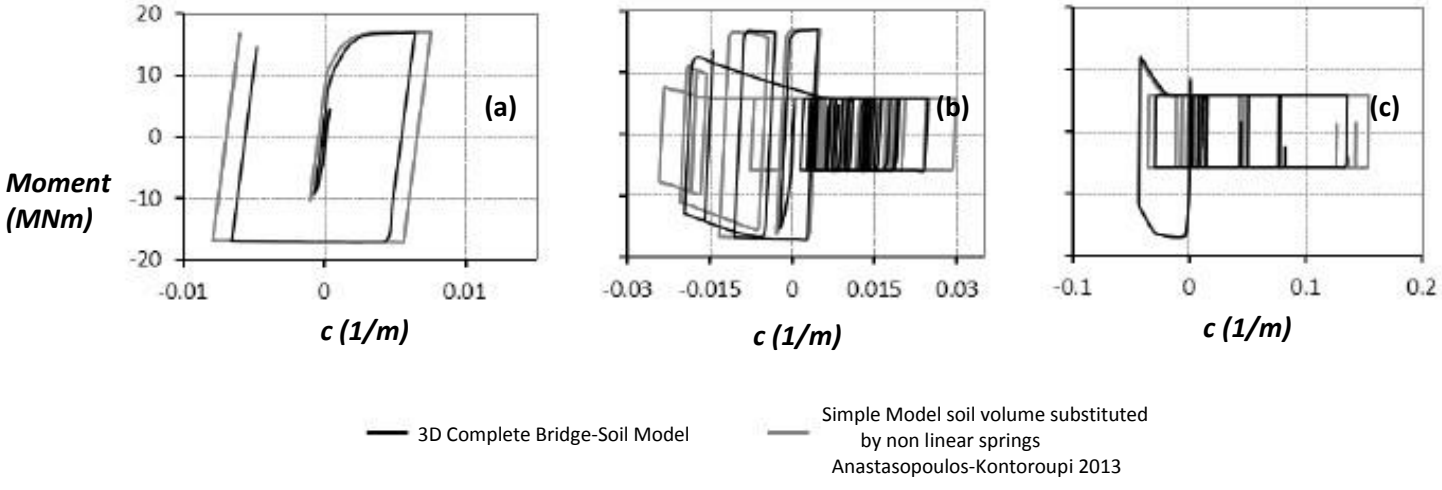

Figure 3.29 Moment-Curvature curves of the two models for **(a)** Aegio, **(b)** Lefkada_2003 and **(c)** Rinaldi_228 records in Longitudinal direction

	3D Complete Bridge-Soil Model				*Simple Model (non linear springs Anastasopoulos)*			
	max Drift (m)	Drift res (m)	μ demand	μ d / μ c	max Drift (m)	Drift res (m)	μ demand	μ d / μ c
AEGIO	0.05	0.01	2.85	0.25	0.05	0.01	3.51	0.31
LEFKADA_2003	0.09	0.00	10.70	0.94	0.10	0.01	12.90	1.13
RINALDI_228	0.45	0.02	58.38	5.12	0.52	0.01	66.23	5.81

Deviations					
max Drift (m)	maxDrift ratio (%)	Drift res (m)	Drift res ratio (%)	μ demand	μ d / μ c
0.00	0.00	0.00	0.00	0.66	0.06
0.01	0.11	0.01	0.09	2.20	0.19
0.07	0.80	0.01	0.10	7.85	0.69

Table 3.6 Seismic Performance and deviations observed between the two Models in Longitudinal direction

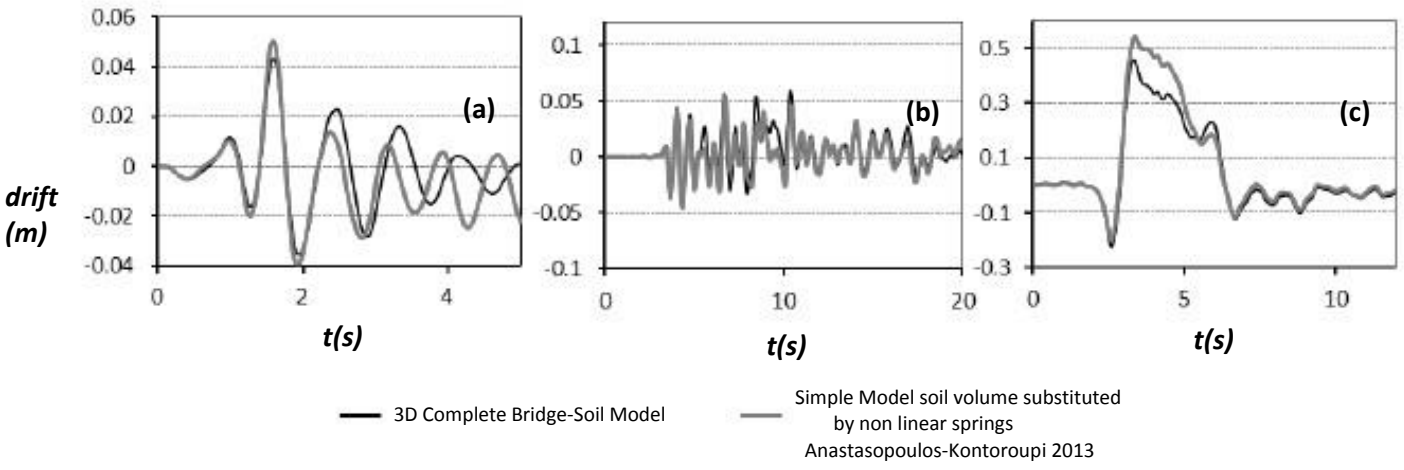

Figure 3.30 Drift time histories of the two models for **(a)** Aegio, **(b)** Lefkada_2003 and **(c)** Rinaldi_228 records in Transverse direction

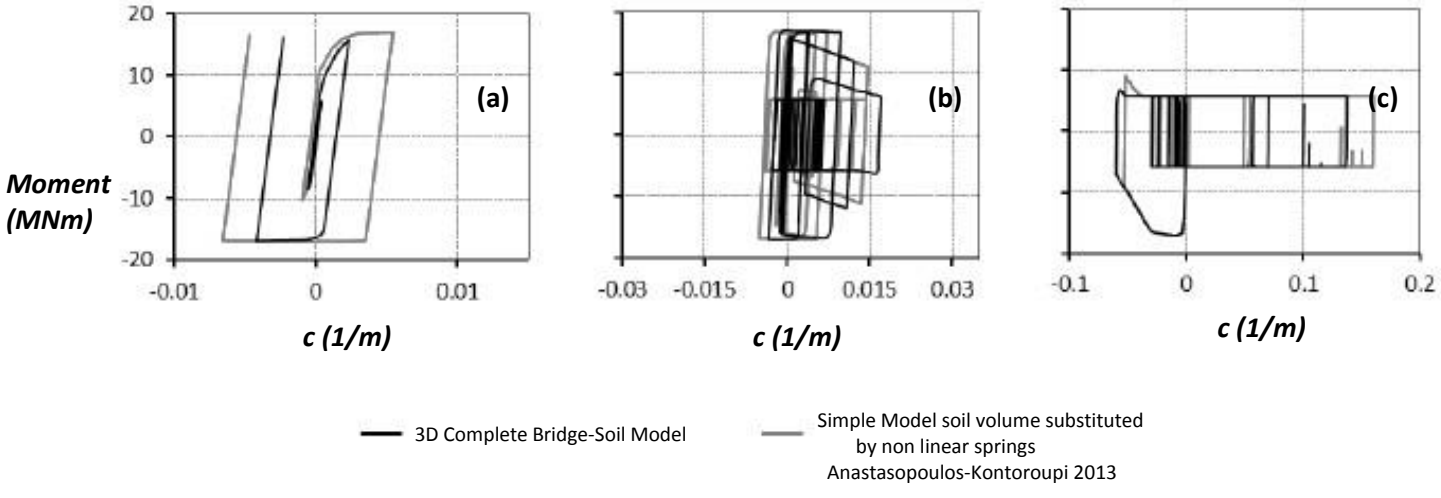

Figure 3.31 Moment-Curvature curves of the two models for **(a)** Aegio, **(b)** Lefkada_2003 and **(c)** Rinaldi_228 records in Transverse direction

	3D Complete Bridge-Soil Model				*Simple Model (non linear springs Anastasopoulos)*			
	max Drift (m)	Drift res (m)	μ demand	μ d / μ c	max Drift (m)	Drift res (m)	μ demand	μ d / μ c
AEGIO	0.04	0.00	1.81	0.16	0.05	0.02	2.84	0.25
LEFKADA_2003	0.06	0.00	7.35	0.64	0.06	0.01	6.35	0.56
RINALDI_228	0.46	0.03	59.42	5.21	0.54	0.02	69.25	6.07

Deviations					
max Drift (m)	maxDrift ratio (%)	Drift res (m)	Drift res ratio (%)	μ demand	μ d / μ c
0.01	0.08	0.02	0.24	1.03	0.09
0.00	0.05	0.01	0.09	1.00	0.08
0.08	0.91	0.01	0.09	9.83	0.86

Table 3.7 Seismic Performance and deviations observed between the two Models in Transverse direction

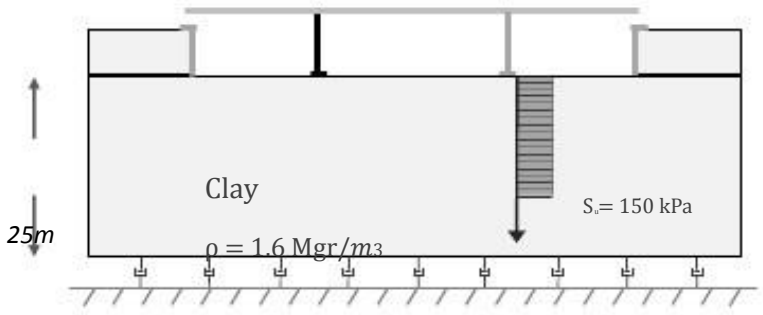

3D Complete Bridge-Soil Model

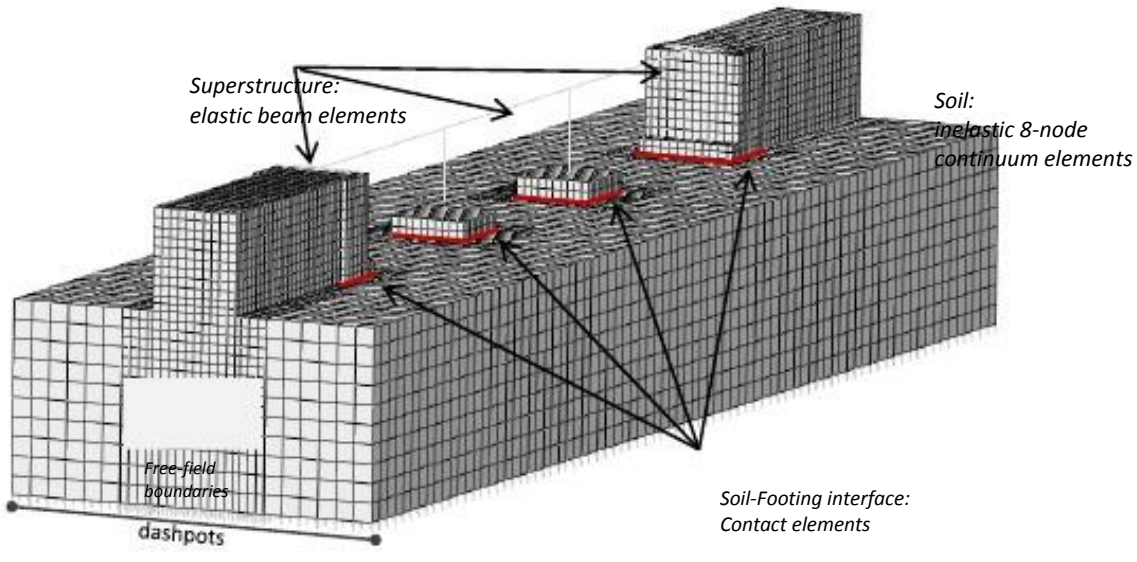

Figure 3.33 Rigorous 3D finite element model comprising the entire soil–foundation–structure system, taking account of material (soil) and geometric nonlinearities (uplifting and P–δ effects).

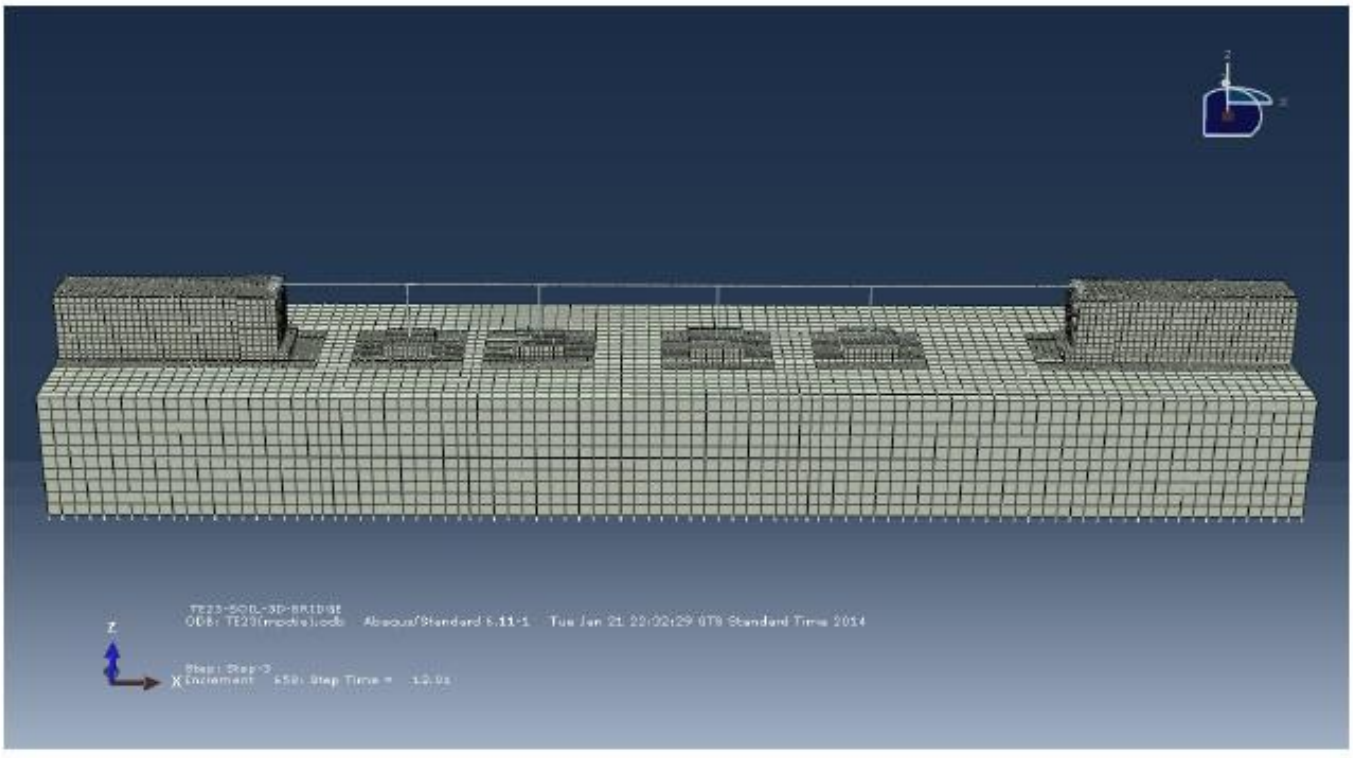

Figure 3.34 Complete 3D Bridge-Soil Model

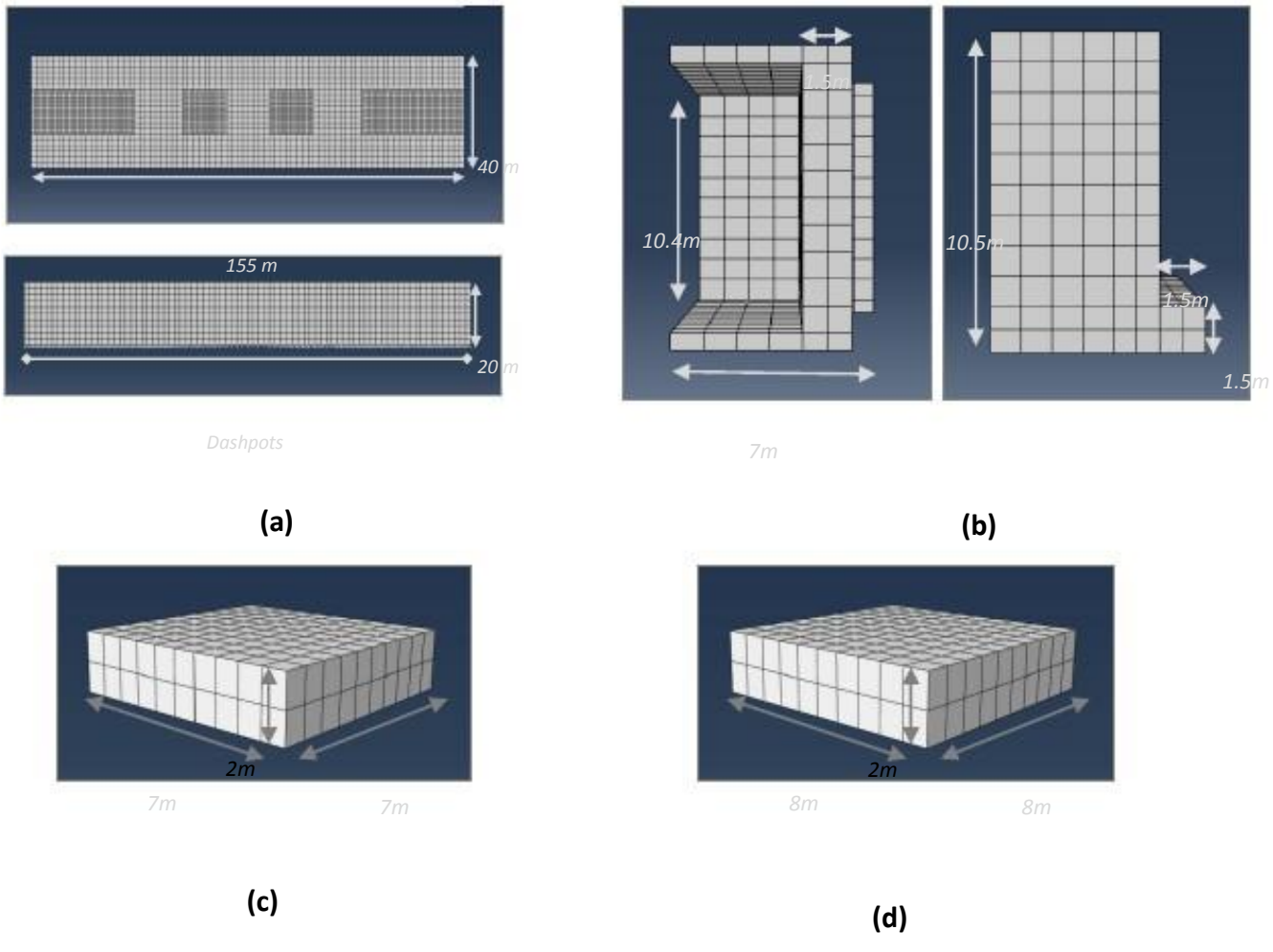

Figure 3.35 . **(a)** Soil Model , **(b)** Model of Retaining Walls, **(c)** Model of Footings 1,2 **(d)** Model of Footings 3,4

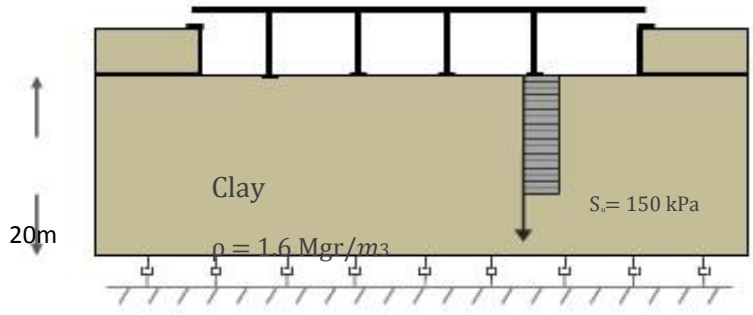

Figure 6.3 Soil Properties

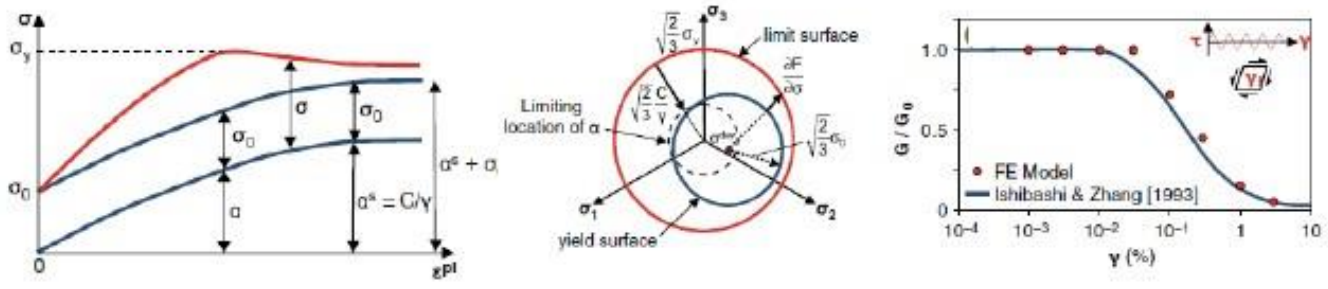

(a) (b) (c)

Figure 3.36 (a),(b) Simplified 1D and 3D representation of the hardening, **(c)** Calibration of kinematic hardening model for soil (stiff clay, Su =150kPa) against published G–γ (PI=30, σv =100kPa) curves (Ishibashi and Zhang 1993)

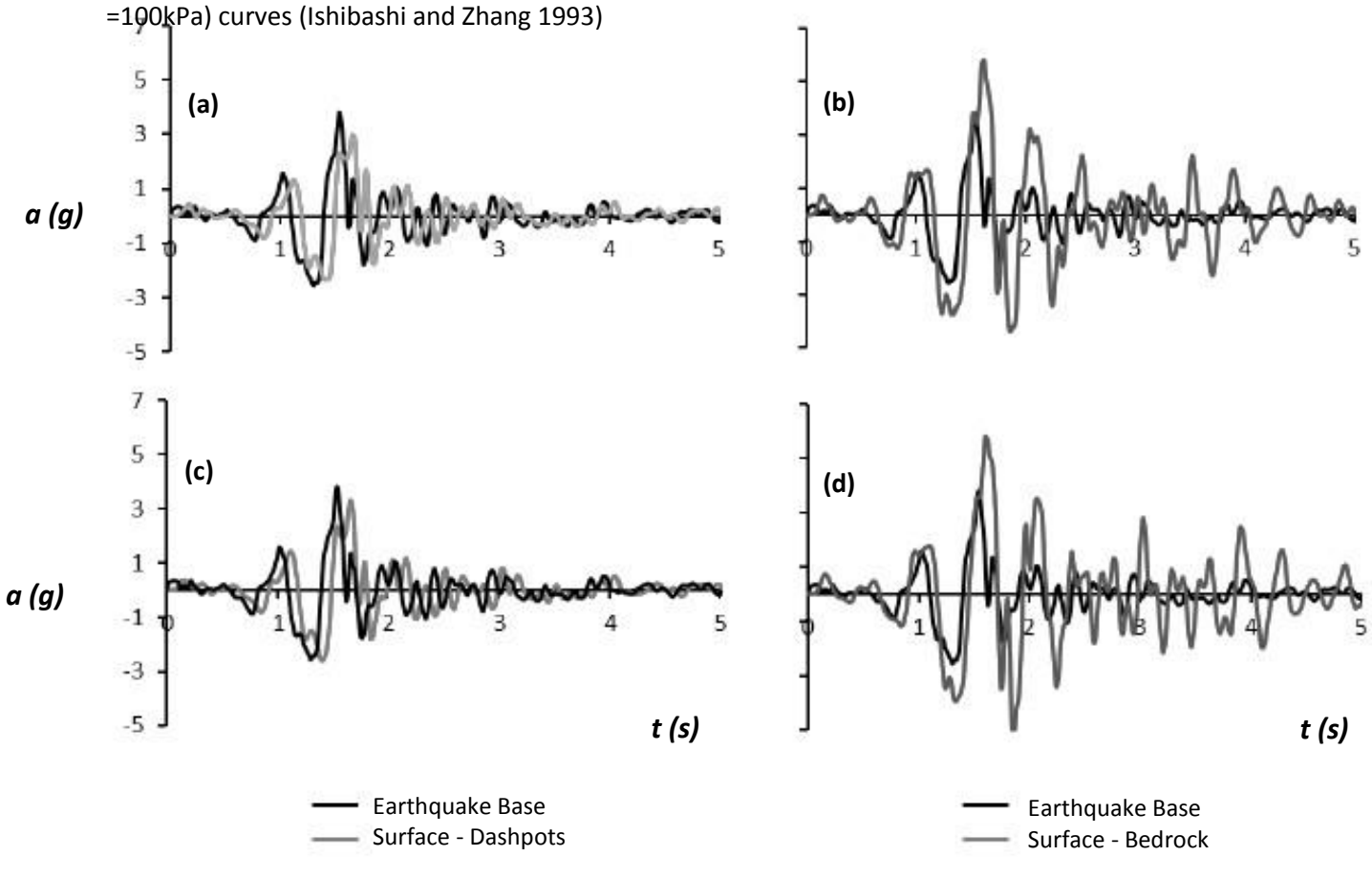

Figure 3.37 Soil amplification with **(a),(c)** and without **(b),(d)** Dashpots at the bottom of the model for Aegio record in longitudinal and transvers direction

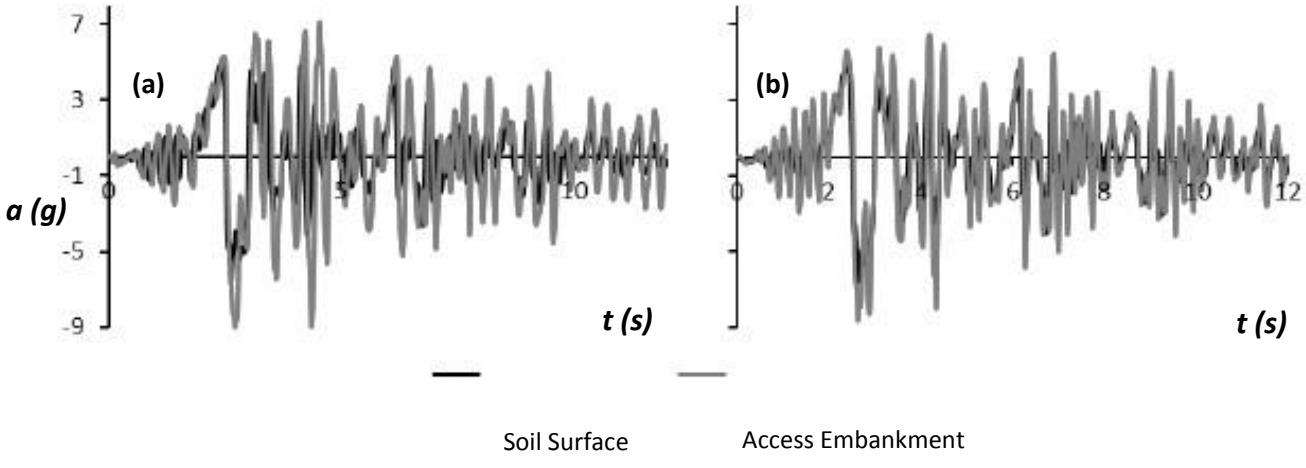

Figure 3.38 Soil amplification for Rinaldi_228 record in **(a)** Longitudinal and **(b)** Transverse direction on access embankment

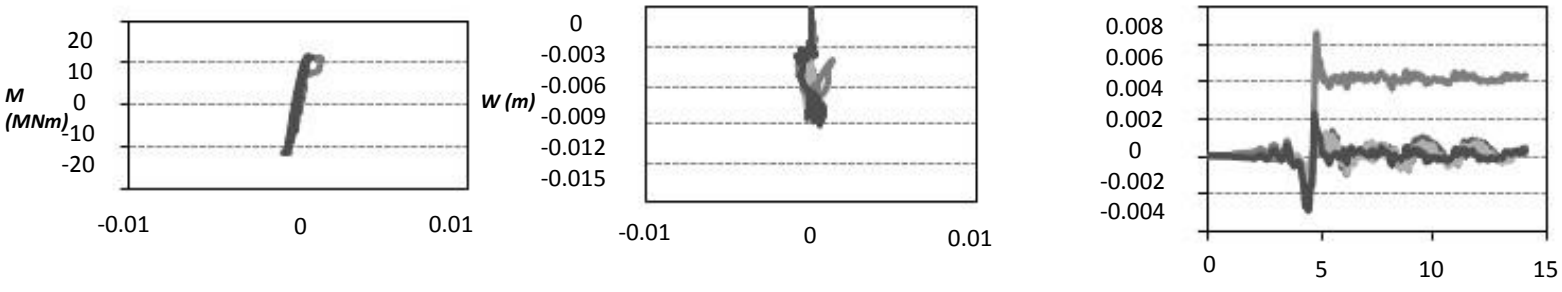

Figure 3.38 (a) Moment-Angle, **(b)** Settlement – Angle and **(c)** Horizontal drift curve of surface foundation for Rinaldi_228 record in Longitudinal direction

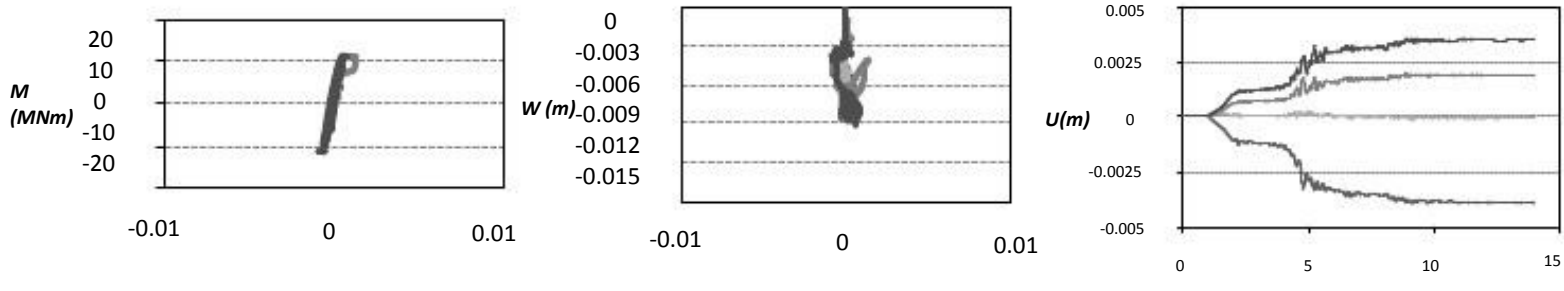

Figure 3.39 (a) Moment-Angle, **(b)** Settlement – Angle and **(c)** Horizontal drift curve of surface foundation for Rinaldi_228 record in Transverse direction

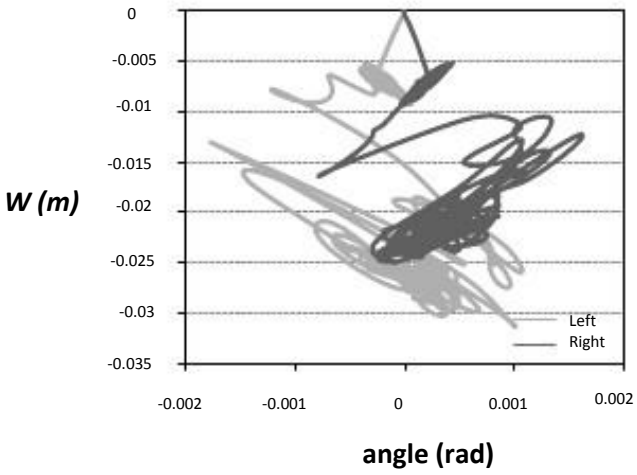

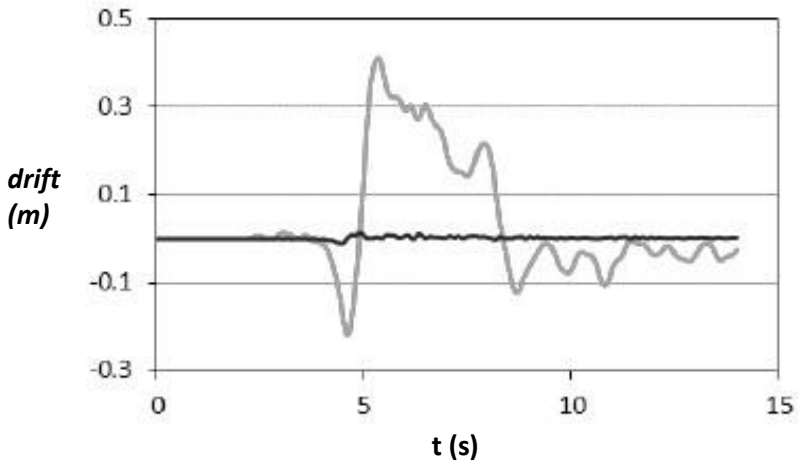

Figure 3.40 (a) Settlement-angle for both retaining walls and **(b)** drift of right retaining wall and displacement of deck for Rinaldi_228 record in Longitudinal direction

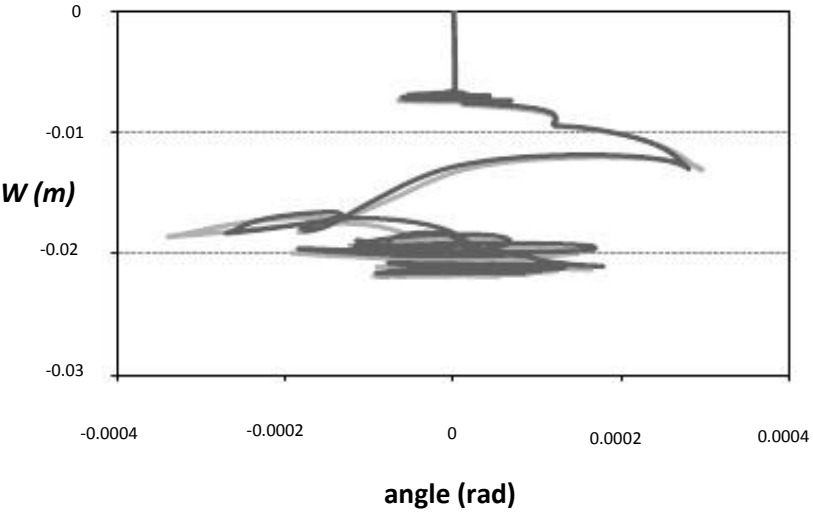

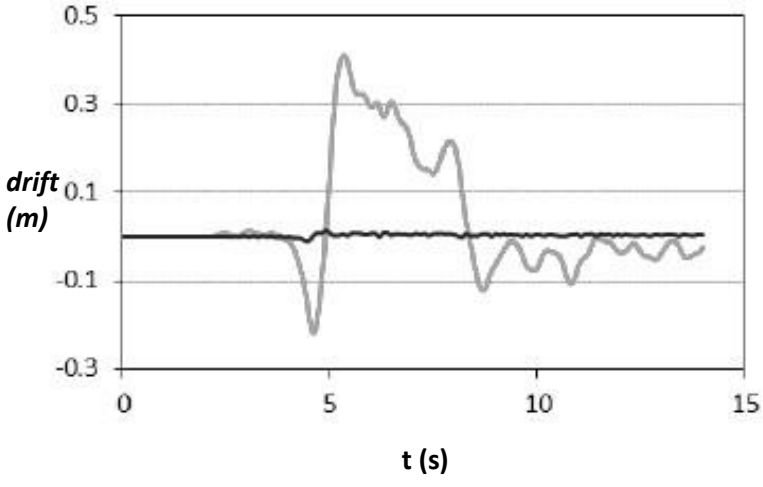

Figure 3.41 (a) Settlement-angle for both retaining walls and **(b)** drift of right retaining wall and displacement of deck for Rinaldi_228 record in Transverse direction

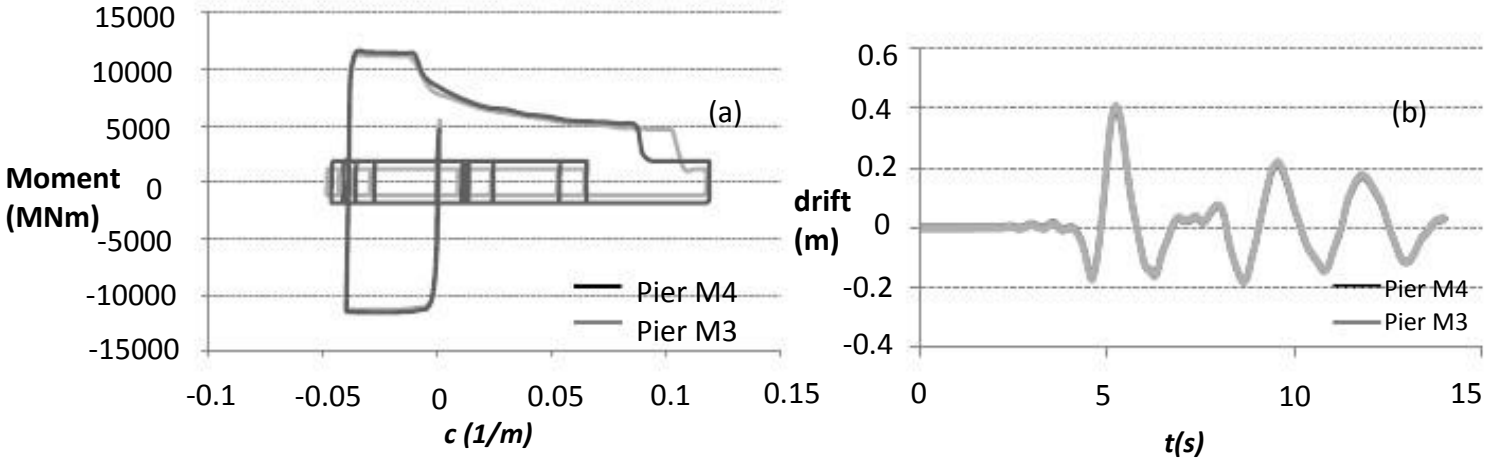

Figure 3.42 (a) Moment-Curvature and **(b)** drift time history for piers 3,4 for Rinaldi_228 record in Longitudinal direction

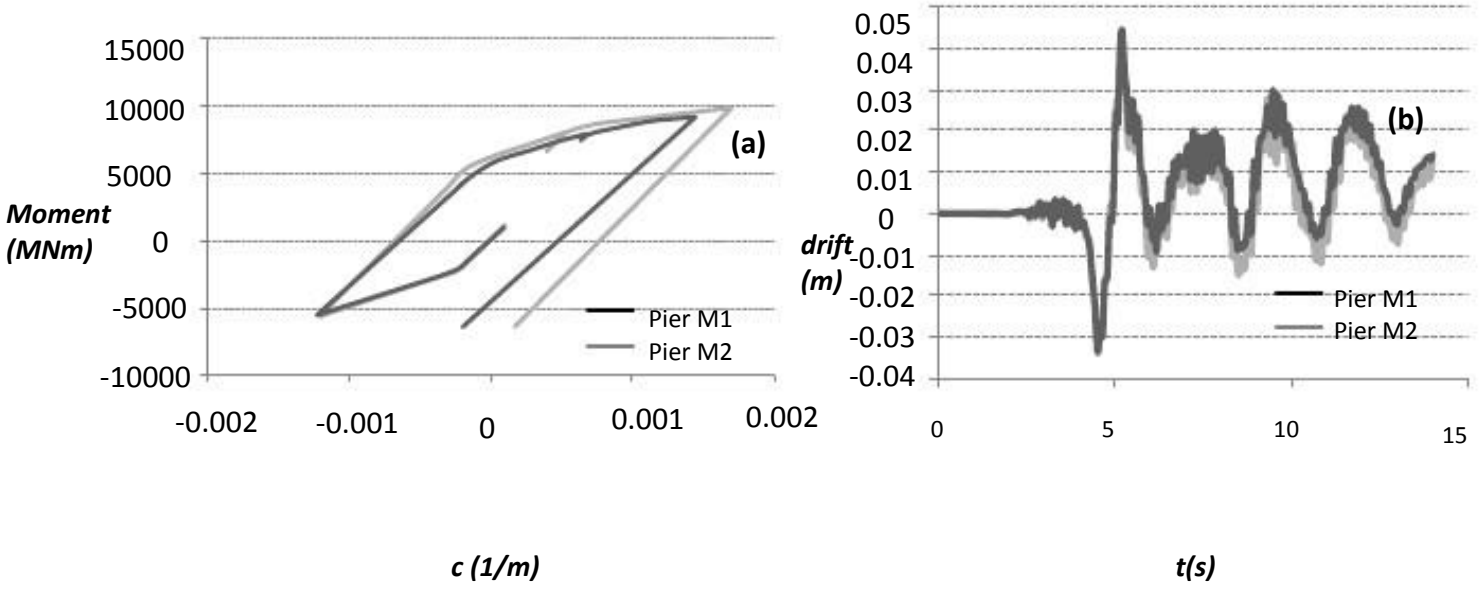

Figure 3.43 (a) Moment-Curvature and **(b)** drift time history for piers 1,2 for Rinaldi_228 record in Longitudinal direction

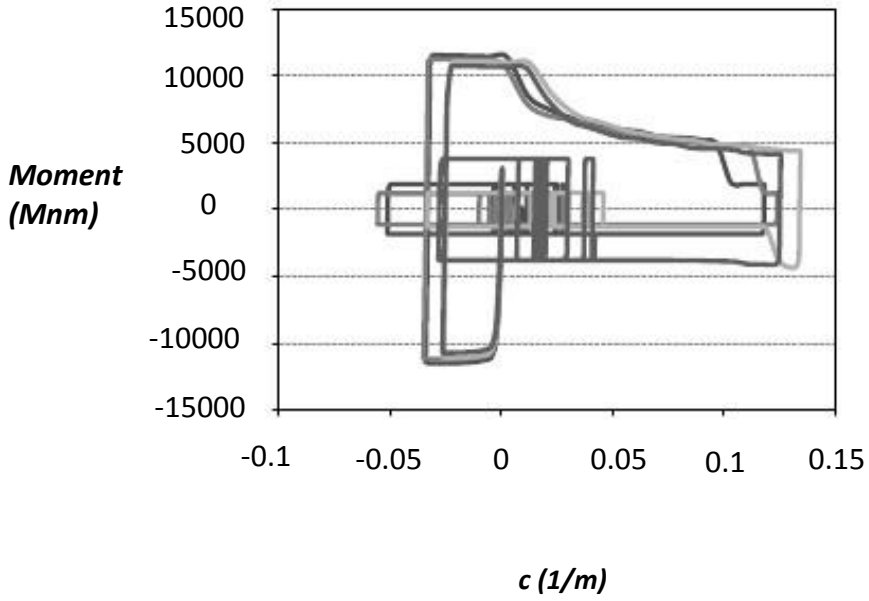

Figure 3.44 (a) Moment-Curvature for piers 1,2,3,4 for Rinaldi_228 record in Transverse direction

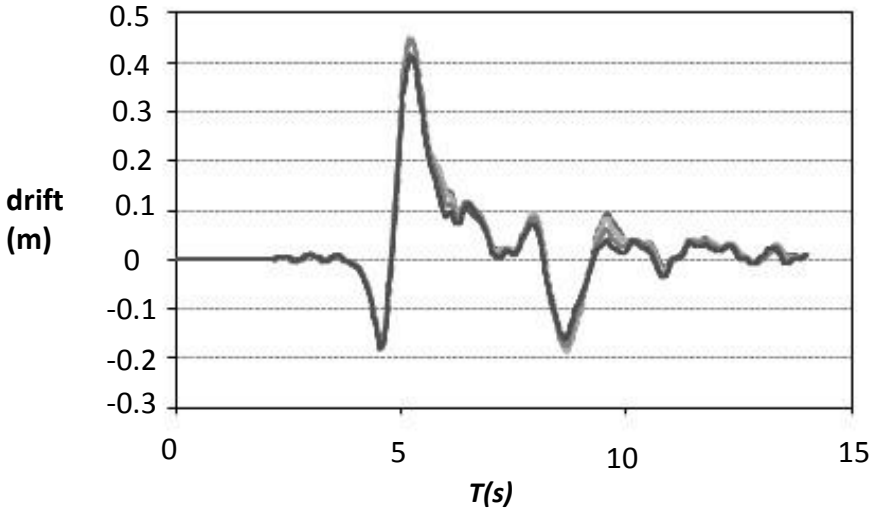

Figure 3.45 (a) Drift time history for piers 1,2,3,4 for Rinaldi_228 record in Transverse direction

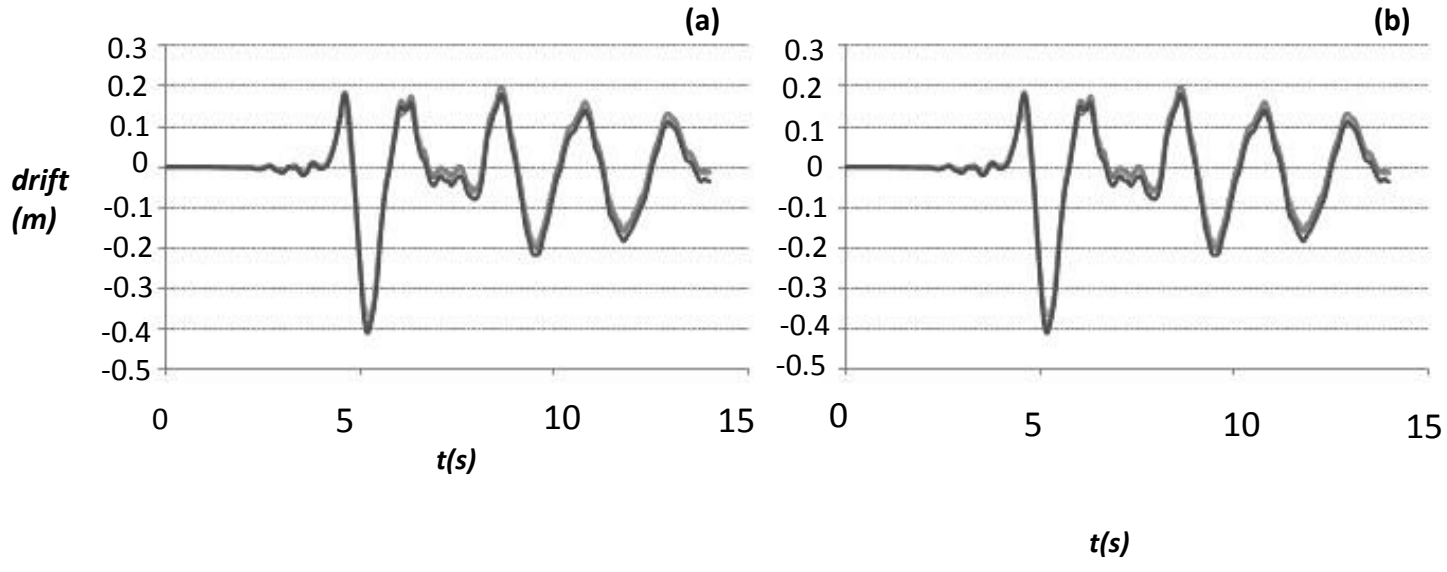

Figure 3.46 Drift time history of bearing in **(a)** longitudinal and **(b)** transverse direction

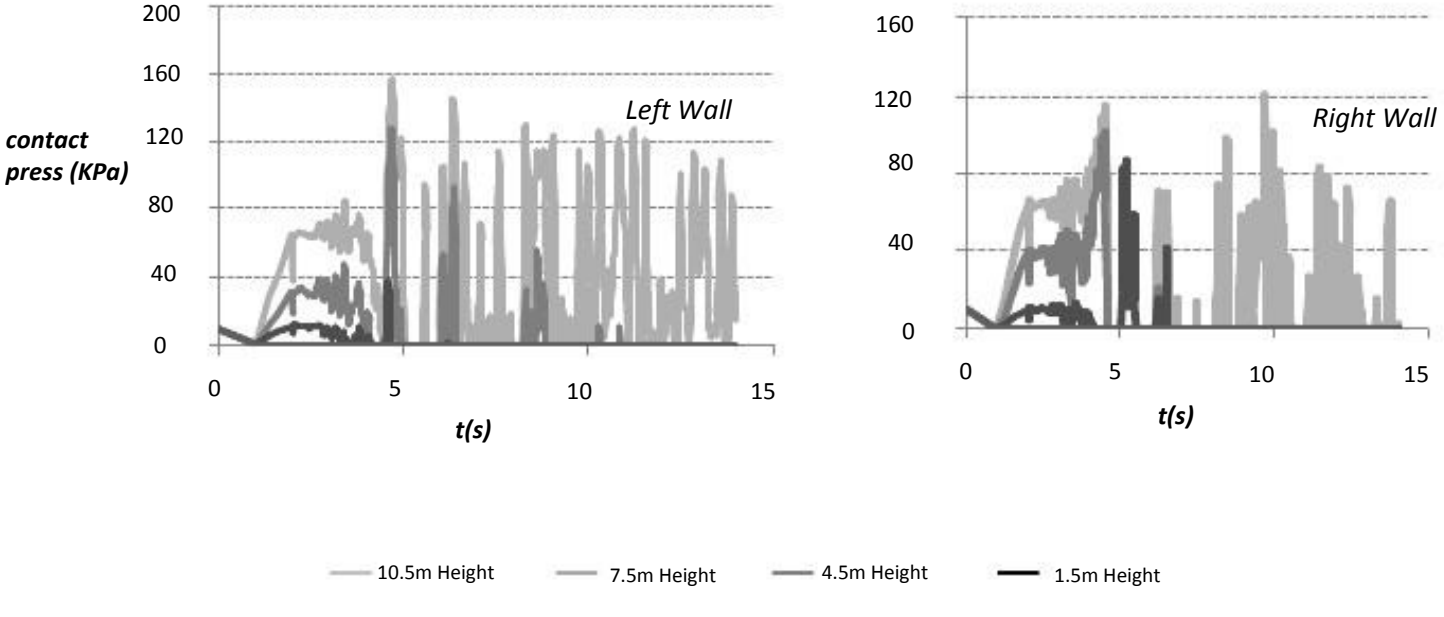

Figure 3.47 Contact Press in both retaining walls in Longitudinal direction for Rinaldi_228 record

CHAPTER 4

THE ABUTMENT STOPPER IN A TYPICAL MOTORWAY BIDGE

4.1 What is the Abutment Stopper?

4.1.1 Role of the Abutment Stopper

Stopper is a large box girder structure which allows the development of the in-service movements of the bridge deck, without transmitting significant loads to the piers and their foundations, while during earthquake they transmit the entire seismic action. The use of stoppers is a very frequent structural measure in current Bridge Engineering, especially in seismically isolated bridges. They are used as a second line of defence as they are designed to reduce the possibility of unseating and to secure the structural integrity of the bridge under extreme seismic movements. Furthermore, the stoppers protect the bearings against excessive seismic deflections and therefore have the ability to control the seismic movements of the deck.

4.1.2 The use of the abutment stoppers in the transverse and longitudinal Direction

Despite the fact that stoppers, which restrain the transverse seismic movements of the deck, are used frequently in seismically isolated bridges, the use of longitudinal stoppers is relatively rare, mainly due to the serviceability needs of the deck, which are critical for the longitudinal direction of the bridge. Serviceability requires the free contraction and expansion of the deck, due to the annual thermal cycle shrinkage, creep and prestress. In current Bridge Engineering, the control of the longitudinal displacements is usually based on the increase in the damping of the structure (Kawashima 2004), which leads to the use of high damping bearings and, rarely, viscous dampers (Eurocode 8 Part 2 2005). The afore mentioned design of bridges can be characterized as conventional, in the sense that the current codes for the design of bridges (Eurocode 8 Part 1 2005; Eurocode 8 Part 2 2005) cover the use and the modeling of these elements, namely bearings and hydraulic dampers.

However, in some cases there are structural solutions which can be implemented in order to change the overall resisting system of the bridge (Saiidi et al. 2001), aiming at controlling its seismic response. For example, in case of integral bridges (Arockiasamy and Sivakumar 2005) the increase in the stiffness of the bridge resisting system, by taking into account the participation of the abutments (Caltrans 1999) and the passive resistance of the backfill soil (Dicleli 2005) usually leads to reductions in the seismic movements of the deck. These reductions are mainly observed in the longitudinal direction of the bridge (Mikami et al. 2008; Mylonakis et al. 1999; Tegos et al. 2005)

Another solution suggests that adequate clearances, namely expansion joints, are required between the longitudinal stoppers and the deck. The expansion joints should have variable magnitudes along the deck, because the constraint in-service movements of the deck are also varying along the length of the bridge. Furthermore, the longitudinal stoppers are not expected to be mobilised simultaneously during earthquake, because the piers, on which the stoppers are installed, respond with different longitudinal displacements.

4.2 Simulation of abutment stoppers

4.2.1 Simulation of abutment stoppers in the longitudinal direction

Firstly, in the longitudinal direction two stoppers are installed, one in each retaining wall. Two new nodes are created one meter left and right of the two outer nodes of the deck. The simulation is consisted of a gap element which connects the new nodes with the outer nodes of the deck (Figure 4.1). Gap elements are two-node elements formulated in three-dimensional space. This element type is only available in a static stress analysis with linear material models and are defined by two end nodes specified in three-dimensional space. Only the element's axial forces are calculated for each element, and depending on the settings, only compressive forces or only tensile forces are generated. A compression gap is not activated until the gap is closed; a tension gap is not activated until the gap is opened. In this case, the gap is considered 10cm. Therefore, the structural behavior of a finite element model associated with gap elements is always nonlinear because of its indeterminate condition, that is, whether the gaps are closed or opened is not known in advance. An iterative solution method is used to determine the status (opened or closed) of the gap elements.

Moreover, the new nodes are tied with a node of the retaining wall under MPC (Multi Point Constraint). A tie type MPC makes all active degrees of freedoms equal at two nodes. Therefore, when the gap closes and the gap element is activated, the deck and the corresponding retaining wall have the same displacement.

The figure 4.2 shows the open-close of the gap in both retaining walls. It is obvious that when the gap opens in the left retaining wall, the gap closes in the right retaining wall. But, it can be easily seen that many times the gap open more than 20cm which is supposed to be the maximum. In addition, taking into account that the gap is 10cm, it is expected that the maximum drift of every node of the deck would not exceed this displacement. Nevertheless, it is observed that the drift of some nodes was larger than 10cm. This happens because the retaining walls are more pliable in the longitudinal direction and tend to turn..The drift of the node at the top of the pier 4 is a sum of node's displacement plus the displacement due to the turn of the retaining wall. The figure 4.3 depicts the comparison in terms of drift for the node at the top of pier 4 before and after the simulation of the stoppers.

4.2.2 Simulation of abutment stoppers in the transverse direction

In the transverse direction four stoppers are installed, two in each retaining wall. Four new nodes are created in the transverse direction one meter left and right of the two outer nodes of the deck. The simulation is consisted of a gap element which connects the new nodes with the outer nodes of the deck (Figure 4.4). Gap elements are two-node elements formulated in three-dimensional space. This element type is only available in a static stress analysis with linear material models and are defined by two end nodes specified in three-dimensional space. Only the element's axial forces are calculated for each element, and depending on the settings, only compressive forces or only tensile forces are generated. A compression gap is not activated until the gap is closed; a tension gap is not activated until the gap is opened. In this case, the gap is considered 10cm. Therefore, the structural behavior of a finite element model associated with gap elements is always nonlinear because of its indeterminate condition, that is, whether the gaps are closed or opened is not known in advance. An iterative solution method is used to determine the status (opened or closed) of the gap elements.

Moreover, the new nodes are tied with a node of the retaining wall under MPC (Multi Point Constraint). A tie type MPC makes all active degrees of freedoms equal at two nodes. Therefore, when the gap closes and the gap element is activated, the deck and the retaining wall have the same displacement.

The figure 4.5 shows the open-close of the gap in both retaining walls. It is obvious that when the gap opens in the left retaining wall, the gap closes in the right retaining wall. In contrast to the longitudinal direction, it can be easily seen that the gap does not open more than 20cm. This is due to the fact that in the transverse direction the stoppers are installed in the same retaining wall and there is no interaction between them. As illustrated in the figure 4.6 , the drifts of the deck are larger in the middle whereas they are gradually reduced near to the retaining walls. The figure 4.7 depicts this comparison in terms of drift for the node at the top of piers 1 and 3 before and after the simulation of the stoppers (Figures 4.8, 4.9). Finally, because of the simulation of the stoppers there is a substantial rise of the moments in the deck (Figure 4.10, 4.11). To be more specific, it is observed an almost fourfold rise of the moments in the transverse direction, which reaches the colossal number of 290 MNm. Nevertheless, nowadays the decks can be constructed prestressed in the transverse direction and are able to hold out these moments.

Chapter 4

Figures

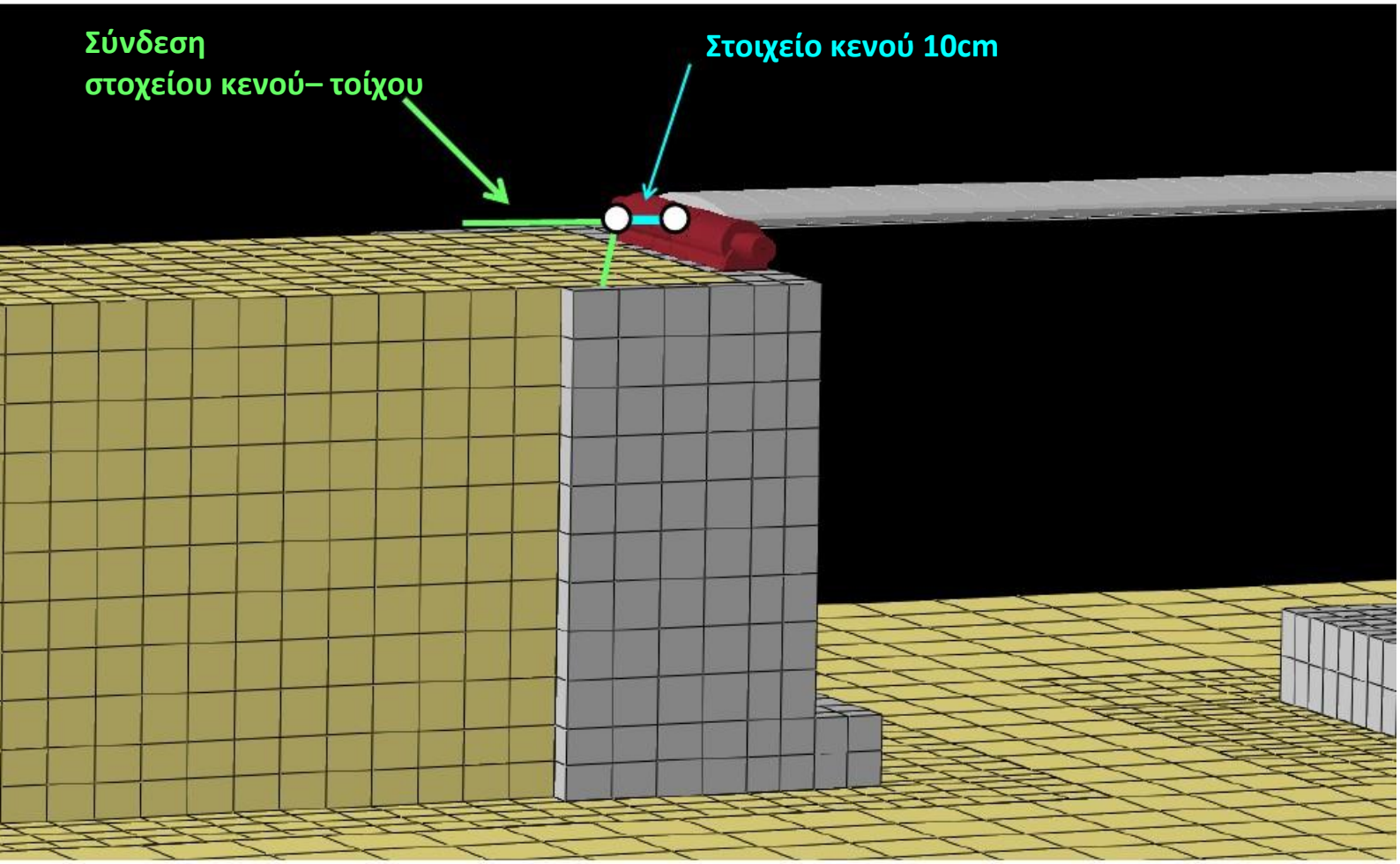

Figure 4.1 Simulation of the stoppers in the longitudinal direction

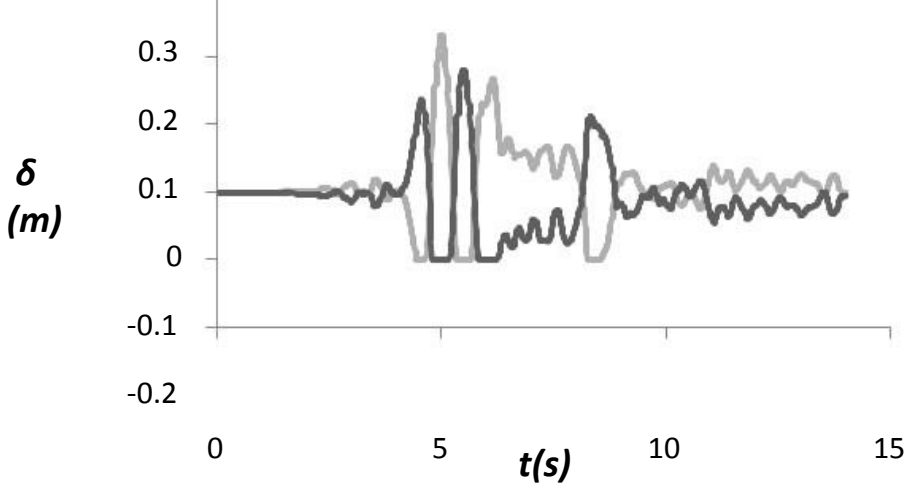

Figure 4.2 Open-close of the gap in the gap element for the Rinaldi_228 record in the Longitudinal direction

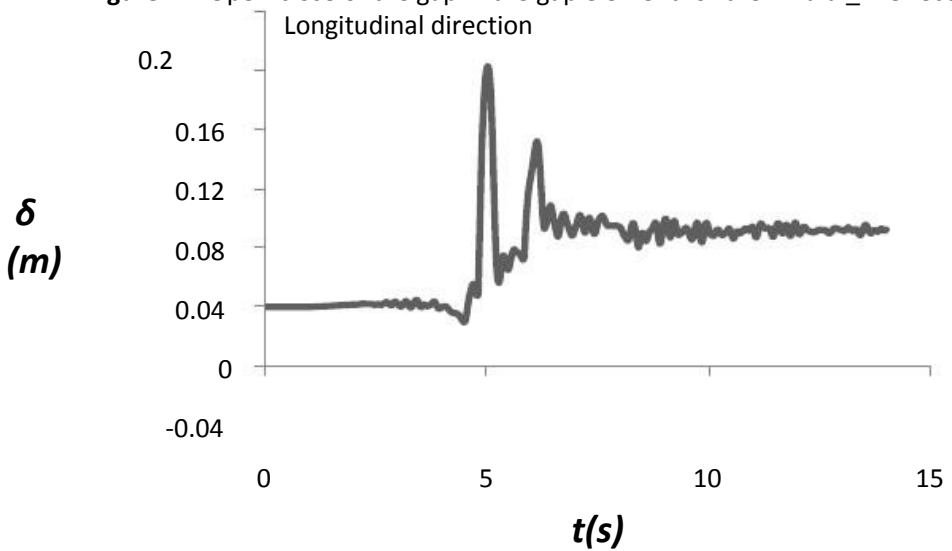

Figure 4.3 Horizontal drift of the wall for the Rinaldi_228 record in the Longitudinal direction

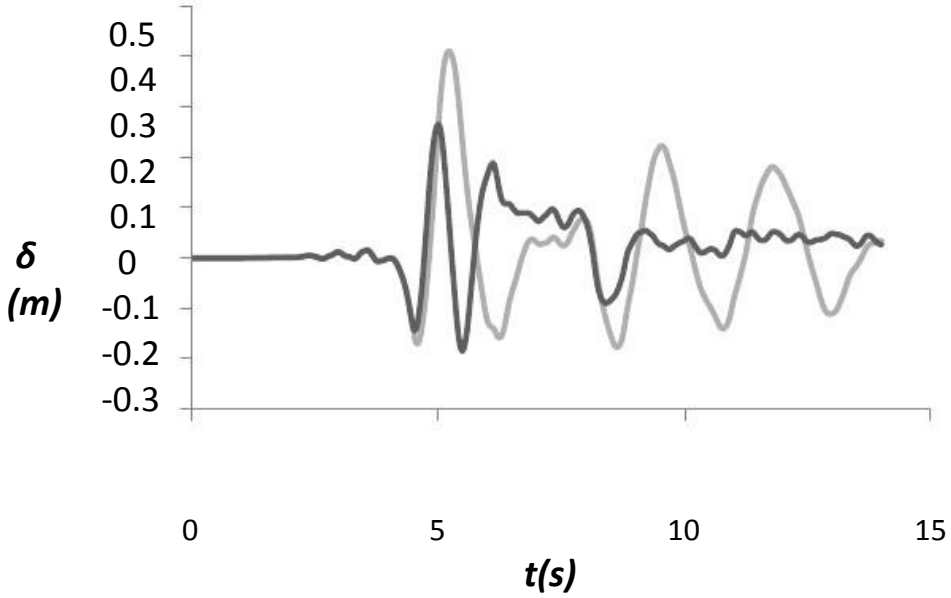

Figure 4.4 Horizontal drift of the pier 4 for the Rinaldi_228 record in the Longitudinal direction

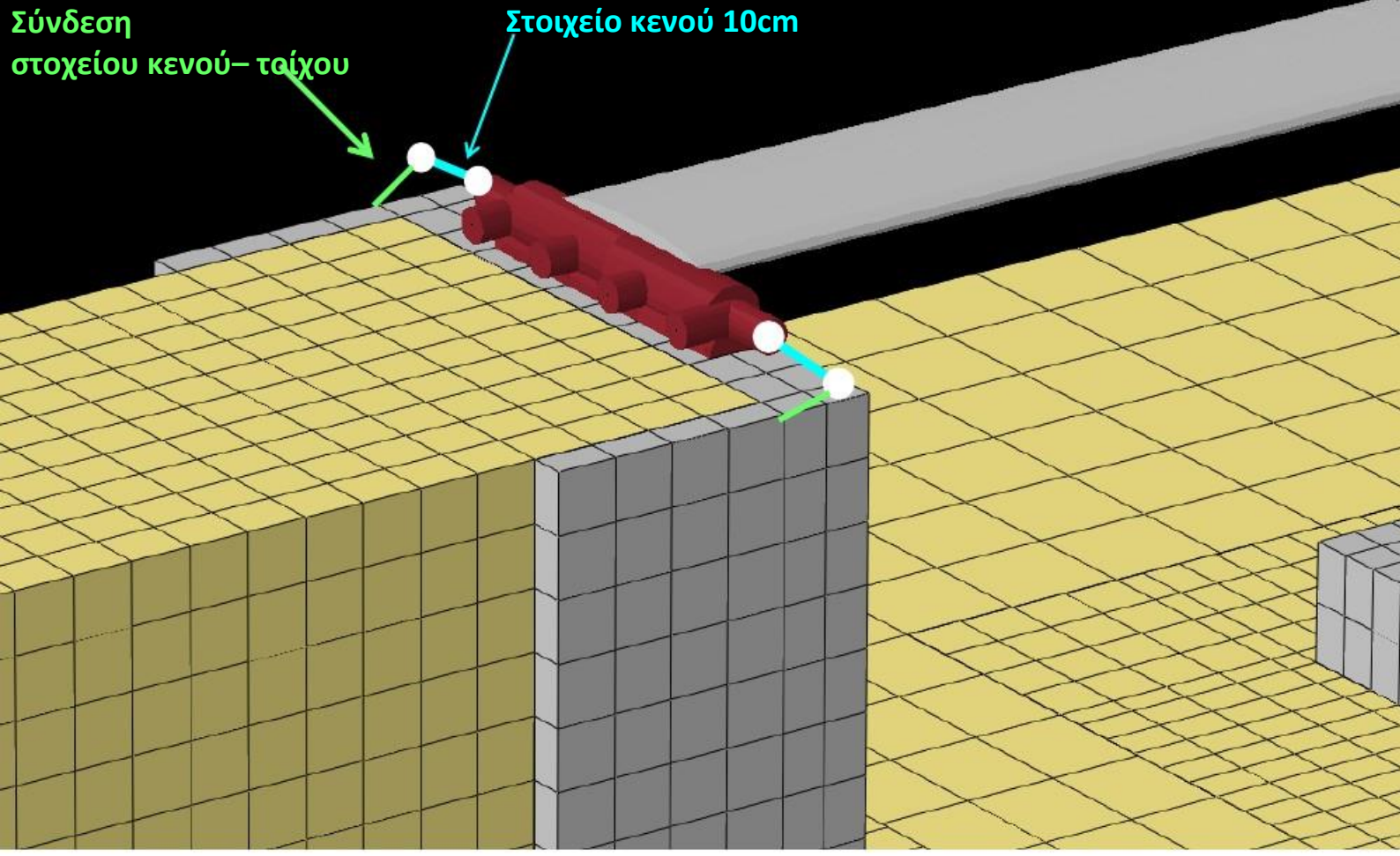

Figure 4.5 Simulation of the stoppers in the Transverse direction

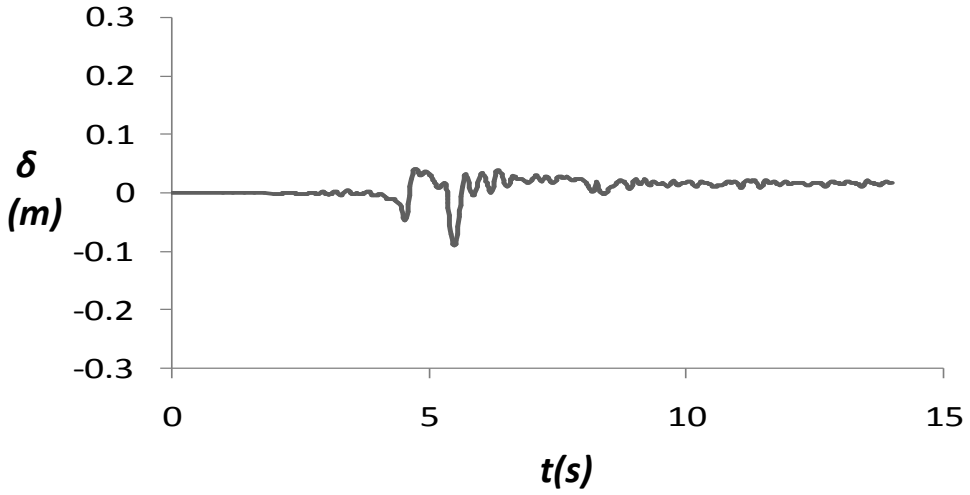

Figure 4.7 Horizontal drift of the wall for the Rinaldi_228 record in the Transverse direction

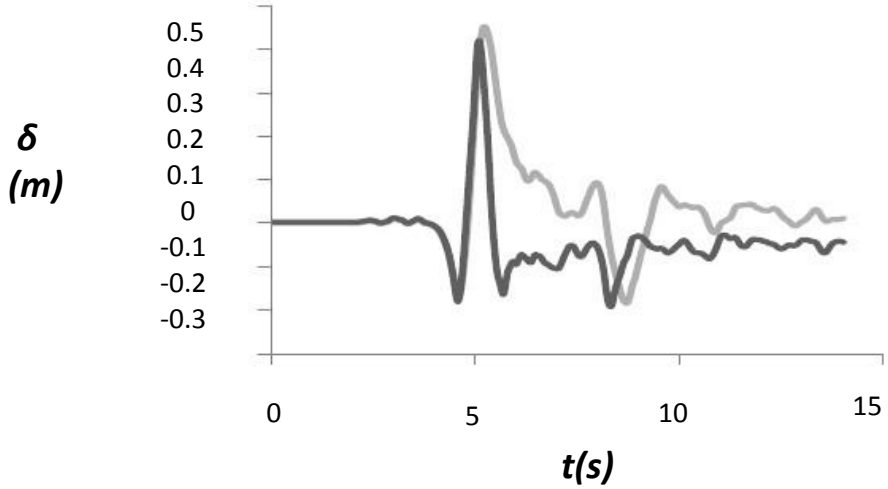

Figure 4.8 Horizontal drift of the pier 3 for the Rinaldi_228 record in the Transverse direction

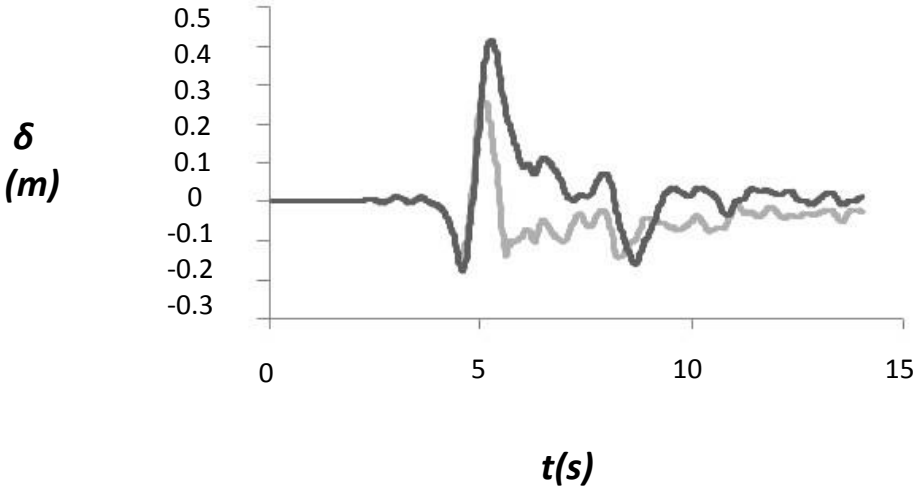

Figure 4.9 Horizontal drift of the pier 1 for the Rinaldi_228 record in the Transverse direction

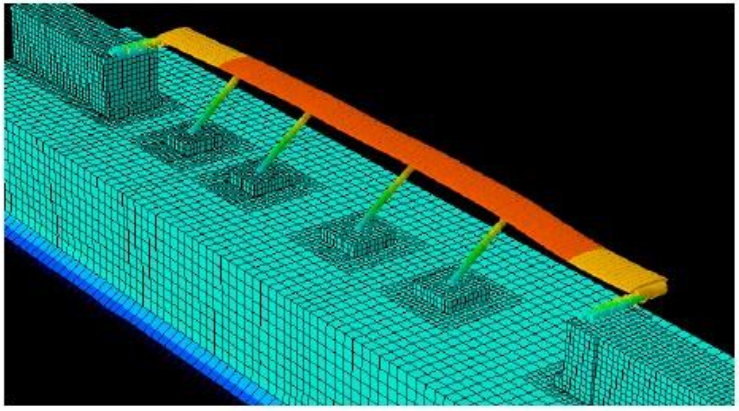

Figure 4.10 Displacement of the deck in the Transverse direction without the simulation of stoppers

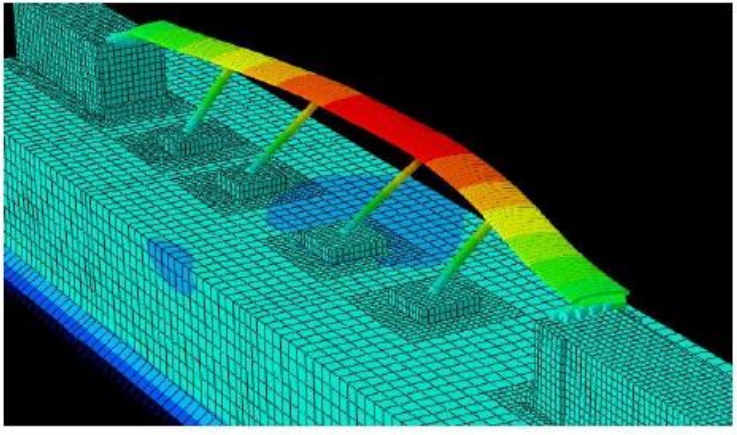

Figure 4.11 Displacement of the deck in the Transverse direction with the simulation of stoppers

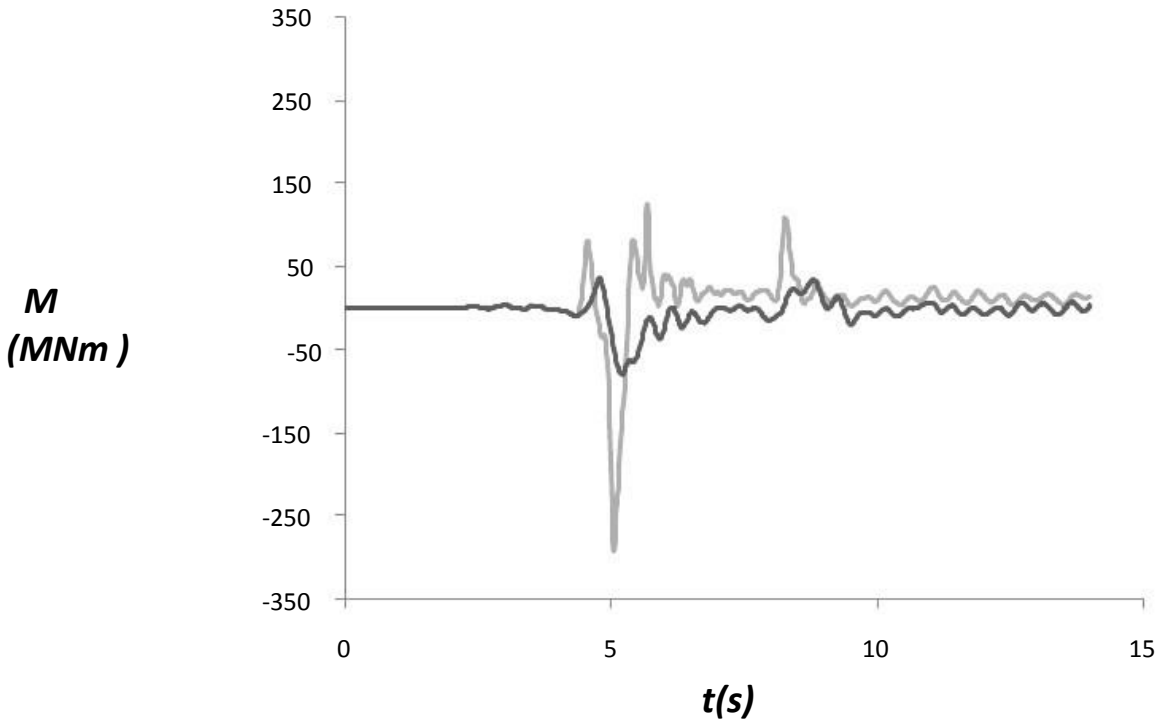

Figure 4.12 Moments in the deck for the Rinadi_228 record in the Transverse direction with and without the simulation of stoppers

CHAPTER 5

ROCKING ISOLATION- EFFECT OF NON-LINEAR SSI

5.1 Introduction

It has been more than 30 years since the realization of the earthquake engineering community that the increase of strength of a structural system does not necessarily enhance safety. This recognition has lead to the development of new design principles, aiming at rationally controlling seismic damage and rendering the structure “fail-safe”. A fail-safe system can be defined as a system in which failure of some elements or subsystems, caused by unexpectedly extreme loading, does not lead to the collapse because an alternative load path is developed by the remaining elements or subsystems (Frangopol and Curley 1987). Accepting that failure of structural members cannot always be avoided, earthquake engineering research focused on ensuring: (1) that structural members can sustain dynamic loads that exceed their strength without collapsing—ductility design; (2) that failure is “guided” to members that are less important for the overall integrity of the structure (i.e. beams instead of columns); and (3) that failure is in the form of non-brittle mechanisms (bending instead of shear failure)— capacity design (Park and Paulay 1975).

However, while substantial research and regulatory efforts have been devoted to developing “fail-safe” (robust) structures, less attention has been given to the soil-structure system as a whole. Capacity design principles mainly refer to the superstructure, usually underestimating the effect of soil and foundation. In the words of Priestley (2000) “the incorporation of foundation compliance effects into force-based design is generally carried out inadequately, if at all”. Even when foundation compliance is taken into account, little care is given to the nonlinearity of soil and foundation. In fact, current practice in seismic “foundation” design, particularly as entrenched in seismic codes (e.g. EC8), attempts to avoid the mobilization of “strength” in the foundation. In structural terminology: no “plastic hinging” is allowed in the foundation-soil system. In simple geotechnical terms, the designer must ensure that the foundation system will not even reach a number of “thresholds” that would conventionally imply failure. Thus, the following states are prohibited:

• mobilization of the “bearing-capacity” failure mechanisms under cyclically-uplifting

shallow foundations;

• sliding at the soil-footing interface or excessive uplifting of a shallow foundation;

• passive and shear failure along the sides and base of an embedded foundation;

“Overstrength” factors plus (explicit and implicit) factors of safety larger than 1 are introduced against each of the above “failure” modes, as in static design. Although such a restriction may appear reasonable (the inspection and rehabilitation of foundation damage after a strong earthquake is not easy), it may lead to nonconservative oversimplifications, especially in the case of strong geometric nonlinearities, such as foundation uplifting and sliding (e.g. Harden and Hutchinson 2006). Most importantly, neglecting such phenomena prohibits the exploitation of strongly non-linear energy dissipating mechanisms in defense of the superstructure in case of occurrence of ground motions larger than design. Today, a growing body of evidence suggests that soil-foundation plastic yielding under seismic excitation is not only unavoidable, but may even be beneficial.

A new seismic design philosophy, in which yielding of the soil-foundation system is “utilised” to protect the superstructure—exactly the opposite of conventional capacity design (in which plastic “hinging” is restricted to the superstructure). Figure 5.1 schematically illustrates the difference between conventional design and the new concept, and provides a real example of plastic “hinging” in the superstructure (Fig. 5.2), and a real example of unintended plastic “hinging” in the foundation (Fig. 5.3). The latter shows the excessive tilting of a slender building on very soft soil in Adapazari (Turkey, 1999),where soil failure can be seen to have (unintentionally) acted as a “shield” for the superstructure, which remained structurally unscathed. Naturally there is always a price to pay, which is none other than permanent rotation and settlement—in this particular case excessive, but not always so.

The need for this “reversal” of current seismic design stems from:

(a) The inherent uncertainty of predicting the maximum credible earthquake and determining the characteristics of the corresponding seismic motion (PGA, PGV, frequency content, duration, details). For example, the notorious 1995 Mw7.2 Kobe earthquake was generated by an unknown fault, generating PGAs of up to 0.85 g, compared to 0.3 g of the design code (e.g. Gazetas et al. 2005). In fact, in each new earthquake larger PGAs are recorded. A recent example is the “long-awaited” 2004Mw6.0 Parkfield earthquake, where the maximum recorded PGA at close proximity to the seismogenic fault reached 1.8 g, accompanied by PGVs of the order of 100 cm/s (Shakal et al. 2006). Interestingly, there were several other records at similar distances from the fault where the PGAs were even an order ofmagnitude lower! Such observations lead to the conclusion that the probability of occurrence of such large near-fault PGAs can be substantial. On the other hand, the probability of capturing such records can be seen as a function of the density of accelerograph networks: i.e. it was the extreme density of instrumentation that allowed the recording of the aforementioned PGAs.

Obviously, if the fault was not well-documented, and money had not been spent on instrumentation, these records would not exist. With such evidence, the challenge of defining upper bounds on earthquake ground motions (Bommer et al. 2004) can be seen from a different perspective. Therefore, it is considered logical to accept that the risk of occurrence of seismic ground motions larger than assumed in design will always be substantial. Naturally, the magnitude of this risk will depend on the assumed earthquake hazard levels. On the other hand, evidence is accumulating that shows that PGA (alone) is not the crucial parameter.

The frequency content, the pulse sequence, and the asymmetry of motion, may indeed be of more importance (e.g. Makris and Roussos 2000; Fardis et al. 2003). It is therefore important to develop new design methods that will allow structures to withstand earthquakes larger than assumed in design without collapsing or sustaining un-repairable damage.

(b) The necessity of developing economically efficient earthquake protection solutions. The era of global economic crisis urgently calls for a drastic reappraisal of our way of thinking. Seismic safety and protection of human life is—and must remain—the first priority. However, a typical structure will have to withstand a strong earthquake only once or twice in its life. Hence, economy and respect to the environment should also play a role in the design process. So, instead of building larger and stronger (more expensive) foundations to make sure that strong seismic shaking will manage to get to the superstructure (i.e. conventional capacity design), and then reinforce the superstructure so that it may withstand the earthquake without collapsing (making it also more expensive and consuming more-and-more material resources), why not do exactly the opposite : intentionally under-design the foundations to act as “safety valves”, limiting the acceleration transmitted onto the superstructure. This way, we may achieve economy in the foundation and the superstructure, without undermining safety. In fact, as it will be shown in the sequel, due to the substantially larger ductility capacity of soil failure mechanisms compared to structural yielding, the new design philosophy may provide increased safety margins.

To unravel the effectiveness of the new design philosophy (compared to conventional capacity design), two realistic bridge structures of the Greek Metropolitan Motorway ''Attiki odos'', A01_TE20 and A01_TE23, are used as examples. The results presented herein can be seen as a demonstration of the potential advantages of the new concept.

Two different foundation widths are considered to represent the two alternative design approaches.

1) A larger foundation, B = 8 m, which is the real one and it is designed in compliance with conventional capacity design, ensuring that the plastic “hinge” will develop in the superstructure (base of pier).

2)A smaller, under-designed, B = 5m foundation is considered in the spirit of the new design philosophy. As it will be shown below, the *underdesigned* foundation will not allow the design seismic action to develop..

5.2. Dynamic time-history analysis

The seismic performance of the two alternatives is investigated through nonlinear dynamic time history analysis. An ensemble of 2 real accelerograms are used as seismic excitation of the soil-foundation-structure system in the transverse and longitudinal direction. In all cases, the seismic excitation is applied at the dashpot level. As depicted in figure 5.4, the selected records are : a) Aegion record, b) Rinaldi_228 record. The first one is a seismic motion that do not exceed the design limits, whereas the second one exceeds seriously the design limits.

5.2.1 Longitudinal direction of A01_TE23

The comparisons made examine the seismic behavior of the 3rd and 4th pier of the bridge which are not seismically isolated in the longitudinal direction.

a)Aegion Record

The record from the 1995 Ms 6.2 Aegion (Greece) earthquake can be considered as a moderate intensity seismic excitation. Although its elastic response spectrum exceeds the design spectrum for the range of periods between 0.4 and 0.8 s (Fig. 5.4), due to its characteristically short duration and the presence of (practically) a single strong motion pulse of moderate acceleration amplitude (0.37 g), it is reasonably considered as a seismic motion within the limits of the design.

In Fig. 5.5 the comparison is portrayed in terms of the foundation experienced moment– rotation ($M-\theta$) . As expected, while the response of the conventionally designed foundation of these piers is practically elastic (Fig. 5.5.1), the *under-designed* foundation (new design philosophy) experiences some inelasticity (Fig. 5.5.2).

In Fig. 5.6 the comparison is in terms of foundation settlement– rotation ($w-\theta$). The conventionally designed system is subjected to limited settlement $w \approx 0.4$cm (Fig. 5.6.1). In marked contrast, the *new concept* (Fig. 5.6.2) experiences larger but still limited dynamic settlement: $w \approx$ 1cm (Pier 4).

Figure 5.7 illustrates the moment–curvature response at the base of the pier for the conventionally designed system. Some inelasticity takes place, but the curvature ductility is tolerable: the demand is almost an order of magnitude lower than the capacity of the reinforced concrete section. In the case of the new design philosophy, thanks to foundation yielding the response of the pier is purely elastic. The time histories of deck horizontal displacement, i.e. the *drift Δ,* for the two alternatives are compared in Fig. 5.8. As graphically illustrated in the adjacent sketch notation, the drift has two components (see also Priestley et al. 1996): (i) the "*flexural drift*" Δc, i.e. the structural displacement due to flexural distortion of the pier column, and (ii) the *"rocking drift*" $\Delta r = \theta H$, i.e. the displacement due to rocking motion of the foundation. This way, the contribution of pier flexural distortion and foundation rotation to the final result of interest (i.e. the total drift Δ) can be inferred. As might have been expected, while for the conventional design (*over-designed foundation*) Δ is mainly due to pier distortion Δc, exactly the opposite is observed for the *under-designed* foundation of the new design philosophy: Δ is mainly due to foundation rotation Δr. Nevertheless, despite the differences in the mechanism leading to its development (pier distortion versus foundation rotation), the residual and maximum drift is quite similar.

b)Rinaldi_228 record

The Rinaldi record from the devastating 1994 Ms 6.7 Northridge earthquake is utilized herein as an illustrative example of very strong seismic shaking, substantially exceeding the design limits. Containing a well-distinguished, long-duration asymmetric acceleration pulse of 0.82 g (being the result of forward-rupture directivity effects), it generates an elastic response spectrum overly exceeding the design.

Figure 5.9 compares the response of the two alternatives, in terms of deformed mesh with superimposed plastic strain. In the conventionally designed system (Fig. 5.9.1) there is no inelastic action in the soil. In stark contrast, with the new design scheme (Fig. 5.9.2) the "plastic hinge" takes the form of mobilisation of the bearing capacity failure mechanisms in the underlying soil, leaving the superstructure totally intact. Notice that the red regions of large plastic shearing are of large extent, indicating alternating mobilisation of the bearing capacity failure mechanism.

As seen in Fig. 5.10, the piers of the conventional system suffer a curvature ductility exceeding the design limit by almost one order of magnitude—clearly a case of collapse.

In Fig.5.11 the comparison is in terms of deck drift Δ of the two piers. It can be seen that in the rocking-isolation concept the drifts of the piers 3 and 4 are reduced by 17% and 20% respectively. They experience substantial maximum deck drift (about 22 cm), almost exclusively due to foundation rotation Δr . Nevertheless, the residual foundation rotation leads to a tolerable 3cm deck horizontal displacement at the end of the earthquake.

The moment–rotation (M– θ) response of the two foundations is depicted in Fig. 5.12. Respecting its design principles, the conventional B = 8m foundation-soil system remains practically elastic (Fig. 5.12.1); the causes are now evident: (i) the rocking stiffness of the foundation, being proportional to B^3, is large and leads to small stresses in the soil; and (ii) pier failure effectively limits the loading transmitted onto the foundation. Exactly the opposite is observed for the *under-designed* (B = 5m) foundation, the response of which is strongly inelastic (Fig. 5.12.2): mobilisation of bearing capacity failure acts as a *"safety valve"* or a *"fuse"* for the superstructure. But despite such excessive soil plastification, not only the structure does not collapse, but the residual (permanent) rotation is rather limited. Under static conditions, the development of this rotational mechanism on either side of the foundation would have lead to toppling of the structure. However, dynamically, each "side" of the rotational mechanism deforms plastically for a very short period of time ("momentarily"), producing limited inelastic rotation which is partially cancelled by the ensuing deformation on the opposite side. Obviously, exactly the same applies to structural plastic "hinging" in conventional design. The main difference between the two alternatives lies in the mechanism of energy dissipation, and the related displacement ductility margins.

However, energy dissipation is not attainable at zero cost: in some cases the cost is the increase of foundation settlement but in our case there is not an excessive increase of the foundation settlement . Figure 5.13 compares the settlement–rotation (w– θ) response for the two alternatives.

While the practically elastic response of the conventional (*over-designed*) foundation leads to a minor 1cm (pier 4) settlement (Fig. 5.13.1), the *under-designed* foundation of the new philosophy experiences an increased 4cm settlement (Fig. 5.13.2), which remains insignificant.

5.2.2 Transverse direction of A01_TE23

The comparisons made examine the seismic behavior of all the piers of the bridge.

a) Aegio record

In Fig. 5.14 the comparison is portrayed in terms of the foundation experienced moment– rotation (M– θ) . As expected, while the response of the conventionally designed foundation of these piers is practically elastic (Fig. 5.14.1), the *under-designed* foundation (new design philosophy) experiences some inelasticity (Fig. 5.14.2).

In Fig. 5.15 the comparison is in terms of foundation settlement– rotation (w– θ). The conventionally designed system is subjected to limited settlement $w \approx 0.5$cm (Fig. 5.15.1). In marked contrast, the *new concept* (Fig. 5.15.2) experiences larger but still insignificant dynamic settlement: $w \approx 0.7$ cm (Pier 4).

Figure 5.16 illustrates the moment–curvature response at the base of the pier for the conventionally designed system. Some inelasticity takes place, but the curvature ductility is tolerable: the demand is almost an order of magnitude lower than the capacity of the reinforced concrete section. In the case of the new design philosophy, thanks to foundation yielding the response of the piers 3,4 is very close to elastic, while the piers 1,2 show slight inelasticity. The time histories of deck horizontal displacement, i.e. the *drift Δ,* for the two alternatives are compared in Fig. 5.17. As graphically illustrated in the adjacent sketch notation, the drift has two components (see also Priestley et al. 1996): (i) the "*flexural drift*" Δc, i.e. the structural displacement due to flexural distortion of the pier column, and (ii) the *"rocking drift*" $\Delta r = \theta H$, i.e. the displacement due to rocking motion of the foundation. This way, the contribution of pier flexural distortion and foundation rotation to the final result of interest (i.e. the total drift Δ) can be inferred. As might have been expected, while for the conventional design (*over-designed foundation*) Δ is mainly due to pier distortion Δc , exactly the opposite is observed for the *under-designed* foundation of the new design philosophy: Δ is mainly due to foundation rotation Δr. Nevertheless, despite the differences in the mechanism leading to its development (pier distortion versus foundation rotation), the residual and maximum drift is quite similar.

b)Rinaldi_228 record

As seen in Fig. 5.18, the piers of the conventional system suffer a curvature ductility exceeding the design limit by almost one order of magnitude—clearly a case of collapse.

The moment–rotation (M– θ) response of the two foundations is depicted in Fig. 5.19. Respecting its design principles, the conventional B = 8m foundation-soil system remains practically elastic (Fig. 5.19.1); the causes are now evident: (i) the rocking stiffness of the foundation, being proportional to B^3, is large and leads to small stresses in the soil; and (ii) pier failure effectively limits the loading transmitted onto the foundation. Exactly the opposite is observed for the *under-designed* (B = 5m) foundation, the response of which is strongly inelastic (Fig. 5.19.2): mobilisation of bearing capacity failure acts as a *"safety valve"* or a *"fuse"* for the superstructure. But despite such excessive soil plastification, not only the structure does not collapse, but the residual (permanent) rotation is rather limited. Under static conditions, the development of this rotational mechanism on either side of the foundation would have lead to toppling of the structure. However, dynamically, each "side" of the rotational mechanism deforms plastically for a very short period of time ("momentarily"), producing limited inelastic rotation which is partially cancelled by the ensuing deformation on the opposite side. Obviously, exactly the same applies to structural plastic "hinging" in conventional design. The main difference between the two alternatives lies in the mechanism of energy dissipation, and the related displacement ductility margins.

However, energy dissipation is not attainable at zero cost: in some cases the cost is the increase of foundation settlement but in our case there is not an excessive increase of the foundation settlement . Figure 5.20 compares the settlement–rotation (w– θ) response for the two alternatives. While the practically elastic response of the conventional (*over-designed*) foundation leads to a minor 1cm (pier 4) settlement (Fig. 5.20.1), the *under-designed* foundation of the new philosophy experiences an increased 4cm settlement (Fig. 5.20.2), which remains insignificant.

Results consistenly indicate the superior performance of the rocking isolated alternative, especially when subjected to large intensity seismic shaking substantially exceeding the design limits (i.e., when ''life safety'' is the primary concern). The comparisons made in the previous figures where the performance of the two design alternatives of the bridge AO1_TE23 subjected to the strong seismic shaking of Rinaldi are shown in terms of moment-curvature response of the piers and moment-settlement response of the foundation. Hence, while the conventionally designed system of piers appears bound to collapse in both directions, with the ductility demands overly exceeding the capacity of the piers, the rocking-isolated system survives such tremendous seismic shaking practically unscathed. Presumably, its superior performance is directly associated to strongly inelastic foundation response, unavoidably leading to an increase of foundation settlement.

Chapter 5

Figures

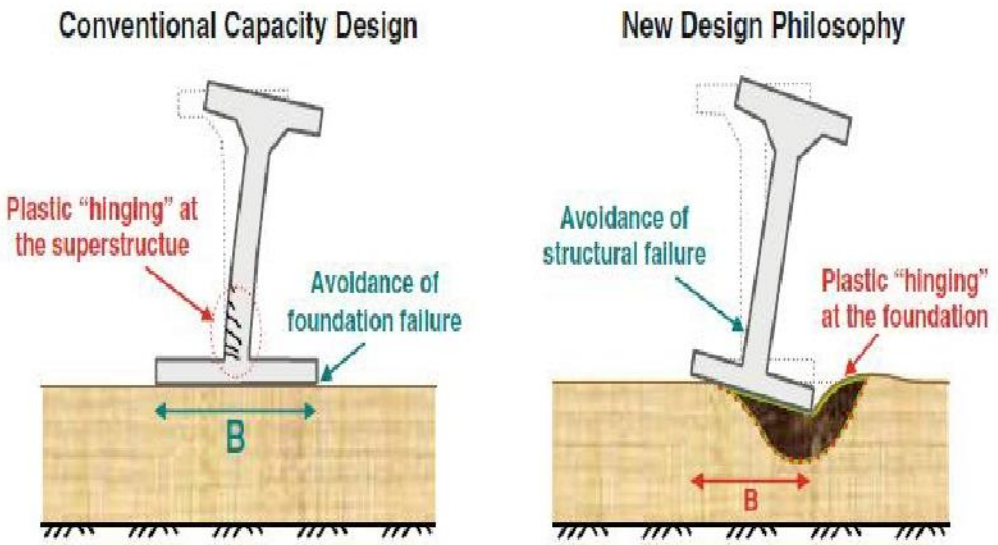

Figure 5.1

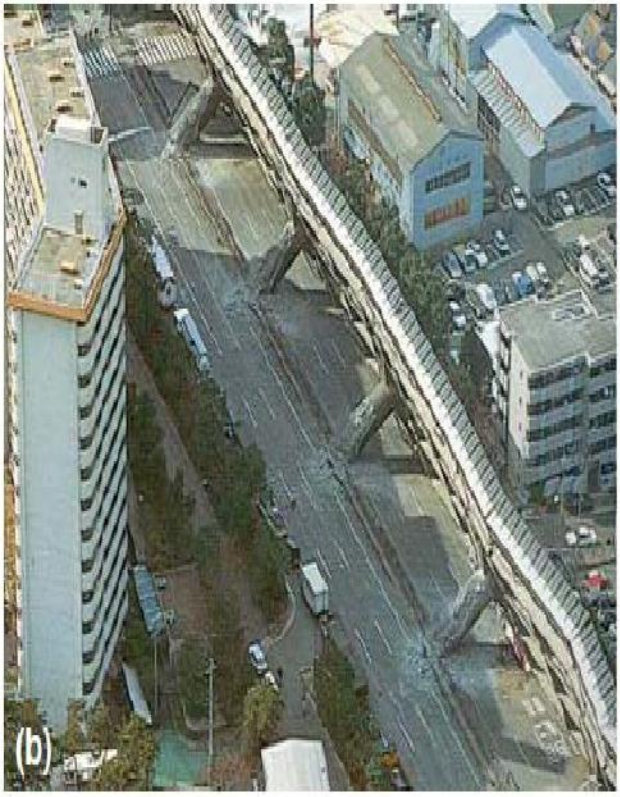

Figure 5.2

Figure 5.3

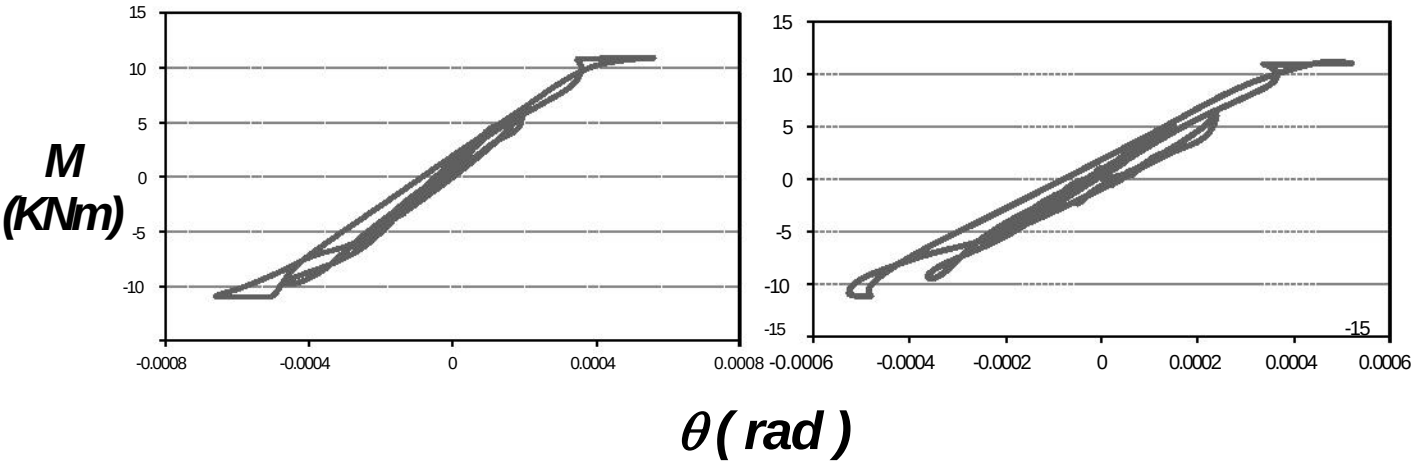

Figure 5.5.1 Moment-Angle of the conventional foundations 3,4 for the Aegio record in the longitudinal direction

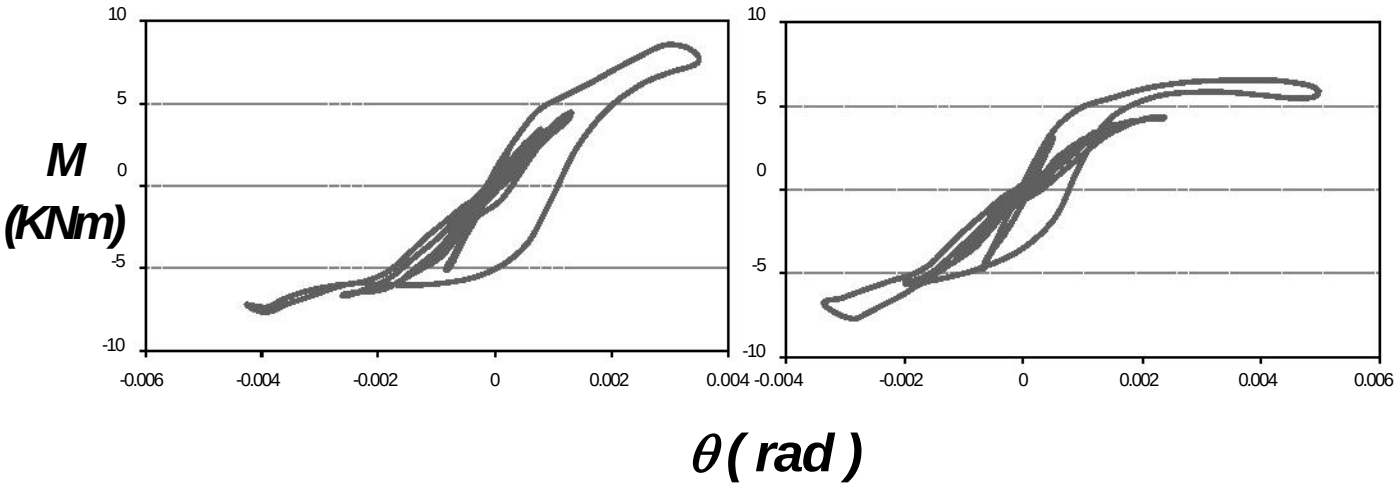

Figure 5.5.2 Moment-Angle of the under-designed foundations 3,4 for the Aegio record in the longitudinal direction

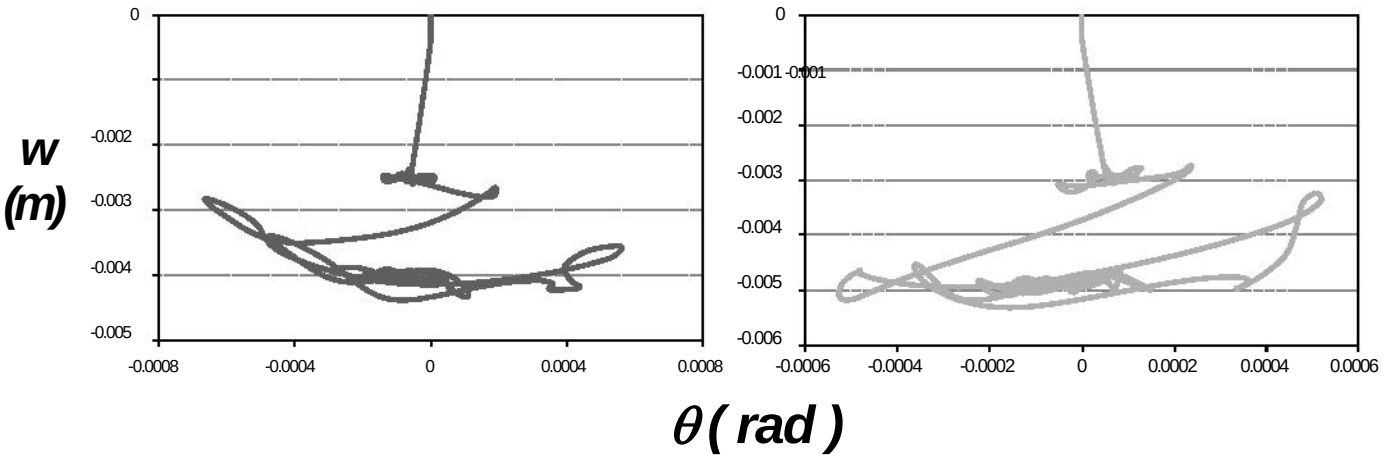

Figure 5.6.1 Settlement-Rotation of the conventional foundations 3,4 for the Aegio record in the longitudinal direction

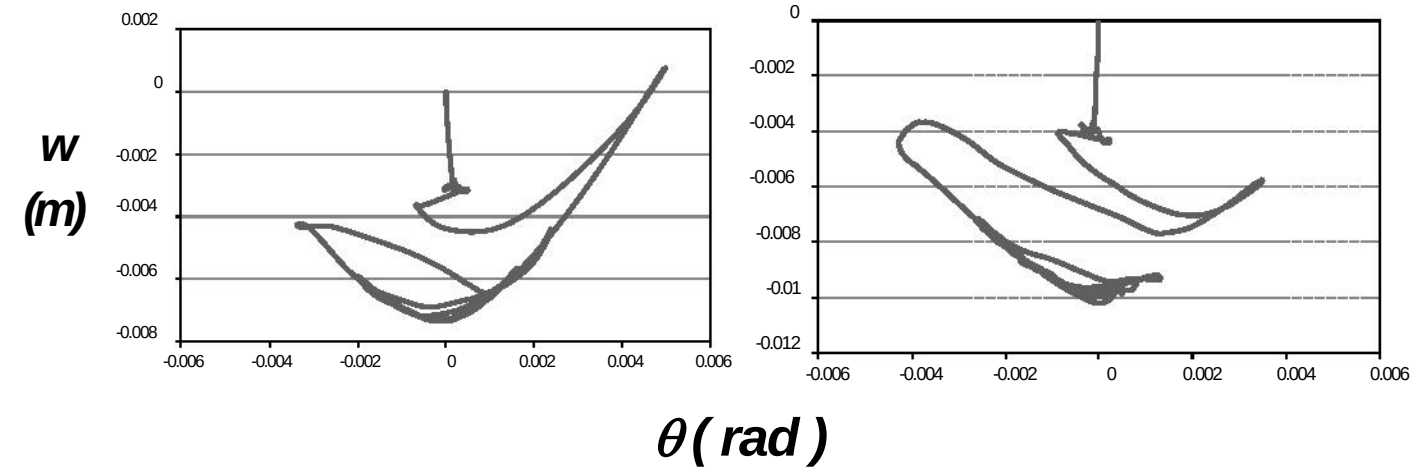

Figure 5.6.2 Settlement-Rotation of under-designed foundations 3,4 for the Aegio record in the longitudinal direction

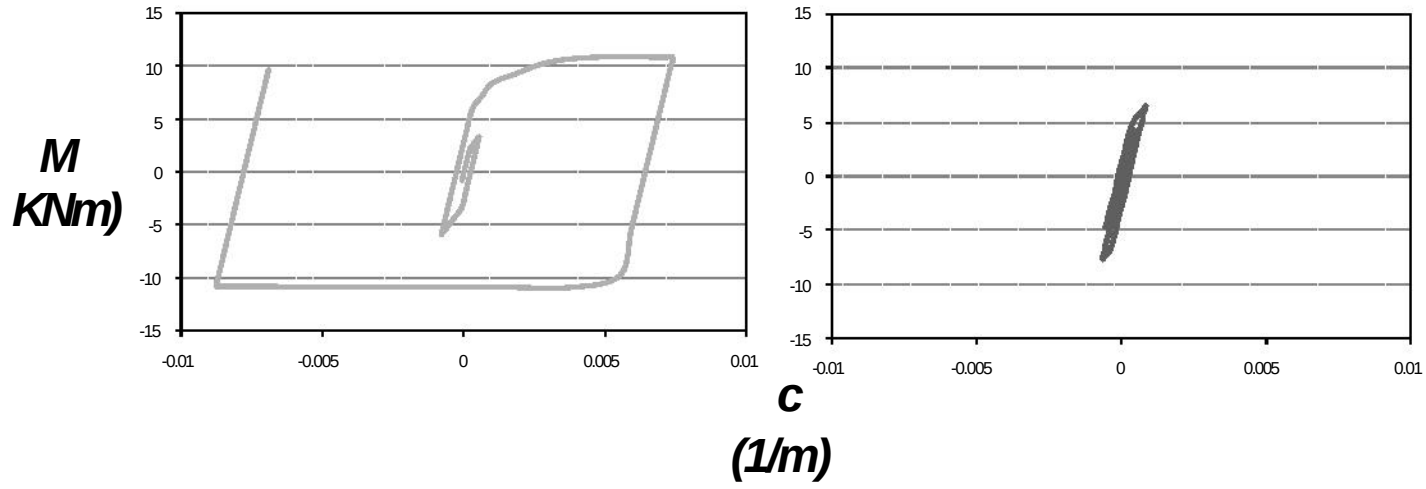

Figure 5.7.1 Moment-Curvature of the pier 3 for the Aegio record in the longitudinal direction

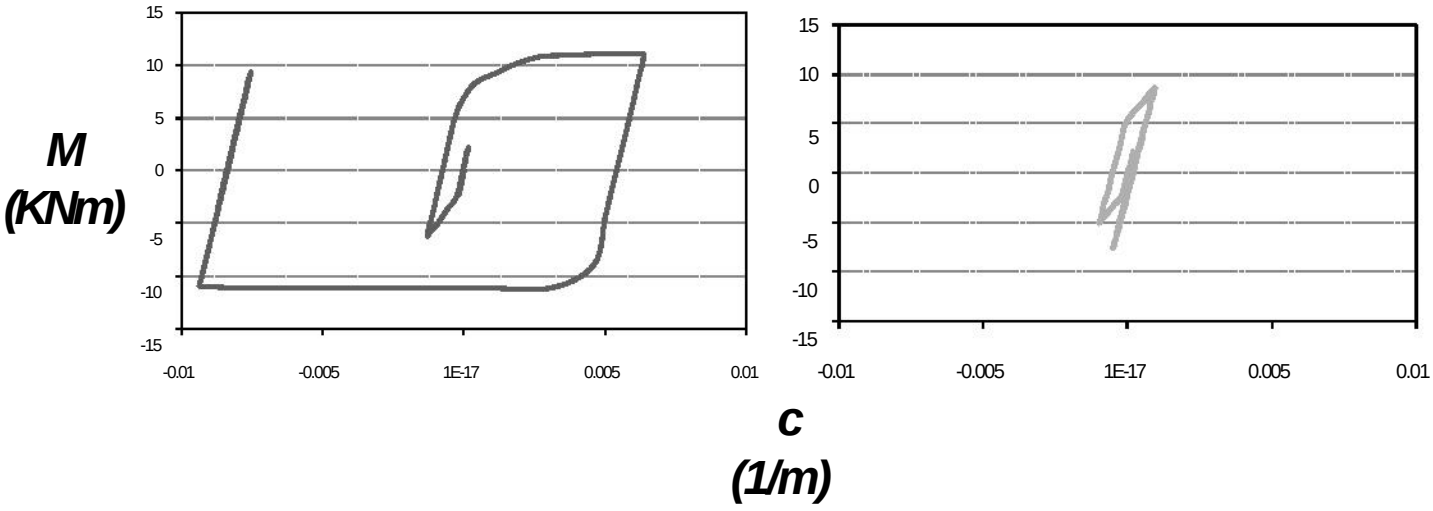

Figure 5.7.2 Moment-Curvature of the pier 4 for the Aegio record in the longitudinal direction

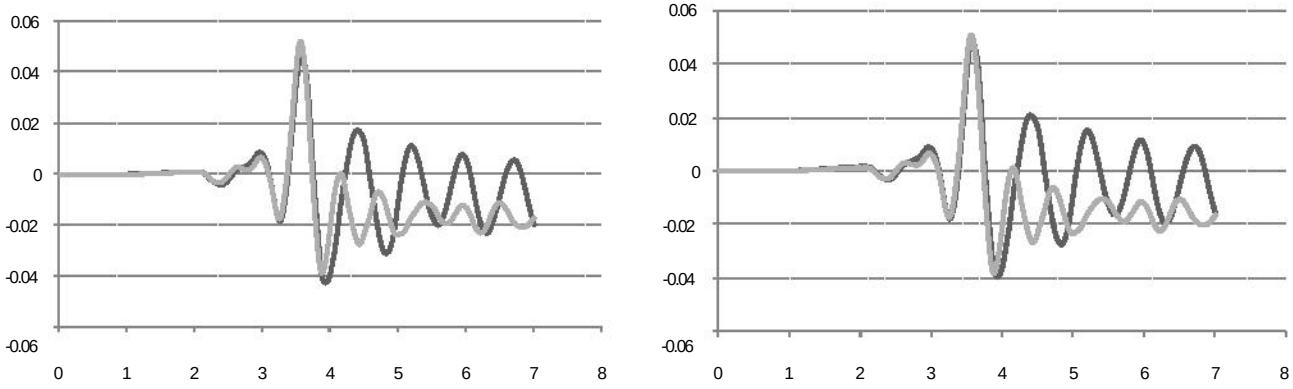

Figure 5.8 Comparison of the horizontal drift of the piers 3,4 for the Aegio record in the longitudinal direction

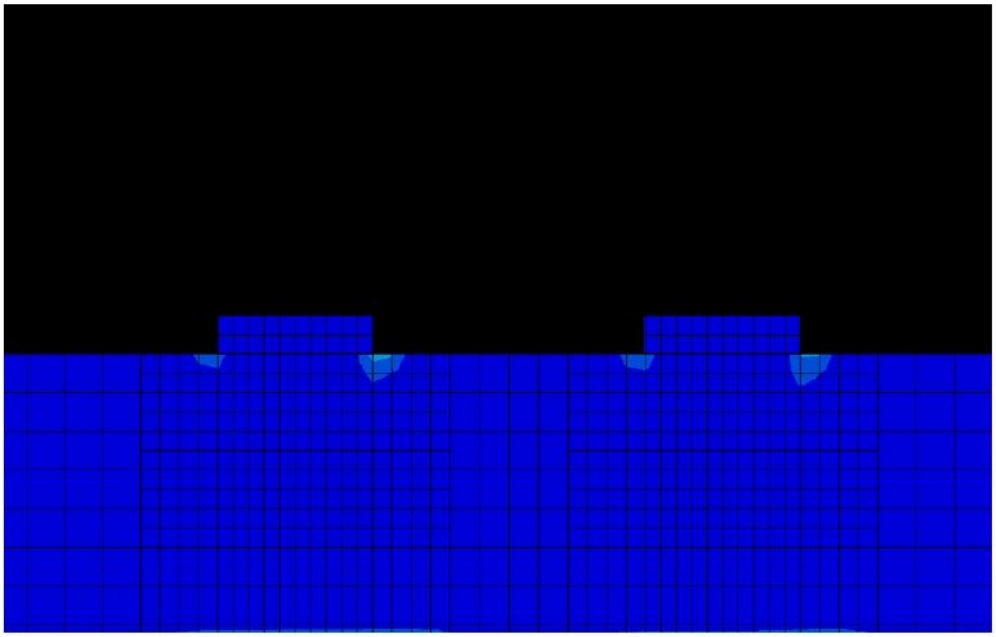

Figure 5.9.1 Deformed mesh with superimposed plastic strain for the conventional foundation for the Rinaldi_228 in the Longitudinal direction

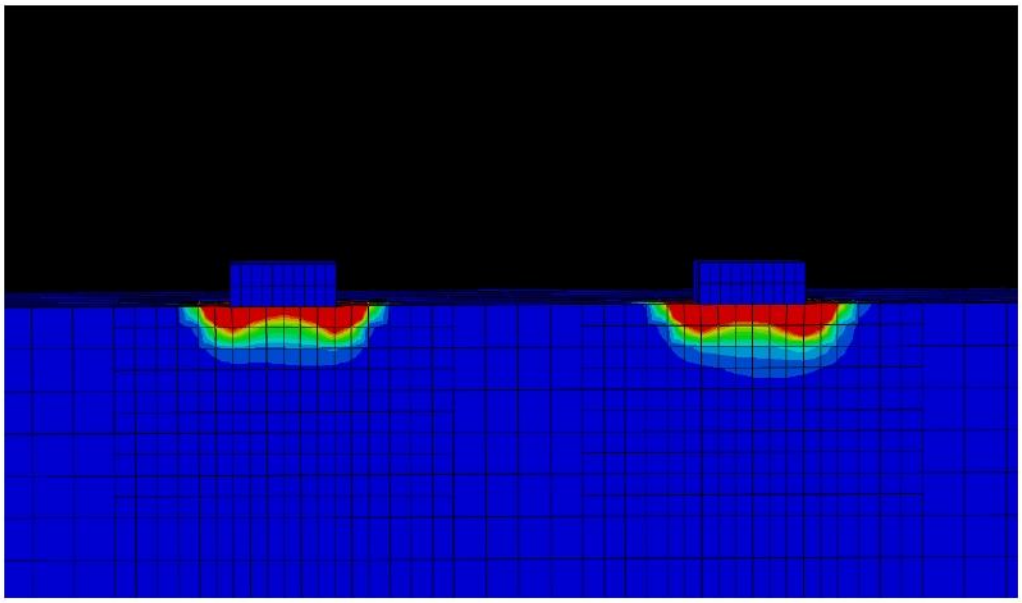

Figure 5.9.2 Deformed mesh with superimposed plastic strain for the under-designed foundation for the Rinaldi_228 in the Longitudinal direction

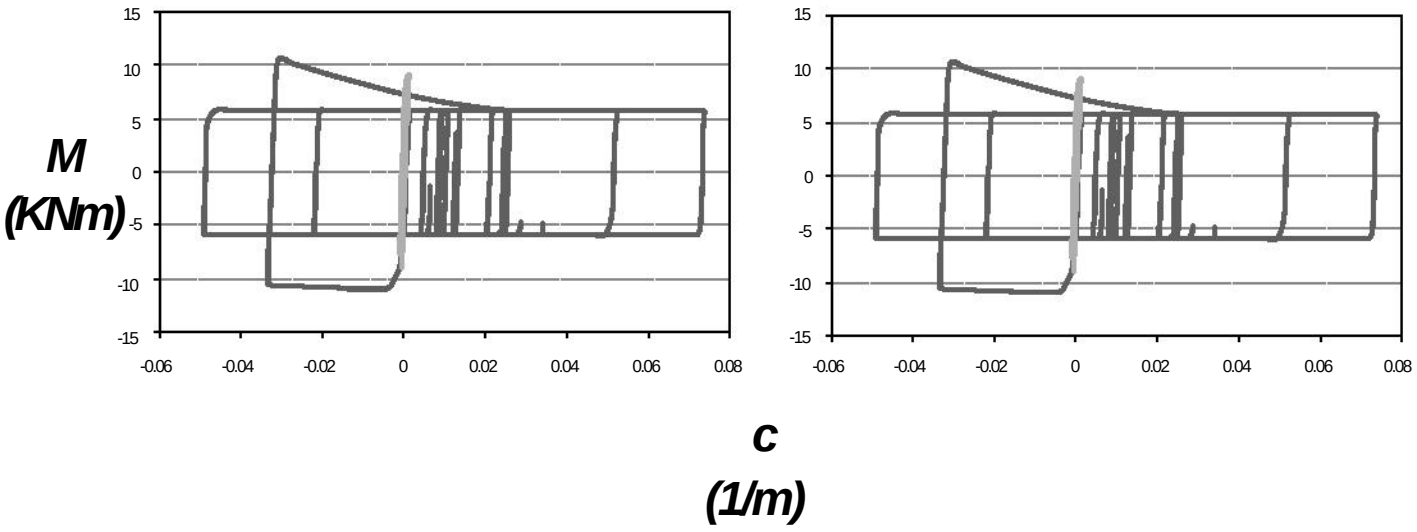

Figure 5.10 Comparison in terms of Moment-Curvature of the piers 3,4 for the Rinaldi_228 record in the Longitudinal direction

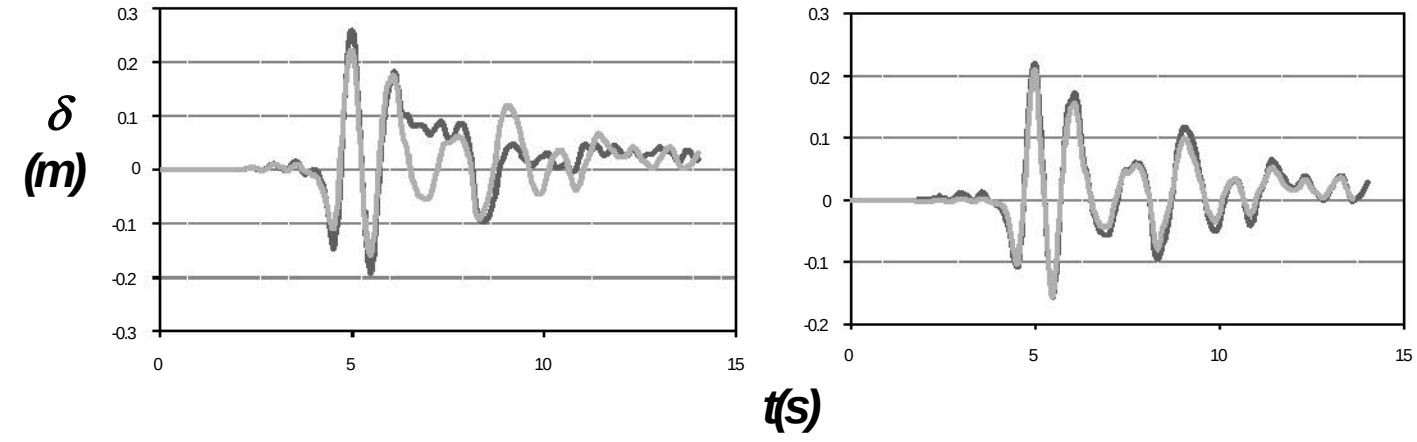

Figure 5.11 Comparison in terms of horizontal drift of the piers 3,4 for the Rinaldi_228 record in the Longitudinal direction

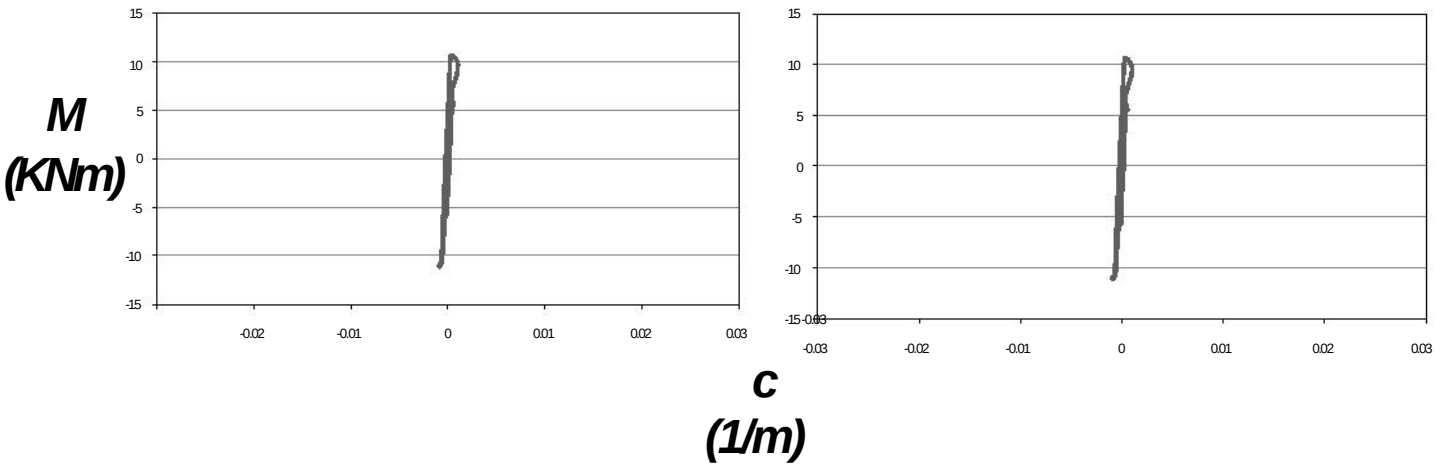

Figure 5.12.1 Moment-Rotation of the conventional foundations 3,4 for the Rinaldi_228 record in the Longitudinal direction

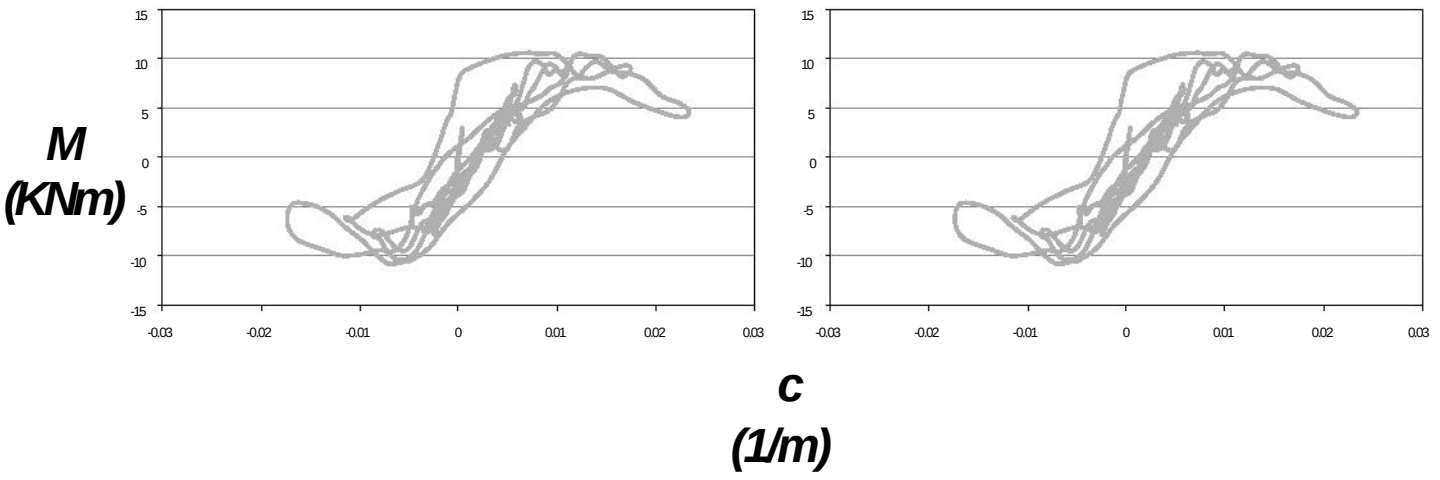

Figure 5.12.2 Moment-Rotation of the under-designed foundations 3,4 for the Rinaldi_228 record in the Longitudinal direction

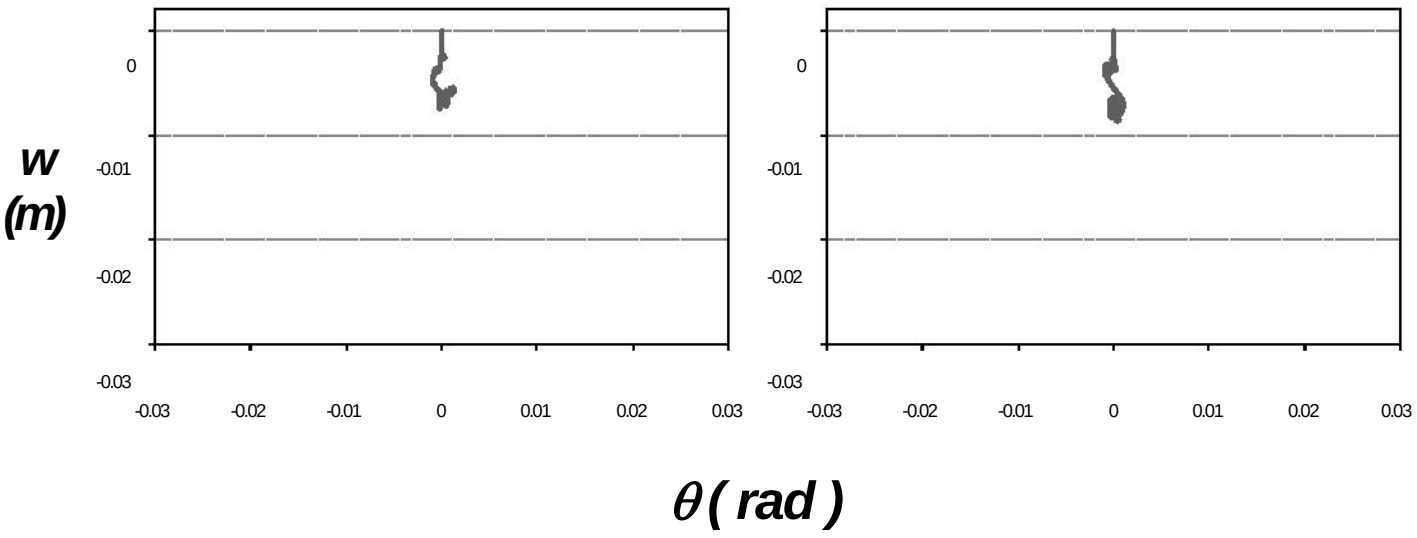

Figure 5.13.1 Settlement-Rotation of the conventional foundations 3,4 for the Rinaldi_228record in the longitudinal direction

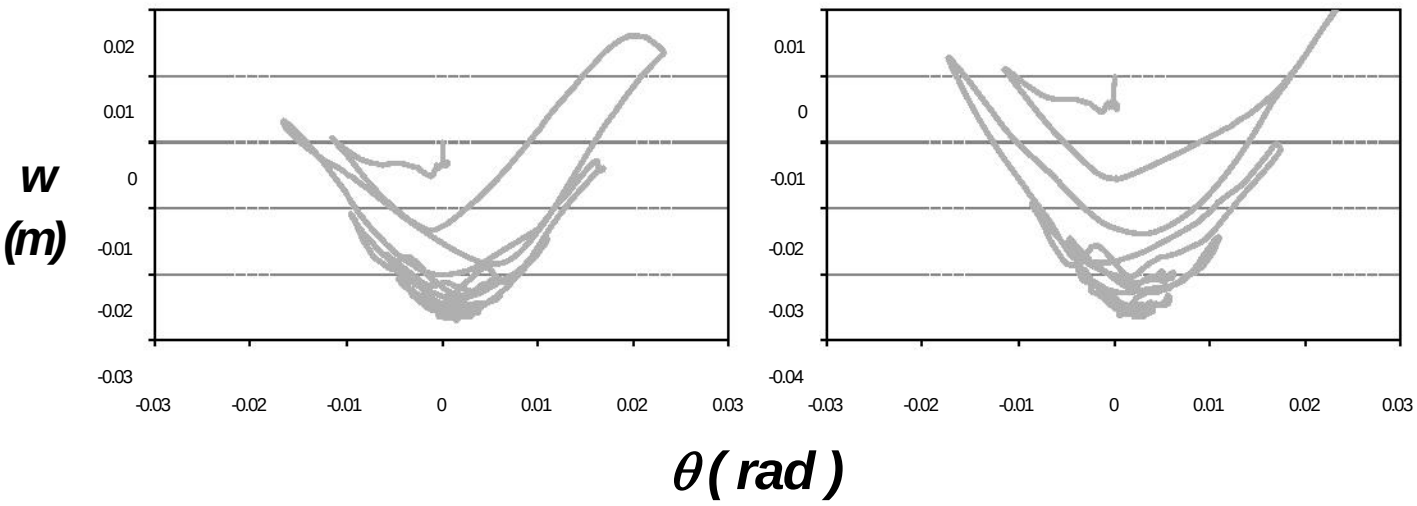

Figure 5.13.2 Settlement-Rotation of under-designed foundations 3,4 for the Rinaldi_228record in the longitudinal direction

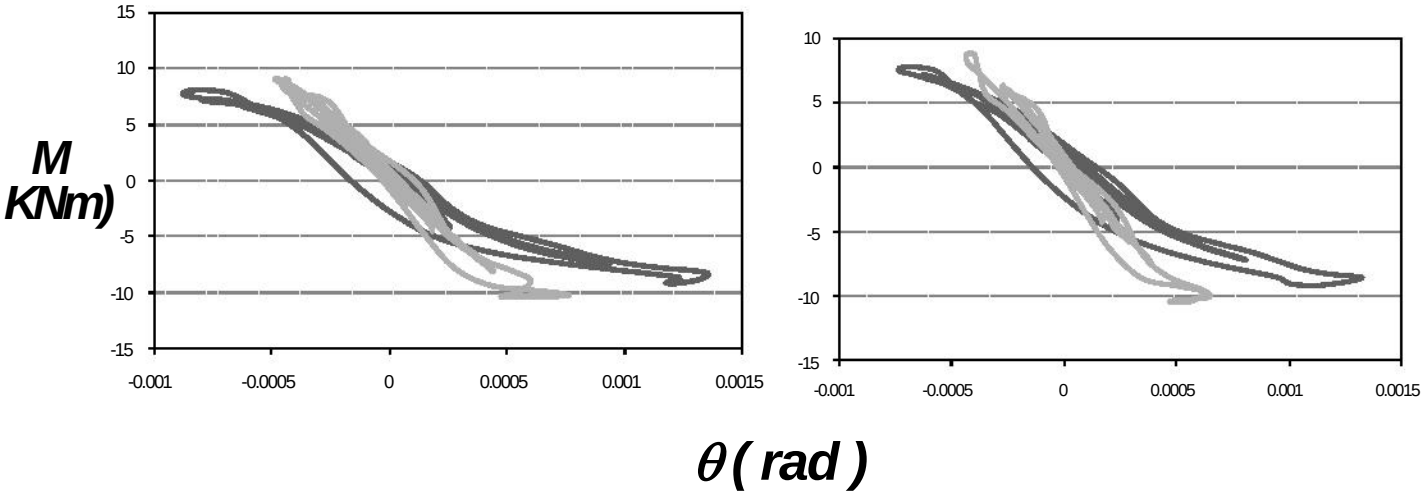

Figure 5.14.1 Comparison in terms of Moment-Rotation of foundations 1,2 for the Aegio record in the Transverse direction

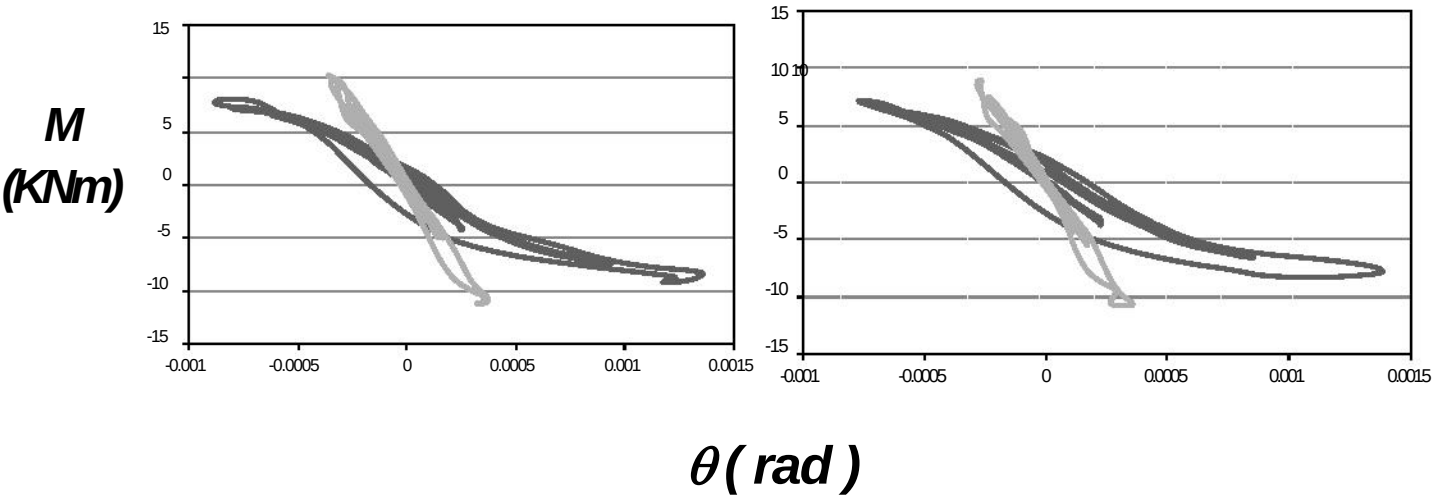

Figure 5.14.2 Comparison in terms of Moment-Rotation of foundations 3,4 for the Aegio record in the Transverse direction

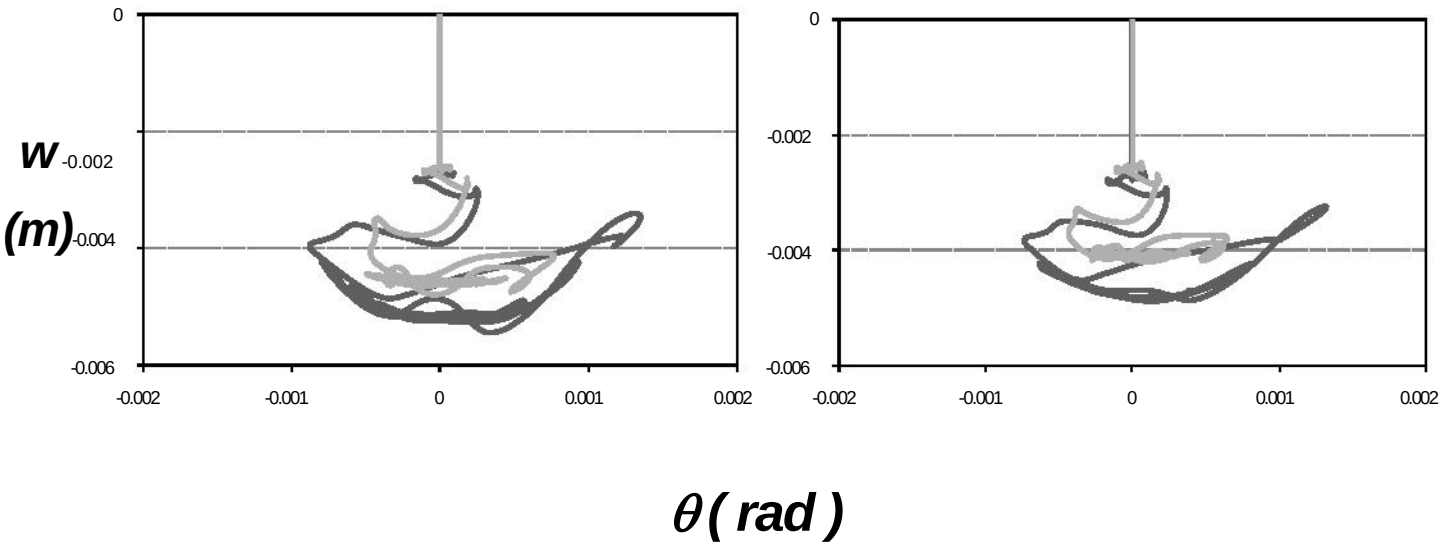

Figure 5.15.1 Comparison in terms of Settlement-Rotation of foundations 1,2 for the Aegio record in the Transverse direction

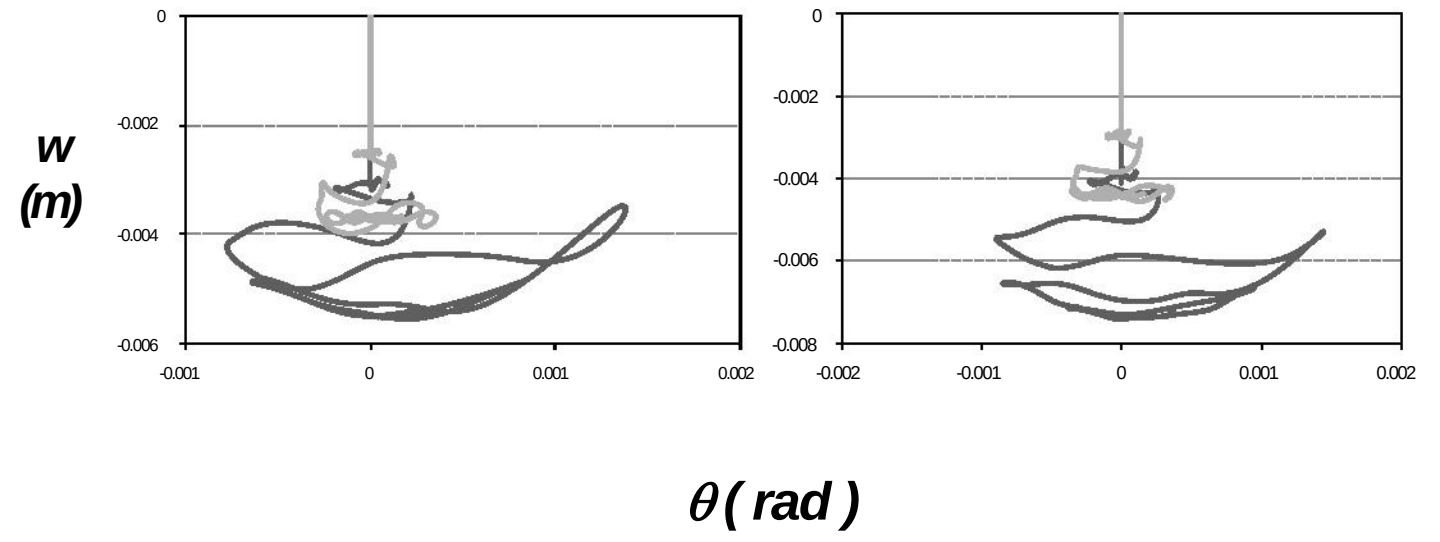

Figure 5.15.2 Comparison in terms of Settlement-Rotation of foundations 3,4 for the Aegio record in the Transverse direction

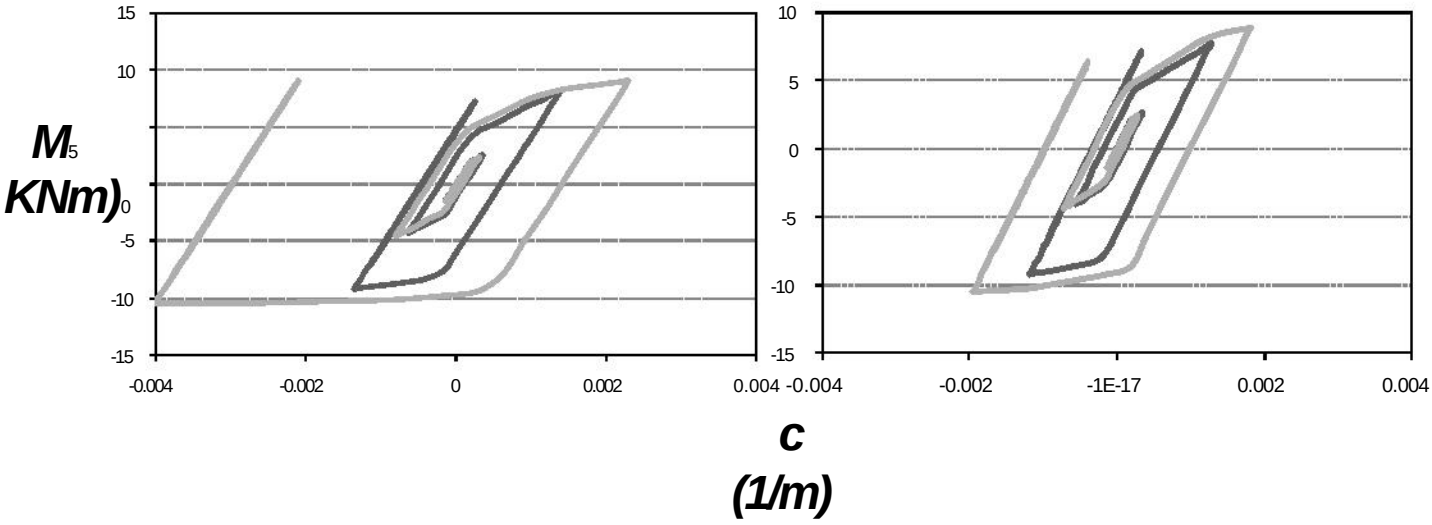

M ***KNm)***

c

(1/m)

Figure 5.16.1 Comparison in terms of Moment-Curvature of the piers 1,2 for the Aegio record in the Transverse direction

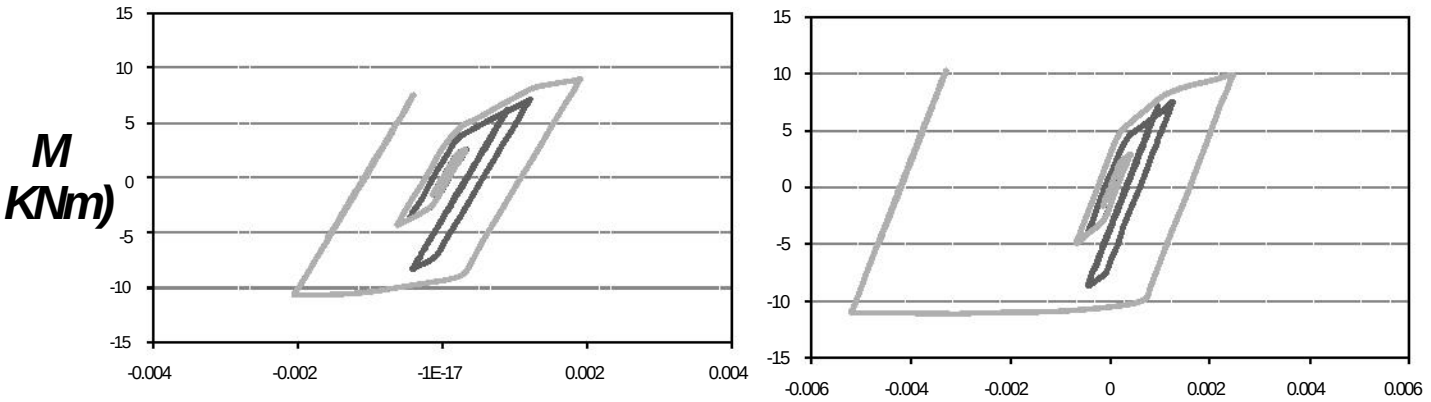

M ***KNm)***

c

(1/m)

Figure 5.16.2 Comparison in terms of Moment-Curvature of the piers 3,4 for the Aegio record in the Transverse direction

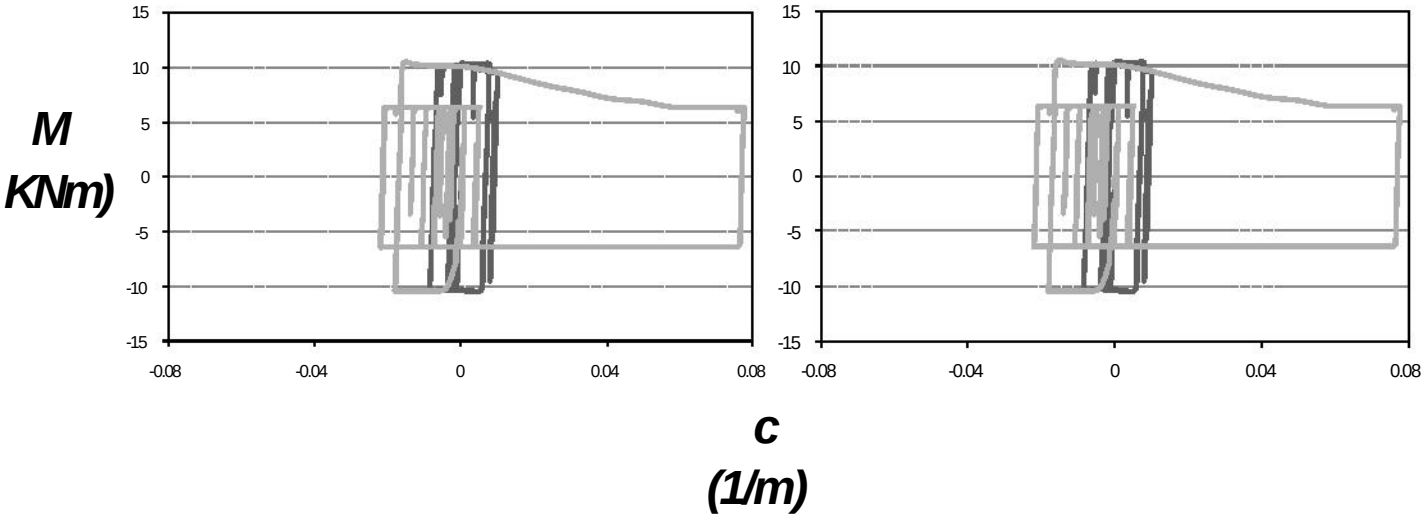

Figure 5.18.1 Comparison in terms of Moment-Curvature of the piers 1,2 for the Rinaldi_228 record in the Transverse direction

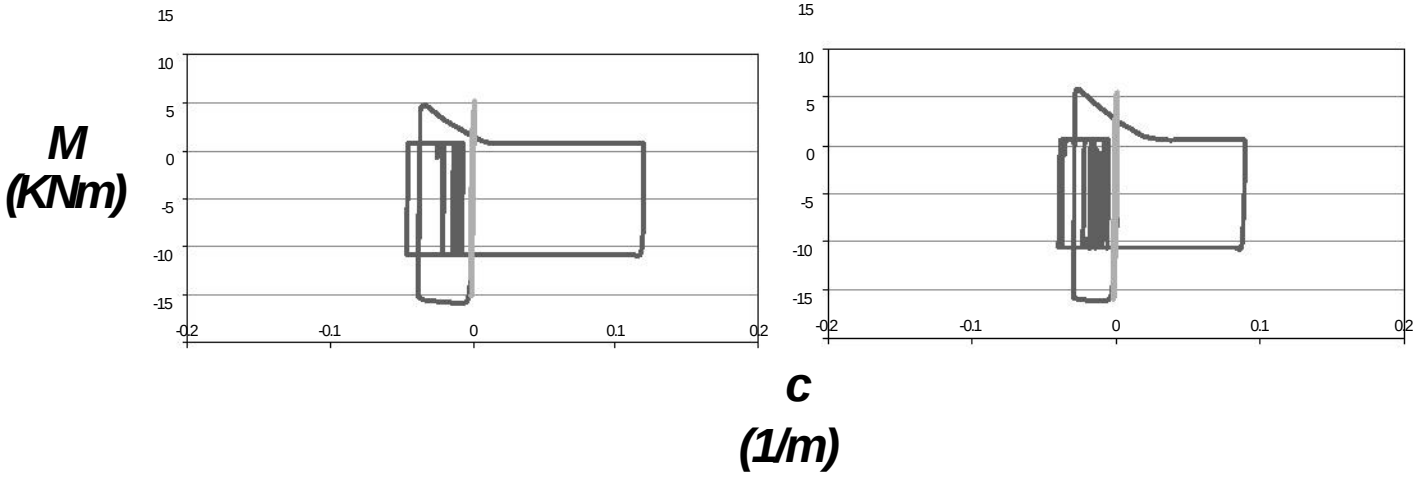

Figure 5.18.2 Comparison in terms of Moment-Curvature of the piers 1,2 for the Rinaldi_228 record in Transverse direction

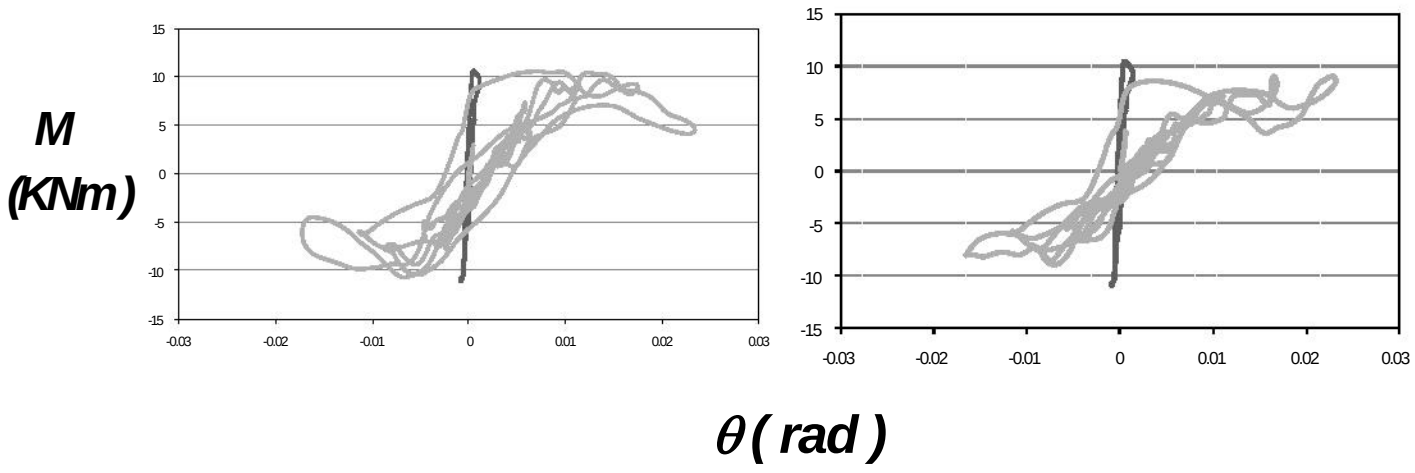

Figure 5.19 Comparison in terms of Moment-Rotation of foundations 1,2 for the Rinaldi_228 record in the Transverse direction

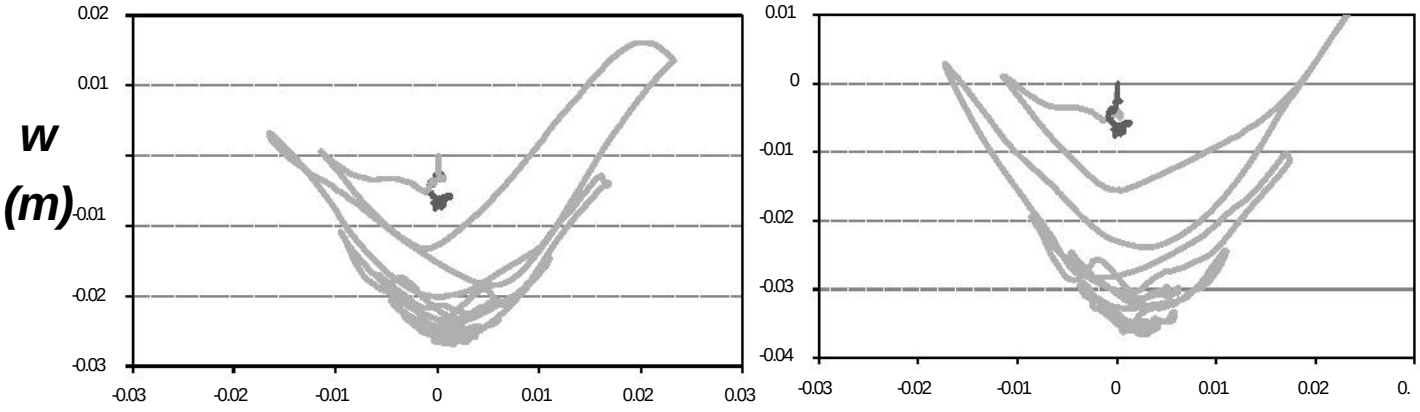

References

ABAQUS 6.11. (2011). Standard user's manual. Dassault Systèmes Simulia Corp., Providence, RI, USA.

Anastasopoulos I., Gelagoti F., Kourkoulis R., Gazetas G. (2011). “Simplified Constitutive model for Simulation of Cyclic Response of Shallow Foundations: Validation against Laboratory Tests”, *Journal of Geotechnical and Geoenvironmental Engineering*, ASCE, Vol. 137, No. 12, pp. 1154–1168.

Anastasopoulos I., Kokkali P., Tsatsis A. (2011), “Experimental Investigation of Vertical Load Capacity of Surface Footings”.

Anastasopoulos I., Kokkali P., Tsatsis A. (2011). “1-dof System Lying on Square Foundation: Monotonic and Cyclic Loading”.

Anastasopoulos I., Gazetas G., Loli M., Apostolou M., Gerolymos N. (2010). “Soil failure can be used for seismic protection of structures”. *Bulletin of Earthquake Engineering* 8, pp. 309-326.

Applied Technology Council (1985). “Earthquake Damage Evaluation Data for California”, *Rep. No. ATC-13, Applied Technology Council, Redwood City, CA.*

Applied Technology Council (1991). ”Seismic Vulnerability and Impact of Disruption of Lifelines in the Conterminous United States”, *Rep. No. ATC-25, Applied Technology Council, Redwood City, CA.*

Ayyub, B. M. and Lai, K.-L. (1989). "Structural reliability assessment using Latin Hypercube Sampling." *Proceedings of ICOSSAR '89, the 5th International Conference on Structural Safety and Reliability*, Part II , ASCE, New York NY USA , p 1177-1184.

Basoz N. , Kiremidjian, A. S. (1999). "Development of Empirical Fragility Curves for Bridges." *5th US Conference on Lifeline Earthquake Engineering* , ASCE, New York NY USA .

Basoz N., Kiremidjian, A. S. (1997). “Evaluation of Bridge Damage Data From the Loma Prieta and Northridge, CA Earthquakes.” *Rep. No. MCEER-98-0004*, John A. Blume Earthquake Engineering Center, Stanford, CA.

Basoz N., Kiremidjian, A. S. (1996). “Risk Assessment for Highway Transportation Systems.” *Rep. No. NCEER-118*, JohnA. Blume Earthquake Engineering Center, Stanford, CA.

Broglio, S., Crowley, H., Pinho, R. (2010). “Simplified capacity curves for RC bridges” *Proceedings of the 14th European Conference on Earthquake Engineering*, paper no. 1336, Ohrid, Macedonia.

Chai, Y. H., Priestley, M. J. N., and Seible, F. (1991). "Seismic Retrofit of Circular Bridge Columns for Enhanced Flexural Performance." *ACI Structural Journal (American Concrete Institute),* 88(5), 572-584.

Choi E, DesRoches R, Nielson B (2004). “Seismic fragility of typical bridges in moderate seismic zones”. Engineering Structures ; 26:187–199.

Chopra A. K. (1995): “*Dynamics of structures – Theory and applications to earthquake engineering”*, Prentice-Hall Inc.

Codermatz R., Nicolich R., Slejko D. (2003). “Seismic risk assessments and GIS technology: applications to infrastructures in the Friuli-Venezia Giulia region (NE Italy)”. *Earthquake Engineering and Structural Dynamics,* Vol.32, pp. 1677-1690.

EAK (2000) “Greek Seismic Code”, Organization of Seismic Planning and Protection, Athens (in Greek).

ΕΚΩΣ(2000) “Greek code for reinforced concrete”, Organization of Seismic Planning and Protection, Athens (in Greek).

EN1998-1-1, “Eurocode 8: *Design of structures for earthquake resistance – Part 1 -1”: General rules, seismic actions and rules for buildings, CEN, 2003.*

Erdik M., Fahjan Y., Ozel O., Alcik H., Mert A., Gul M.,(2003). “Istanbul Earthquake Rapid Response and the Early Warning System”, *Bulletin of Earthquake Engineering* **1,** pp. 157-163.

Erdik M., Sesetyan K., Demircioglu M.B., Hancılar U., Zulfikar C. (2010) “Rapid earthquake loss assessment after damaging earthquakes”. *Soil Dynamics and Earthquake Engineering*, Vol. 31, pp. 247-266.

Esposito, S. and Iervolino, I. (2010) “PGA and PGV Spatial Correlation models based on European multi-event datasets”, *Bulletin of the Seismological Society of America*. 101 (5): 2532-2541.

FEMA. (1997). “HAZUS 97 Technical Manual II.” Washington DC, FEMA.

Garini, E. (2011). “Sliding Systems under Near–Fault Ground Shaking: Development and Demonstration of Inelastic Analogues”, *Doctoral Thesis NTUA*.

Gazetas G., Anastasopoulos I, Adamidis O., Kontoroupi T. ,(2013). “Nonlinear rocking stiffness of foundations”*, Soil Dynamics and Earthquake Engineering Volume 47, April 2013, Pages 83–91*

Gazetas G, Anastasopoulos I, Gerolymos N, Mylonakis G, Syngros C. (2005). ”The collapse of the Hanshin expressway (Fukae) bridge, Kobe 1995: soil-foundation-structure interaction, reconstruction, seismic isolation”, *Entwicklungen in der Bodenmechanik, Bodendynamik und Geotechnik, Festschrift zum 60. Geburstag von Univ.-Professor Dr.-Ing.habil. Stavros A. Savidis (Honorary Volume for the 60th Birthday of Professor Savidis)*, Frabk Rackwitz, Springer, pp 93–120. 219

Gazetas, G. (2005):“Soil Dynamics” Geotechnical Division, National Technical University of Athens, 2005 (in Greek).

Gazetas G, ApostolouM, Anastasopoulos I. (2003). “Seismic uplifting of foundations on soft soil, with examples from Adapazari (Izmit 1999, Earthquake)”. *In: BGA int. conf. on found. innov., observations, design & practice*, Univ. of Dundee, Scotland, September 25, pp 37–50.

Gazetas, G. [1991]. “Formulas and charts for impedances of surface and embedded foundations”, *Journal of Geotechnical Engineering*, ASCE, 117 (9), 1129–1141.

Gazetas G. (1987). “Simple physical methods for foundation impedances.” *Dynamics of Foundations and Buried Structures, Benerjee PK and Butterfield R., editors, ElsevierApplied Science*, Chapter 2, 44-90.

Gazetas, G. (1983). “Analysis of machine foundation vibrations: state of the art,” Soil Dynamics and Earthquake Engineering, 2(1), 2-42.

Gourvenec S. (2007). “Shape effects on the capacity of rectangular footings under general loading”, *Geotechnique 57, No. 8, pp. 637–646.*

Hwang H, Liu JB, Chiu Y-H.(2000) “Seismic fragility analysis of highway bridges”. *MAEC RR-4*, Center for Earthquake Research Information.

Hwang, H., Huo, J. R. (1998). "Probabilistic Seismic Damage Assessment of Highway Bridges." *6th US National Conference on Earthquake Engineering*, EERI, Oakland, CA.

Hwang, H., Jaw, J. W. (1990). "Probabilistic Damage Analysis of Structures." *Journal of Structural Engineering*, 116(7), 1992-2007.

Jacob, K. H. (1992). "Seismic Hazards in the Eastern U.S. and the Impact on Transportation Lifelines." *Lifeline Earthquake Engineering in the Central and Eastern U.S*., Monograph No. 5, ASCE, New York NY USA .

Jernigan JB, Hwang H. (2002) “Development of bridge fragility curves”. *7th US National Conference on Earthquake Engineering*, EERI: Boston, MA, 2002.

Karim, K.R., Yamazaki, F. (2003). “A simplified method of constructing fragility curves for highway bridges”. *Earthquake Engineering and Structural dynamics* **32**, 1603-1626.

Karim, K.R., Yamazaki, F. (2001). “Effect of earthquake ground motions on fragility curves of highway bridge piers based on numerical simulation”. *Earthquake Engineering and Structural dynamics* **30**, 1839-1856. 220

Kiureghian, A. D. (2002). "Bayesian Methods for Seismic Fragility Assessment of Lifeline Components." Acceptable Risk Processes: Lifelines and Natural Hazards, Monograph No. 21, A. D. Kiureghian, ed., Technical Council on Lifeline Earthquake Engineering, ASCE, Reston VA USA.

Kottegoda N. T. , Rosso, R. (1997). "Statistics, Probability, and Reliability for Civil and Environmental Engineers." The McGraw-Hill Companies, Inc.
Kourkoulis, R., Anastasopoulos, I., Gelagoti, F., Kokkali, P. (2012). "Dimensional Analysis of SDOF Systems Rocking on Inelastic Soil", *Journal of Earthquake Engineering* (in press).

Koutsourelakis S., Prevost J., Deodatis G. (2002). "Risk assessment of an interacting structure–soil system due to liquefaction Earthquake" *Earthquake Engineering and Structural Dynamics* (2002)31 pp.: 851–879.

Kowalsky, M. J. (2000). "Deformation Limit States for Circular Reinforced Concrete Bridge Columns" *Journal of Structural Engineering*, 126(8), 869-878.

Kwon O, Elnashai A.(2010) , "Fragility analysis of a highway over-crossing bridge with consideration of soil–structure interactions", *Structure and Infrastructure Engineering Volume 6*, Issue 1-2, 2010 pages 159-178.

Mackie, K. and Stojadinovic, B. (2003). "Seismic Demands for Performance-Based Design of Bridges." Rep. No. PEER 312.

Mackie, K. and Stojadinovic, B. (2001). "Probabilistic Seismic Demand Model for California Bridges." *Journal of Bridge Engineering*, 6(6), 468-480.
Mander, J. B., Kim, D. K., Chen, S. S., Premus, G. J. (1996). "Response of Steel Bridge Bearings to the Reversed Cyclic Loading." *Rep. No. NCEER 96-0014*, NCEER, Buffalo, NY.

Mander, J. B., Basoz, N. (1999). "Seismic Fragility Curve Theory for Highway Bridges." *5th US Conference on Lifeline Earthquake Engineering* , ASCE, New York NY USA .

Meyerhof, G. G. (1951). "The ultimate bearing capacity of foundations", *Geotechnique*, 2 (4), 301-332.
Moschonas, I.F., Kappos, A.J., Panetsos, P., Papadopoulos, V., Makarios, T. and Thanopoulos, P. (2009). "Seismic fragility curves for greek bridges: methodology and case studies", *Bulletin of Earthquake Engineering* **7**, pp. 439-468.

Nielson BG. (2005) "Analytical fragility curves for highway bridges in moderate seismic zones". Ph.D. Thesis, Georgia Institute of Technology, 2005.

Pitilakis, K., Kakderi, K. (2011) "Seismic risk assessment and management of lifelines", utilities and infrastructures. 221

Priestley, M.J.N., Seible, F., Calvi, G.M. (1996) “Seismic Design and Retrofit of Bridges,” John Wiley and Sons, New York.

Selva, J., Kakderi, K., Alexoudi, M., Pitilakis, K. (2011). “Seismic Performance of a System of Interdependent Lifeline and Infrastructure Components*”, 8th International Conference on Urban Earthquake Engineering*, March 7-8, 2011, Tokyo Institute of Technology, Tokyo. Japan.

Shinozuka M, Feng MQ, Lee J, Naganuma T.(2000). “ Statistical analysis of fragility curves”. *Journal of Engineering Mechanics*; 126:1224–1231.

Shinozuka M, Feng MQ, Kim H-K, Kim S-H.(2000). Nonlinear static procedure for fragility curve development. *Journal of Engineering Mechanics* 2000; 126:1287–1296.
Shinozuka, M., Feng, M. Q., Dong, X., Uzawa, T., and Ueda, T. (2000). "Damage Assessment of a Highway Network Under Scenario Earthquakes for Emergency Response Decision Support." *Proceedings of SPIE* - The International Society for Optical Engineering, Society of Photo-Optical Instrumentation Engineers , Bellingham WA USA , p264-275.

Vamvatsikos D. , Cornell CA. (2002) “Incremental dynamic analysis Earthquake” *Earthquake Engineering and Structural Dynamics* 31 pp. :491–514.

Vamvatsikos D, Cornell CA.(2001) “Tracing and post-processing of IDA curves: Theory and software implementation” . Report No. RMS-44, RMS Program, Stanford University, Stanford.
Wen, Y. K., Ellingwood, B. R., Veneziano, D., and Bracci, J. (2003). *Rep. No. MAE-FD-2*, Mid-America Earthquake Center, Urbana, IL.

Wen, Y. K. and Wu, C. L. (2001). "Uniform Hazard Ground Motions for Mid-America Cities." *Earthquake Spectra*, 17(2), 359-384.

Yamazaki F, Hamada T, Motoyama H, Yamauchi H.(1999). “Earthquake damage assessment of expressway bridges in Japan”. *Technical Council on Lifeline Earthquake Engineering Monograph* 1999; 361–370.